

6. SITE 960¹

Shipboard Scientific Party²

HOLE 960A

Date occupied: 24 January 1995
Date departed: 31 January 1995
Time on hole: 7 days, 11 hr, 30 min
Position: 3°34.979'N, 2°44.009'W
Bottom felt (drill pipe measurement from rig floor, m): 2059.7
Distance between rig floor and sea level (m): 11.44
Water depth (drill pipe measurement from sea level, m): 2048.3
Total depth (from rig floor, m): 2510.9
Penetration (m): 451.2
Number of cores (including cores having no recovery): 61
Total length of cored section (m): 451.2
Total core recovered (m): 145.01
Core recovery (%): 32.1
Oldest sediment cored:
Depth (mbsf): 451.2
Lithology: claystone/sandstone
Age: Early Cretaceous(?)
Measured velocity (km/s): 3.466 at 159-960A-61R-1, 112 cm

HOLE 960B

Date occupied: 31 January 1995
Date departed: 31 January 1995
Time on hole: 5 hr, 45 min
Position: 3°35.024'N, 2°43.986'W
Bottom felt (drill pipe measurement from rig floor, m): 2045.4
Distance between rig floor and sea level (m): 11.44
Water depth (drill pipe measurement from sea level, m): 2034.0
Total depth (from rig floor, m): 2052.5
Penetration (m): 7.10
Number of cores (including cores having no recovery): 1
Total length of cored section (m): 7.10
Total core recovered (m): 7.15
Core recovery (%): 101.0

Oldest sediment cored:

Depth (mbsf): 7.15
Lithology: nannofossil foraminifer ooze
Age: Pleistocene
Measured velocity (km/s): not measured

Comments: Mud-line core only. Entire core was archived.

HOLE 960C

Date occupied: 31 January 1995
Date departed: 4 February 1995
Time on hole: 3 days, 3 hr, 45 min
Position: 3°35.025'N, 2°43.990'W
Bottom felt (drill pipe measurement from rig floor, m): 2046.3
Distance between rig floor and sea level (m): 11.44
Water depth (drill pipe measurement from sea level, m): 2034.9
Total depth (from rig floor, m): 2399.1
Penetration (m): 352.8
Number of cores (including cores having no recovery): 26
Total length of cored section (m): 230.3
Total core recovered (m): 160.67
Core recovery (%): 69.8
Oldest sediment cored:
Depth (mbsf): 377.7
Lithology: skeletal grainstone/packstone
Age: Late Cretaceous
Measured velocity (km/s): 5.323 at 159-960C-26X-1, 47 cm
Comments: Drilled 210.7–333.2 and 352.8–377.7 mbsf.

Principal results: *JOIDES Resolution* arrived at Site 960 and dropped a beacon using GPS navigation at the location of proposed site IG1-bis. An RCB BHA was made up and Hole 960A was spudded at 0630 hr on 24 January. Recovery in unconsolidated sediments was <30%. Below 330 mbsf recovery improved markedly within seismic Units A and B. Low rates of penetration prompted the dropping of a free-fall funnel and the bit was changed from a CC-4 to a CC-3. The hole was subsequently deepened to 451.2 mbsf after which a wiper trip was made and the hole was flushed with a sepiolite mud pill prior to logging. Caliper readings from the Quad combination tool string indicated that most of the hole was wider than 16 in., thus precluding use of the FMS tool. Hole 960B was spudded as an APC hole, and the top 7.13 m was taken as a mud-line core. Hole 960C was spudded as an APC/XCB hole and cored to 210.7 mbsf, then drilled ahead to 377.7 mbsf. Two cores were taken below 333.2 mbsf. A wiper trip was made and sepiolite circulated before logging with the Quad combination and FMS tool strings. The hole was finally displaced with heavy mud. The bit reached the rig floor at 0230 hr on 4 February.

Five lithologic units were identified from Holes 960A and 960C (Fig. 1). Lithologic Unit I comprises 111.2 m of Pleistocene to lower Miocene

¹Masle, J., Lohmann, G.P., Clift, P.D., et al., 1996. *Proc. ODP, Init. Repts.*, 159: College Station, TX (Ocean Drilling Program).

²Shipboard Scientific Party is given in the list preceding the Table of Contents.

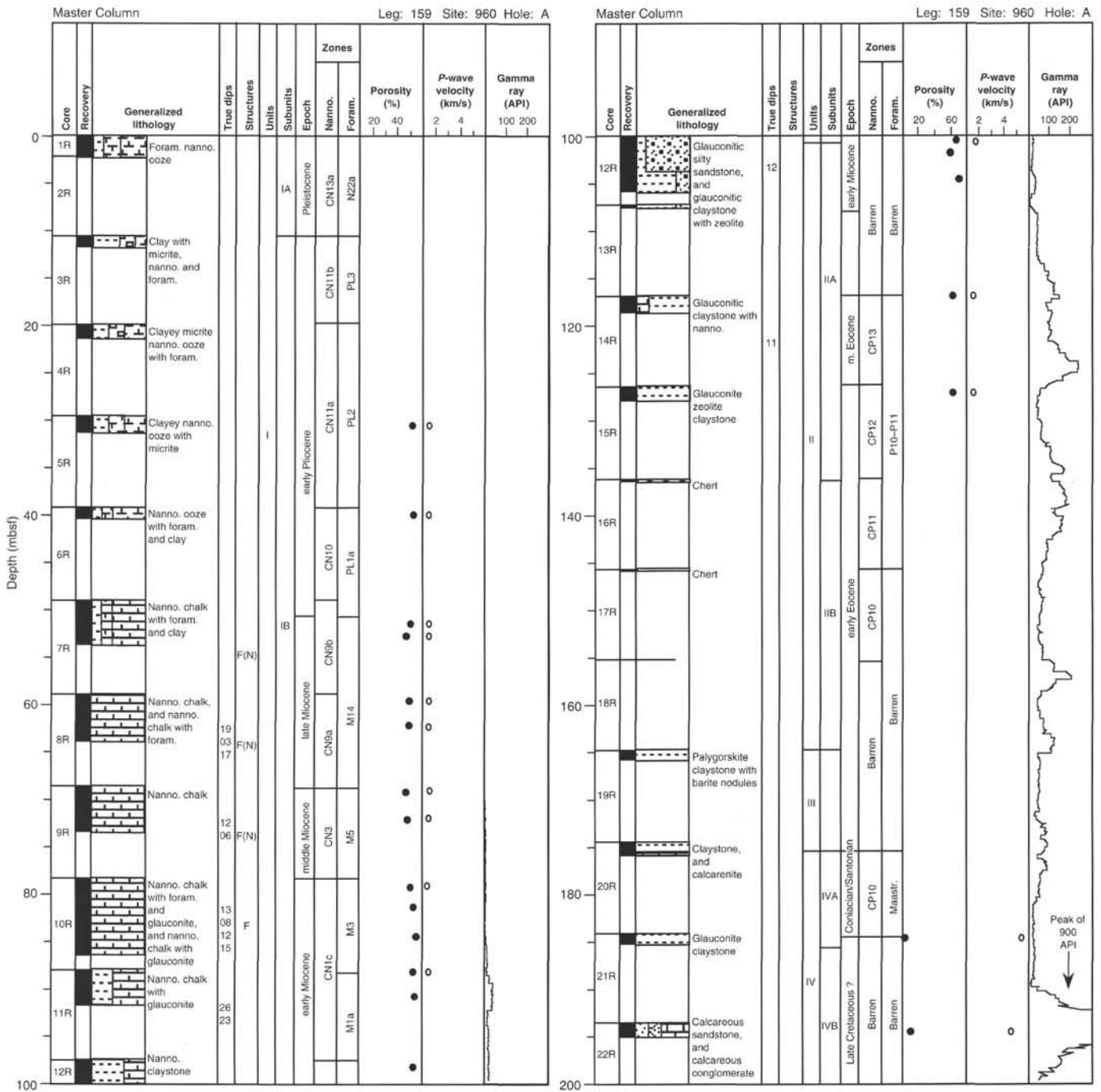


Figure 1. Site 960 master column.

nannofossil/foraminifer ooze (Subunit IA) and nannofossil/foraminifer chalk (Subunit IB). The first appearance (at 100.1 mbsf in Hole 960A and 111.2 mbsf in Hole 960C) of siliceous microfauna and flora marks the upper boundary of lithologic Unit II, characterized by radiolarian nannofossil chalk, claystone, and porcellanite of early Miocene to middle Eocene age, and chert of early to middle Eocene age. The lithologic Unit II/III boundary (164.8 mbsf in Hole 960A, and 179.0 mbsf in Hole 960C) is marked by the last occurrence of chert and the presence of a palygorskite-rich claystone interval containing barite concretions and nodules. This 20.5-m (Hole 960A) to 28.7-m (Hole 960C) unit is distinguished by its bluish-green color and abundant authigenic barite. Lithologic Subunit IVA is a condensed (<10 m) interval with fish debris, hardgrounds, glauconite claystones, and

micritic chalks (Coniacian-Santonian). Lithologic Subunit IVB (Turonian and older) is <144.9 m thick and is composed of quartz sand and skeletal packstones and grainstones. The top is identified as the first occurrence of bioclastic and intraclastic limestones, which contain variable amounts of quartz sand. The lower boundary is placed where bioclastic limestones of lithologic Subunit IVB overlie carbonate-cemented quartz sandstones of lithologic Unit V. The unit is 122.2 m thick. Carbonate-cemented sandstones and siltstones are found in lithologic Subunit VA, changing to silty sandstones, siltstones, and clayey siltstones, of possible lacustrine origin in lithologic Subunit VB. The age of this unit is unknown.

Bedding dips at 0–150 mbsf in Hole 960C display a wide range of values, largely due to slumping. The unconformity at the lithologic Unit IV/V

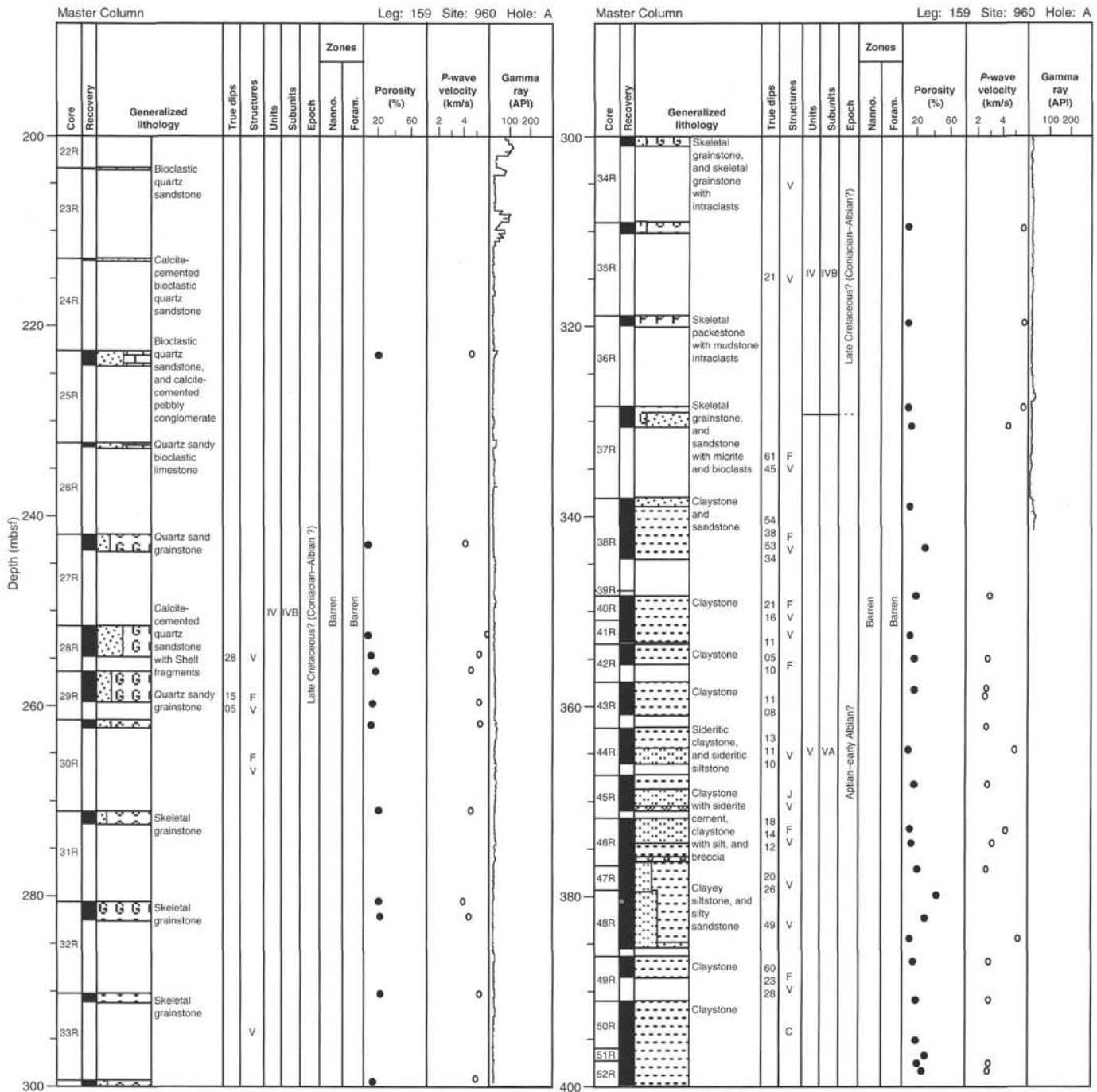


Figure 1 (continued).

boundary is characterized by fissuring, veining, and brecciation. The bedding dip data collected from Unit V show a wide spectrum (5°–60°), with the steeper dips measured directly below the unconformity, which is also the location of the majority of faulting and veining observed. Calcite and kaolinite veins are abundant, with quartz veins appearing at the bottom of Hole 960A (450 mbsf). Complex microfaulting, with associated asymmetric microfolds, displays both normal and reverse senses of motion, possible evidence for strike-slip flower structures. Oblique slickensides/mineral lineations in kaolinite-filled faults also clearly indicate strike-slip motion.

Pleistocene to early Eocene nannofossils were identified in the first 20 cores of Hole 960A. This sequence is interrupted by two barren intervals

and probably contains at least two major hiatuses. Middle Miocene Zone CN5 is missing. Nannofossils representing the time interval from Zone CP14 (middle Eocene) through to the top of Zone CP19 (late Oligocene) are missing. A barren interval is identified near the Neogene/Paleogene boundary. The lower/middle Eocene section contains a barren interval near its base. Nannofossil assemblages range from Turonian to Pleistocene in Core 159-960C-1H through Section 159-960C-26X-CC. Within this sequence at least three pronounced hiatuses could be detected. One of these hiatuses is between early Miocene and middle Eocene assemblages. The youngest hiatus is within Core 159-960C-10H, separating sediments of Zone CN7 (late Miocene) from those of Zone CN4 (early middle Mi-

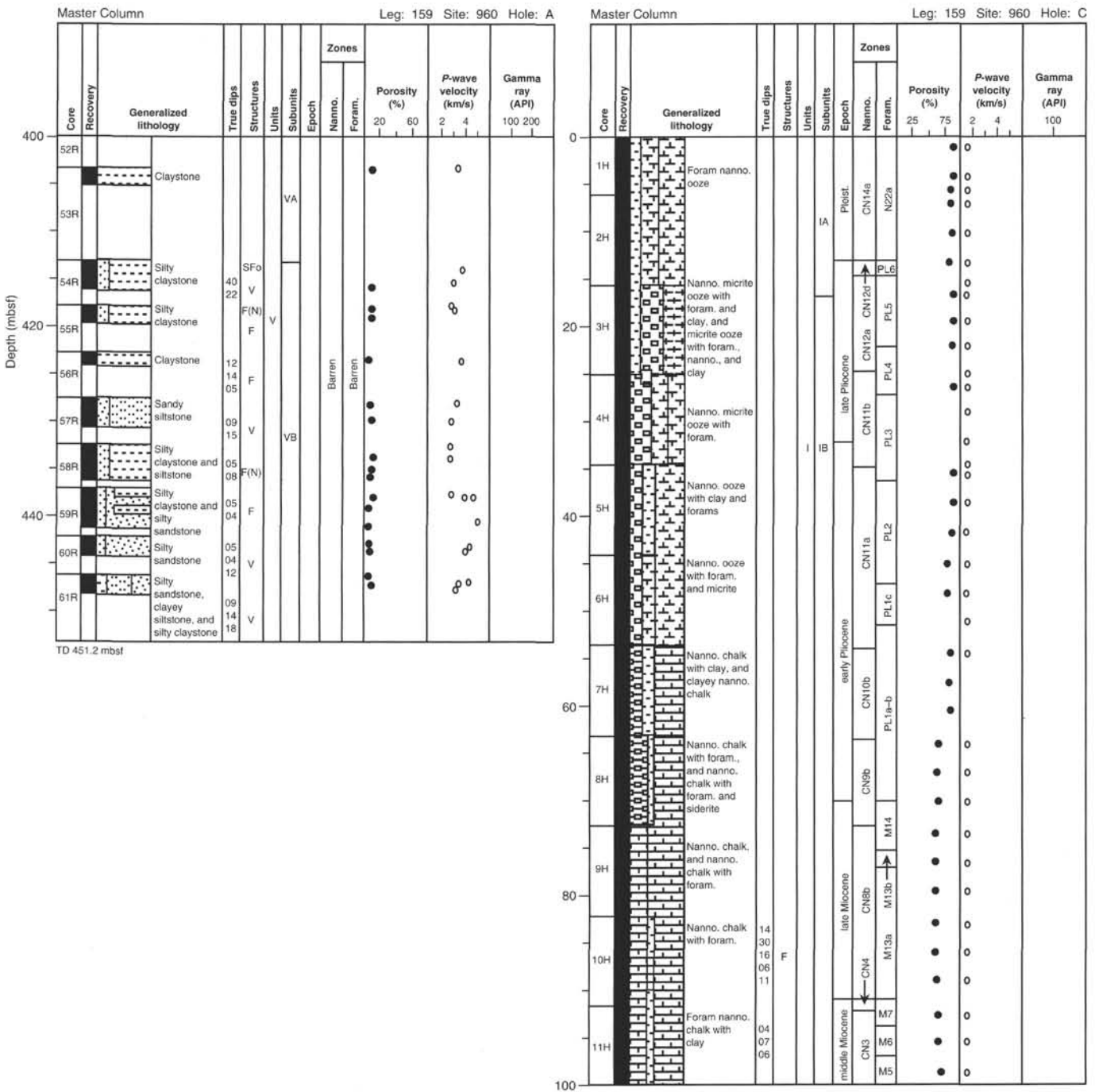


Figure 1 (continued).

ocene). The oldest hiatus is within Core 159-960C-23X, between assemblages assignable to early Eocene Zone CP9 and others of Coniacian to Santonian age.

Magnetic measurements indicate three distinctive transitions in magnetic properties, which can be correlated between Holes 960A and 960C, and Site 959. A sharp increase in NRM intensity and in bulk susceptibility occurs at the upper/lower Pliocene boundary (32 mbsf in Hole 960C, 20 mbsf in Hole 960A). A drop in intensity of magnetization and in susceptibility is encountered at 92 mbsf in Hole 960C and at 74 mbsf in Hole 960A, corresponding to a major hiatus between the upper Miocene and lower middle Miocene. An unconformity is seen at 329 mbsf in Hole

960A, where both the intensity of magnetization and the bulk susceptibility increase significantly. The remanence direction, where measured, is dominated by a drilling-induced component, the character of which alternates in successive cores. This alternation corresponds to the sequential use of two separate APC inner core barrels, which may be inducing the magnetization. Demagnetization to 25 mT does not isolate a high coercivity component, but does define a great-circle trajectory, suggesting that a high coercivity component is present, which may be determined by cleaning in stronger fields.

At 0-100 mbsf, microbial degradation of organic matter drives the sequential reduction of manganese, iron, and sulfate in the sediment, with

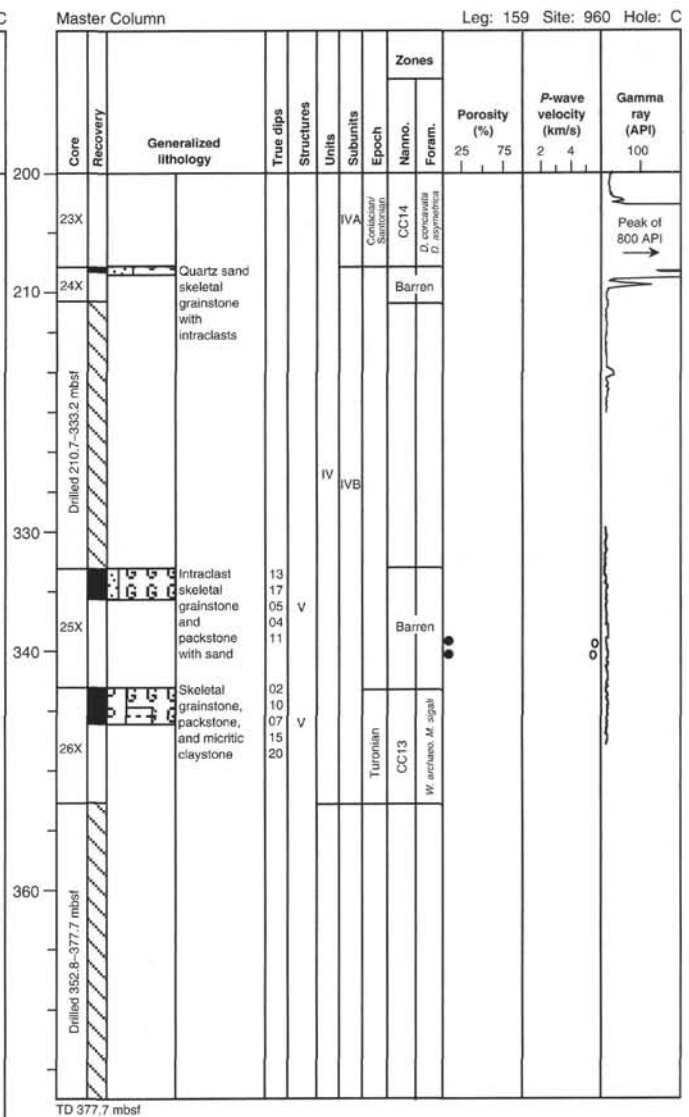
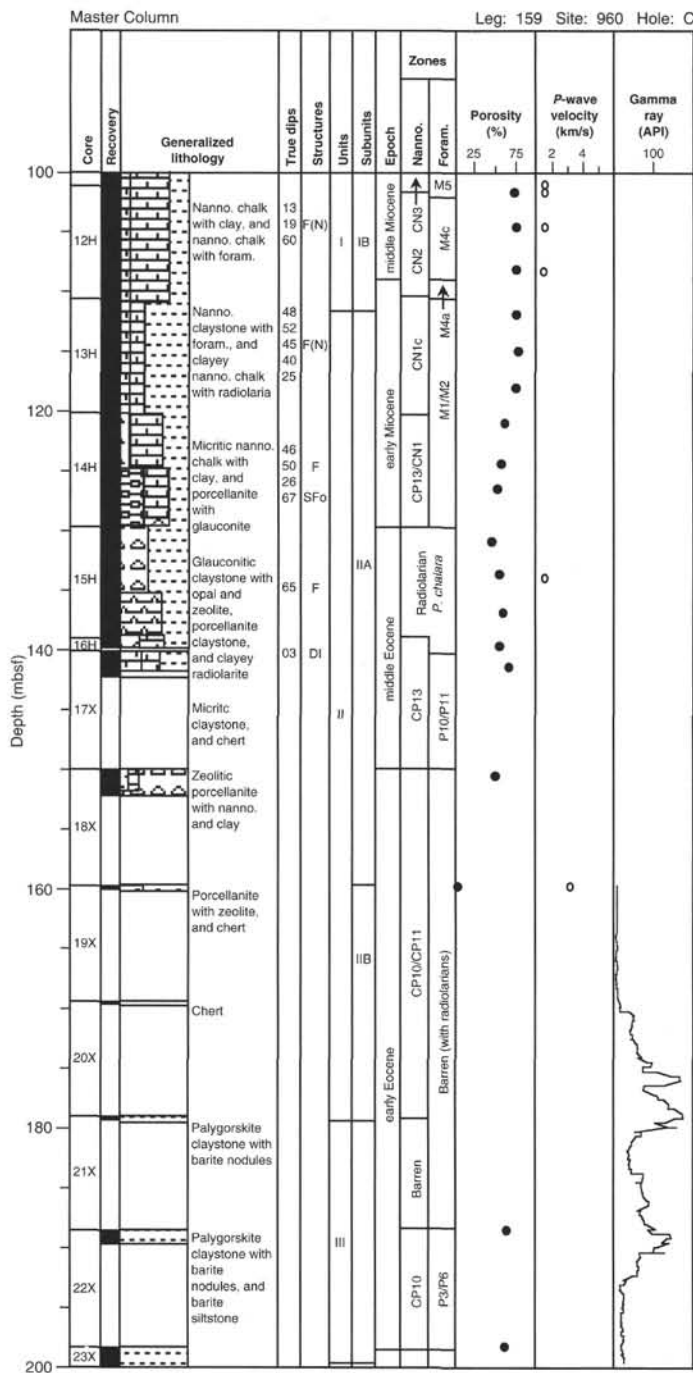


Figure 1 (continued).

these reactions occurring at less than 10 mbsf, 10 mbsf, and approximately 30 mbsf, respectively. Below 100 mbsf, the small number of samples precludes making a detailed interpretation of pore-fluid chemistry, but alkalinity and ammonium data indicate that the deeper sediments at Site 960 are less influenced by organic matter degradation. Profiles of dissolved Ca, Mg, and Sr reflect major differences between pore-fluid chemistry at Sites 959 and 960. At Site 960, no minimum in dissolved Ca occurs. Mg decreases and Sr increases downhole, suggesting carbonate recrystallization but not carbonate precipitation.

Organic carbon contents range from 0 to 6.44 wt%, and carbonate contents from 0 to 98 wt%. These are controlled by paleoenvironmental con-

ditions and/or degree of diagenesis. Intermediate carbonate contents (35–55 wt%), elevated C/N ratios (10–14), and low hydrogen indices (<100 mgHC/gTOC) are seen in the upper Pliocene to Pleistocene sediments. An increase in organic carbon (5.6 wt.%) correlates to a drop in carbonate (0 wt%) at the Miocene/Pliocene boundary. A very high C/N ratio and a low hydrogen index suggest deposition of terrestrial, oxidized organic matter. Early Eocene to early Miocene chalks and claystones indicate a mixed marine/terrestrial source for the organic matter, whereas the underlying limestone unit has no organic carbon. Highly variable organic carbon records with peak contents above 2 wt% and minimum carbonate contents are characteristic of lithologic Unit V. Low hydrogen indices and C/N ra-

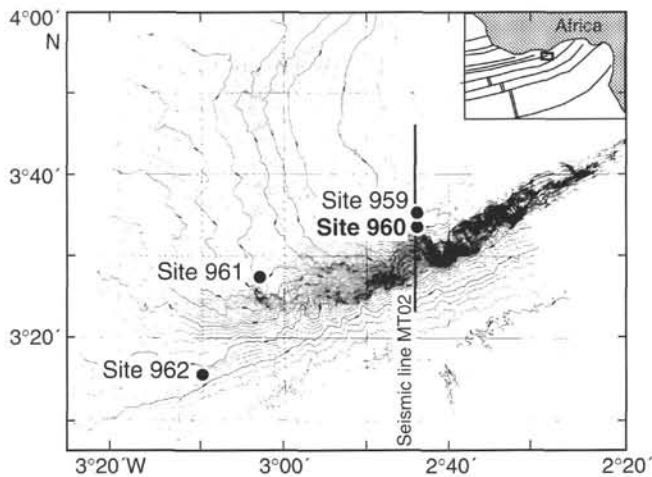


Figure 2. Location of Site 960 on a swath bathymetric map (*Equamarge II* cruise, 1988; Mascle et al., 1989) of the CIGMR and surroundings (bathymetry is in meters; contour interval 50 m). Site 960 is located on migrated MCS Line MT02, 3 mi south of Site 959, almost on top of the CIGMR.

to indicate a terrestrial source. T_{max} values suggest a mixture of immature (below 365°C) and overmature (above 450°C) organic matter.

Natural gamma measurements from core are low at 0–100 mbsf, then rise due to increasing glauconite content. Natural gamma is also high in the palygorskite clay of lithologic Unit III. P -wave velocity is 1.5 km/s in lithologic Units I and II, increasing to 4.0–6.0 km/s in the limestones of lithologic Unit IV, but falling again to 2.5–4.5 km/s in the claystones and sandstones of lithologic Unit V. P -wave velocity also peaks at the late to middle Miocene boundary. No lithologic change is noted, but biostratigraphic evidence indicates a disconformity.

The Quad combination tool string covered the interval 361.3–73.3 mbsf in Hole 960A. Only one third of the logged open hole interval was of a diameter less than 16 in. (as shown by the caliper curve), and these conditions seriously affected the quality of the sonic, density, and porosity data collected by the Quad tool string. Resistivity and gamma-ray data were affected to a much lesser degree. The FMS and GLT tool strings were not run in Hole 960A. In Hole 960C a natural gamma, resistivity, and sonic tool string was run over 121.2–92.4 mbsf and 374.6–159.7 mbsf. Again, the caliper curve indicated washed-out conditions for over half of the logged interval, resulting in poor quality sonic data. The FMS was run but was unable to get past a bridge and so covered the interval 354.5–173.7 mbsf. Data quality was understandably poor but may improve when processed on shore.

BACKGROUND AND OBJECTIVES

Site 960 is located 3 miles south of Site 959 in 2061 m water depth on a small plateau that occupies the summit of the Côte d'Ivoire-Ghana Marginal Ridge (CIGMR) at 2000 mbsf (Fig. 2).

Site 960 had been selected as a backup site for the structurally deep targets we hoped to document at Site 959; the backup site was designed in case of safety problems caused by high hydrocarbon concentrations and potential reservoirs in seismic Unit D (see Basile et al., this volume, for discussion of seismic stratigraphy). Hydrocarbon traps resulting from progressive pinch-out were possible according to the seismic data. Possible source rocks (black shales) were also anticipated within lower Units C to A, which were inferred to be of middle to Late Cretaceous age (Mascle et al., 1988, 1993). Immature source rocks were encountered during Site 959 drilling (see "Organic Geochemistry" section, "Site 959" chapter, this volume); however, these sediments did not pose any safety problems. Hole 959D was finally drilled into the upper parts of seismic Unit B at 1053 mbsf and

bottomed out at 1158.9 mbsf after documenting 105 m of Unit B. A very slow penetration rate (2–3 hr, avg) and poor recovery caused by severe bit damage halted operations at Site 959 (see "Operations" section, "Site 959" chapter, this volume).

To document the deepest target, seismic Unit A, two different options were offered: (1) set a reentry cone and casing at Site 959, and drill a new hole to approximately 1000 mbsf, at which level coring could have been restarted down to the depth objective of 1600 mbsf; (2) stop drilling operations and move to Site 960, where Unit A and possibly a thin sequence of Unit B were believed to be present and were covered only by a thin veneer of soft to semi-indurated sediments.

For both scientific (to determine the provenance of the clastic shallow-water sediments recovered from seismic Unit B in Hole 959D) and for technical and logistical reasons we favored option 2.

At Site 960 an MCS line indicated a drastic thinning of all formations overlying seismic Unit A, and which were recovered at Site 959 (Fig. 3). At Site 960 the total thickness of soft to semi-indurated sediments (Units C to F) was estimated to be on the order of 250–280 m, according to seismic interval velocity analysis (velocities between 1.6 and 2.3 km/s; Fig. 4). Such thinning may be related to strong bottom current activities (Atlantic Intermediate Water flow) near the ridge top that prevent or drastically reduce deposition. Sedimentary thickness reduction appeared, however, to result from the progressive pinch-out of Units C to E toward the ridge top, as seen on the seismic survey (Figs. 3 and 4). At this site Unit B could hardly be distinguished from deeper seismic sequences, possibly due to its progressive thinning upslope onto the basement high or because it comprises a comparable sedimentary facies. It was anticipated that Unit B, if present, would consist of indurated coarse clastics that are strongly affected by syntransform tectonics. Unit A shows an almost reflection-free acoustic character. Migrated MCS sections (Fig. 3) image a few internal and more continuous reflectors, which indicate a sedimentary origin for the unit. Unit A was expected to be as thick as 2.5 km, according to seismic wide-angle data modeling (Sage, 1994). Deep dives EN08, EN09, EN10, and EN12 of the *Equanaute* campaign provided observations and in situ sampling of Unit A, only 4–5 mi away downslope from Site 960 (Fig. 5). We believed that Unit A consisted of a thick, cyclic succession of sandstones, siltstones, and indurated clays of very shallow environment (Guiraud, et al., in press a, b).

Objectives

Transform Margin Evolution

The primary scientific objective at Site 960 was to document the stratigraphically deepest unit of the CIGMR (Unit A), which was not drilled at Site 959. The aim was to sample Unit A as continuously as possible, and potentially Unit B, which it was hoped would provide constraints on the timing and nature of the tectonic regime operating along the transform. Tectonic models suggested that the CIGMR was deformed differently during two distinct periods of time; extensional deformation is recorded by microstructures during and after lithification of Unit A, as shown by detailed microstructural analysis of samples collected by deep dives on the ridge slope (Guiraud, et al., in press a, b); syntransform-related tectonics were expected to be preserved in sediments of both Units A and B, probably in the form of cleavages, and/or as microscale shear folds. Finally both clastic sequences should have recorded any subsequent tectonism, such as differential-subsidence-related extension, or even a more general collapse of the ridge. A reconstruction of the past thermal history of the CIGMR was one of the major goals of Site 960. Apatite fission track studies performed on coarse-grained sandstones from Unit A collected during the *Equanaute* deep dives (Bouillin et al., 1994) showed that the thick sedimentary pile of the CIGMR was heated above 120°C and then cooled below 60°C some time between the Late Cretaceous and early Eocene. Key questions to be addressed included the origin of the heating and cooling (e.g., sediment burial, tectonism,

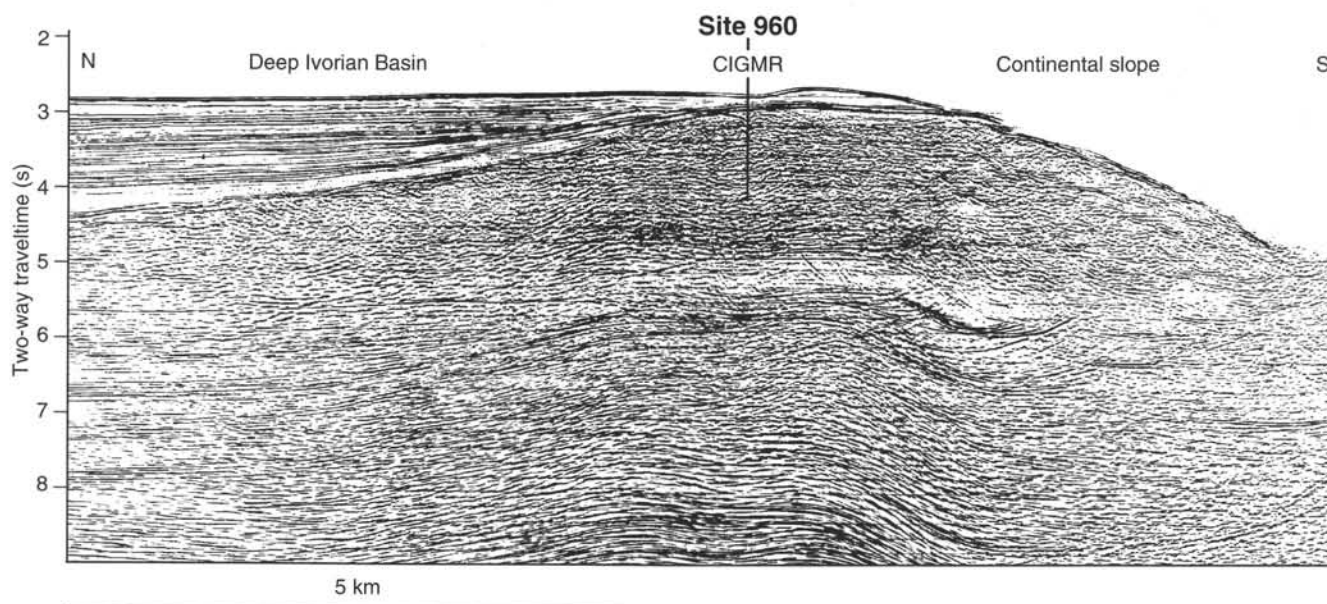


Figure 3. Migrated MCS section of Line MT02 (*Equasis* cruise, 1990; Mascle et al., 1995) across the CIGMR showing location of Site 960; vertical scale is in seconds of two-way traveltime.

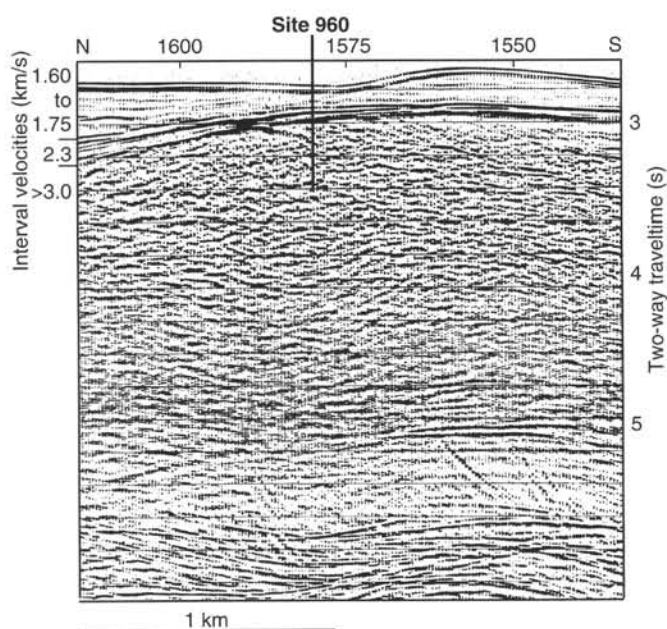


Figure 4. Enlargement of MCS Section MT02 at Site 960 showing a reduced sedimentary cover unconformably overlying a strongly diffractive seismic surface, interpreted as an erosional surface overlying Units A and B. If Unit B is present, it cannot be distinguished from Unit A on the basis of seismic character and seismic interval velocities alone.

oceanic lithospheric heating, tectonic or erosional unroofing), the reaction of the margin to these processes (uplift, subsidence, gravitational collapse), and the degree to which the sediments were affected. These questions were expected to be answered by comparing the fission track histories from Site 960 to the *Equanaute* dives, reconstructing the subsidence or uplift history of the CIGMR (deduced from dating, sedimentology, and interpretation of the seismic profiles) and by analyzing microstructures in thin section.

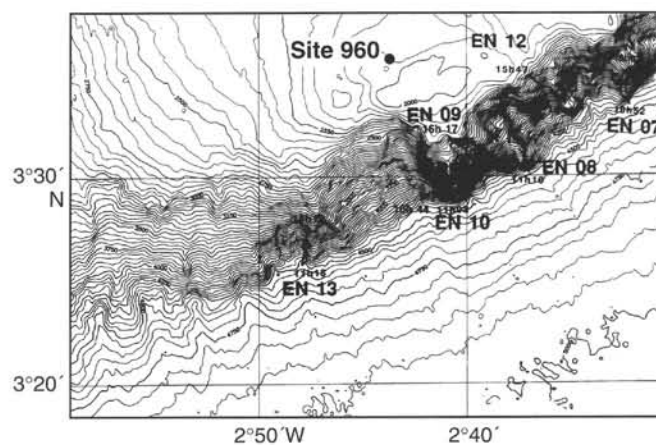


Figure 5. Locations on swath bathymetric map of deep dives EN7, EN8, EN9, EN10, and EN12, performed downslope, 4 to 6 mi from Site 960. Unit A is directly exposed along the slope, where it consists of shallow-water deltaic clastic sediments (after Mascle et al., 1993).

Paleoceanographic Objectives

An unanticipated objective of Site 960 was to compare through time sedimentary environments for both the Deep Ivorian Basin (Site 959) and the crest of the CIGMR (Site 960). We thought this would help us to understand the role of the ridge in acting as a dam to sedimentation in the basin itself. Furthermore, the ridge may have been the source of the shallow-water carbonates recovered from the deepest level cored at Site 959, in which case drilling at Site 960 might sample these sediments at their point of origin.

After RCB coring at Site 960, it became apparent that sediments at this site could provide additional information on two other paleoceanographic subjects, particularly if we could recover a record relatively undisturbed by coring: (1) Barite, palygorskite, and sepiolite are common in the sediments just above the carbonates cored at this site; by characterizing the depositional and diagenetic envi-

ronments associated with these minerals we hoped to determine their origin, specifically whether they are detrital or authigenic; (2) a distinctive hardground was identified, marking the unconformity between Eocene and Cretaceous sediments; its character was expected to provide information about early Cenozoic sedimentation in this area.

OPERATIONS

The transit to Site 960 from Site 959 was made in dynamic positioning (DP) mode because of the short distance (2.7 nautical miles) between the two sites. No site survey was required, and the site, which was originally planned as an alternate to Site 959, was located using the GPS navigation system. Once the drill string was clear of the seafloor at Site 959 and the positioning beacon had been recovered, the vessel began moving to Site 960. The bottom-hole assembly (BHA) for Hole 960A was the same as that used on Hole 959D. As the vessel arrived on location the BHA was being assembled, and rotary core barrels (RCB) were spaced out. The positioning beacon (Datasonics Model 354B, 15 kHz, 208 db, SN 779) that was recovered from Site 959 was deployed, thus initiating Hole 960A at 0630 hr on 24 January 1995.

Hole 960A

The RCB BHA was run in the hole and at 1200 hr, 24 January, Hole 960A was spudded, with the mud line established at 2059.7 m by direct pipe measurement (DPM). The corrected precision depth recorder (PDR) reading normalized to driller's datum was 2048.4 m. The discrepancy was attributed to the difficulty in "feeling" for bottom with the drill pipe and RCB core bit. RCB coring continued at a fairly rapid rate in the upper, softer sediments; however, recovery varied erratically, averaging less than 30% for the first 280 mbsf. The presence of poorly consolidated nannofossil oozes and claystones, followed by hard cherts and weakly cemented limestones, was thought to be the primary contributor to the core recovery problems. The condition of the hole was excellent.

At approximately 2394 m drill pipe depth (334 mbsf), in Core 159-960A-37R, the contact between seismic Units A and B was recovered. Recovery was surprisingly good in the sandstone/shale interbeds below this contact, with two black shale cores recovering 99%. The rate of penetration continued to deteriorate, however, ranging from 0.7 to 1.4 m/hr. Although core diameter and recovery were good, erosion was evident on the softer cored material, indicating the bit seal was likely no longer effective. It was decided that the depth objective would not be attainable with the initial bit. Coring was therefore suspended with bit No. 1, an RBI CC-4 (SN BG255), at a depth of 2457.0 m (397.3 mbsf), and a free fall funnel (FFF) was deployed at 1515 hr, 28 January. The drill string was recovered and the bit reached the rig floor at 2100 hr that same day. The bit was found to be in poor condition with two cones extremely loose, two cones locked up, and two jets plugged, although the cutting structure was undamaged. Bit balling and overload were evident, despite the high circulation rates (50–70 spm). Maximum weight on bit (WOB) had been 35,000 lbs, although the majority of the coring was done with 25,000–30,000 lbs WOB.

Because the cutting structure on the RBI CC-4 core bit was in good condition but rate of penetration (ROP) was poor, and bit balling was evident, an RBI CC-3 core bit (SN BG254) was selected for the next bit run. The RCB BHA was again run in the hole and at 0315 hr, 29 January, after 15 min of camera scanning, Hole 960A was reentered. The pipe was run to 2366.3 m (306.6 mbsf) and the top drive was then picked up. The pipe was washed/reamed to bottom, where 2 m of loose fill was evident. RCB coring resumed at 0700 hr, 29 January, and continued until 1630 hr, 30 January, when a depth of 2510.9

m (451.2 mbsf) was achieved (Table 1). Recovery ranged from 18% to 85%. The ROP ranged from 1.7 to 3.2 m/hr.

After circulating a 30-barrel Sepiolite mud pill, a wiper trip was made in preparation for logging. During the wiper trip, an overpull of 100,000 lbs was experienced at a depth of 2488 m (approximately 428 mbsf). Another tight spot requiring 30,000 lbs of overpull was identified between 2482 m and 2453 m (DPM; 393–422 mbsf). As a result, the top drive was picked up and the hole was reamed from 2458 m (398 mbsf) to bottom. Eight m of fill was encountered at the bottom of the hole. A second short wiper trip through the tight section of the hole was then made in an attempt to ensure good conditions for logging. No interference or drag was experienced during the second wiper trip. Two wireline runs were made to release the bit on bottom and reverse-shift the sleeve. A drift survey taken on the last wireline run indicated a hole deviation of 3.5° at TD. The lower 60 m of the hole was displaced with weighted mud, and the pipe was pulled to a logging depth of 2154.0 m (94.3 mbsf). At 0215 hr, 31 January, the logging sheaves were rigged and the Quad combination logging tool string was run into the hole but was unable to proceed farther than 2421.0 m (361 mbsf). Logs were attempted twice from this point up to 2135 m (75 mbsf); however, the calipers remained fully open throughout that interval, indicating that the hole was at least 17 in. in diameter. Based on this information, no further logging was attempted at this hole.

No hydrocarbons were detected at this hole; however, the hole was filled with weighted mud, according to accepted guidelines, and the drill pipe was pulled clear of the seafloor at 1245 hr, 31 January. After 1.5 hr was spent cutting and slipping the drill line, the pipe trip was resumed. The bit release reached the rig floor at 1700 hr, thus ending Hole 960A.

Hole 960B

Sediment quality and recovery were poor with the RCB coring system from the upper 200 mbsf of Hole 960A, but the sediment contained material of significant scientific value. Thus, we decided to spud a second hole at this site using the APC/XCB coring system. In so doing, we were hoping to determine if a PDC, drag-style, cutting structure on the bit would drill the formation faster than the TCI roller cone bits. We were hopeful that the recovery percentage and core quality would be improved as well. This information would be applicable to the drilling approach decided upon for the remaining two sites (961 and 962; proposed sites IG-2 and IG-3). An APC/XCB BHA was made up without a nonmagnetic drill collar, as it had been decided that core orientation would not be attempted on this hole in order to conserve the time for achieving a deeper penetration. The drilling assembly was terminated with a rebuilt, 10-1/8 in. RBI XCB PDC bit (SN BC376). The bit had 22 rotating hours prior to this deployment. At 2245 hr, 31 January, after the vessel moved 100 m to the north, Hole 960B was spudded and a single APC core recovering 7.15 m of mud-line sediment was taken. This established a mud-line depth of 2045.4 m (DPM). The corrected PDR reading normalized to driller's datum for this hole was 2047.4 m. A request from the curator at the Gulf Coast Repository for additional mud-line core material from this site led us to take only a single core at Hole 960B. Hole 960C, it was decided, would be taken to a greater depth. At 2245 hr, 31 January, Hole 960B was ended as the drill string was pulled clear of the mud line.

Hole 960C

The APC was again run in the hole and Hole 960C was spudded at 2330 hr, 31 January. Continuous APC coring continued into the following day until Core 159-960C-16H indicated an incomplete stroke. Sixteen APC cores were taken, recovering 105.5% of the section. Coring with the APC was terminated at a depth of 2186.5 m

Table 1. Coring summary for Site 960.

Core	Date (1995)	Time (UTC)	Depth (mbsf)	Length cored (m)	Length recovered (m)	Recovery (%)	Core	Date (1995)	Time (UTC)	Depth (mbsf)	Length cored (m)	Length recovered (m)	Recovery (%)
159-960A-							51R	Jan 28	1600	396.1-397.3	1.2	1.99	166.0
1R	Jan 24	1235	0.0-1.2	1.2	1.21	101.0	52R	Jan 29	1100	397.3-403.3	6.0	2.68	44.6
2R	Jan 24	1320	1.2-10.6	9.4	0.02	0.2	53R	Jan 29	1540	403.3-413.1	9.8	1.81	18.4
3R	Jan 24	1400	10.6-19.9	9.3	1.21	13.0	54R	Jan 29	1905	413.1-417.8	4.7	3.07	65.3
4R	Jan 24	1440	19.9-29.6	9.7	1.55	16.0	55R	Jan 29	2150	417.8-422.8	5.0	1.65	33.0
5R	Jan 24	1510	29.6-39.3	9.7	1.64	16.9	56R	Jan 30	0005	422.8-427.4	4.6	1.32	28.7
6R	Jan 24	1540	39.3-49.1	9.8	1.22	12.4	57R	Jan 30	0325	427.4-432.4	5.0	3.26	65.2
7R	Jan 24	1610	49.1-58.9	9.8	4.66	47.5	58R	Jan 30	0600	432.4-437.0	4.6	3.86	83.9
8R	Jan 24	1640	58.9-68.6	9.7	4.97	51.2	59R	Jan 30	1015	437.0-442.0	5.0	4.26	85.2
9R	Jan 24	1710	68.6-78.3	9.7	5.14	53.0	60R	Jan 30	1315	442.0-446.2	4.2	2.17	51.6
10R	Jan 24	1800	78.3-88.0	9.7	8.04	82.9	61R	Jan 30	1615	446.2-451.2	5.0	2.02	40.4
11R	Jan 24	1840	88.0-97.6	9.6	3.84	40.0	Coring totals:				451.2	145.01	32.1
12R	Jan 24	1930	97.6-107.3	9.7	9.30	95.9	159-960B-1H	Jan 31	2255	0.0-7.1	7.1	7.15	101.0
13R	Jan 24	2025	107.3-116.9	9.6	0.44	4.6	Coring totals:				7.1	7.15	101.0
14R	Jan 24	2100	116.9-126.6	9.7	0.71	7.3	159-960C-						
15R	Jan 24	2200	126.6-136.2	9.6	1.34	13.9	1H	Jan 31	2340	0.0-6.2	6.2	6.29	101.0
16R	Jan 24	2245	136.2-145.8	9.6	0.21	2.2	2H	Feb 1	0005	6.2-15.7	9.5	9.96	105.0
17R	Jan 24	2340	145.8-155.2	9.4	0.15	1.6	3H	Feb 1	0040	15.7-25.2	9.5	9.96	105.0
18R	Jan 25	0135	155.2-164.8	9.6	0.00	0.0	4H	Feb 1	0115	25.2-34.7	9.5	10.15	106.8
19R	Jan 25	0440	164.8-174.5	9.7	1.01	10.4	5H	Feb 1	0150	34.7-44.2	9.5	10.12	106.5
20R	Jan 25	0645	174.5-184.1	9.6	1.40	14.6	6H	Feb 1	0220	44.2-53.7	9.5	10.10	106.3
21R	Jan 25	0830	184.1-193.8	9.7	1.07	11.0	7H	Feb 1	0255	53.7-63.2	9.5	10.09	106.2
22R	Jan 25	0930	193.8-203.4	9.6	1.53	15.9	8H	Feb 1	0330	63.2-72.7	9.5	10.03	105.6
23R	Jan 25	1050	203.4-213.0	9.6	0.05	0.5	9H	Feb 1	0400	72.7-82.2	9.5	10.07	106.0
24R	Jan 25	1150	213.0-222.7	9.7	0.19	2.0	10H	Feb 1	0435	82.2-91.7	9.5	10.05	105.8
25R	Jan 25	1315	222.7-232.4	9.7	1.58	16.3	11H	Feb 1	0515	91.7-101.2	9.5	9.85	103.0
26R	Jan 25	1445	232.4-242.1	9.7	0.45	4.6	12H	Feb 1	0555	101.2-110.7	9.5	9.99	105.0
27R	Jan 25	1600	242.1-251.7	9.6	1.49	15.5	13H	Feb 1	0630	110.7-120.2	9.5	9.92	104.0
28R	Jan 25	1825	251.7-256.4	4.7	3.14	66.8	14H	Feb 1	0705	120.2-129.7	9.5	10.16	106.9
29R	Jan 25	2030	256.4-261.4	5.0	3.27	65.4	15H	Feb 1	0750	129.7-139.2	9.5	10.03	105.6
30R	Jan 25	2210	261.4-271.1	9.7	0.87	9.0	16H	Feb 1	0835	139.2-140.2	1.0	0.89	89.0
31R	Jan 25	2330	271.1-280.7	9.6	1.19	12.4	17X	Feb 1	0935	140.2-150.0	9.8	2.11	21.5
32R	Jan 26	0115	280.7-290.3	9.6	1.91	19.9	18X	Feb 1	1015	150.0-159.7	9.7	2.13	21.9
33R	Jan 26	0240	290.3-299.6	9.3	0.91	9.8	19X	Feb 1	1110	159.7-169.4	9.7	0.37	3.8
34R	Jan 26	0445	299.6-309.2	9.6	1.43	14.9	20X	Feb 1	1200	169.4-179.0	9.6	0.20	2.1
35R	Jan 26	0645	309.2-318.9	9.7	1.13	11.6	21X	Feb 1	1300	179.0-188.6	9.6	0.37	3.9
36R	Jan 26	0810	318.9-328.5	9.6	1.07	11.1	22X	Feb 1	1430	188.6-198.3	9.7	1.07	11.0
37R	Jan 26	1130	328.5-338.2	9.7	2.13	21.9	23X	Feb 1	1600	198.3-207.9	9.6	0.73	7.6
38R	Jan 26	1515	338.2-347.9	9.7	5.42	55.9	24X	Feb 1	1700	207.9-210.7	2.8	0.44	15.7
39R	Jan 26	1700	347.9-348.3	0.4	0.00	0.0	25X	Feb 2	1245	333.2-343.2	10.0	2.50	25.0
40R	Jan 26	2015	348.3-351.0	2.7	2.76	102.0	26X	Feb 2	1620	343.2-352.8	9.6	3.09	32.2
41R	Jan 26	2300	351.0-353.5	2.5	2.41	96.4	***Drilled from 210.7 to 333.2 mbsf***						
42R	Jan 27	0145	353.5-357.5	4.0	1.90	47.5	***Drilled (no coring) from 352.8 to 377.7 mbsf***						
43R	Jan 27	0545	357.5-362.3	4.8	3.43	71.4	Coring totals:				230.3	160.67	69.8
44R	Jan 27	1015	362.3-367.2	4.9	3.82	77.9	Drilled:				147.4		
45R	Jan 27	1300	367.2-371.8	4.6	3.68	80.0	Total:				377.7		
46R	Jan 27	1615	371.8-376.8	5.0	5.42	108.0							
47R	Jan 27	1835	376.8-379.3	2.5	2.63	105.0							
48R	Jan 27	2350	379.3-386.4	7.1	5.56	78.3							
49R	Jan 28	0620	386.4-391.1	4.7	2.05	43.6							
50R	Jan 28	1150	391.1-396.1	5.0	6.37	127.0							

DPM (140.2 mbsf). XCB coring resumed with Core 159-960C-17X, and by 1730 hr, 1 February, a cored depth of 2257.0 m DPM (210.7 mbsf) was attained. Recovery for the eight XCB cores was generally poor, ranging from 2% to 22%, and the co-chief scientists agreed that the area of interest had been cored to a sufficient depth. Given time limitations for the remainder of the leg, it was decided to drill ahead with the XCB PDC bit and center bit to identify what ROP might be achievable. If a fast enough drilling rate could be sustained, the desire was to take Hole 960C to a total depth of 350-400 mbsf and attempt to obtain the logging data (primarily FMS) that was not attained in Hole 960A.

Drilling proceeded for 16.75 hr until a depth of 2379.5 m DPM (333.2 mbsf) was reached. For the first 6-7 hr of drilling, a penetration rate of 16 m/hr was achieved. This slowed to slightly faster than 10 m/hr for the final 10 hr. Two XCB cores (159-960C-25X and 26X) were cut in an attempt to again core through the boundary of the A/B seismic units. After recovery of these cores, drilling was resumed and continued to a depth of 2424.0 m or 377.7 mbsf (Table 1), where the ROP slowed to 4.3 m/hr, so the decision was made to terminate the hole. The hole was circulated with a 30-barrel Sepiolite mud pill, and the center bit was recovered via the sandline. During the final sandline run, a multishot deviation survey was taken indicating a hole drift of 2.5°-3.0° at TD. A wiper trip up to 81.7 mbsf was made, with no

indication of any hole problems. Approximately 1 m of fill was identified on bottom, which was reamed through and circulated out of the hole. At 0445 hr, 3 February, preparations for logging began. As there was little interest on the part of the scientific party for anything other than FMS logs, and there was concern over hole deterioration with time, a request was made to LDEO for permission to make the FMS the first and only logging run. This was discouraged by LDEO, and it was decided to take the extra time required to run the Quad combination tool string first. The nuclear source was left out to minimize the risk of losing additional time should the tool be lost in the hole. During the first logging run, the tool string stopped at 2170 m (123.7 mbsf), and was unable to reach any deeper. The tool string was recovered and the drill pipe was lowered to 2215 m (168.7 mbsf) without incident. The Quad combination tool string was again run into the hole and was able to get to within 4 m of hole TD (377.7 mbsf). Logs were obtained from this point up to drill pipe depth. Based on caliper data it appeared that, again, much of the hole was washed out and eroded to at least 17 in. in diameter, despite the low flow rates (50 SPM max) used, and the relatively few hours the hole had been open and exposed. Nonetheless, the FMS logging tool string was deployed, reaching a depth of 2400 m or 24 m from TD. Upon conclusion of the logging program, the pipe was lowered to 2390 m and the hole was displaced with heavy mud. The pipe was

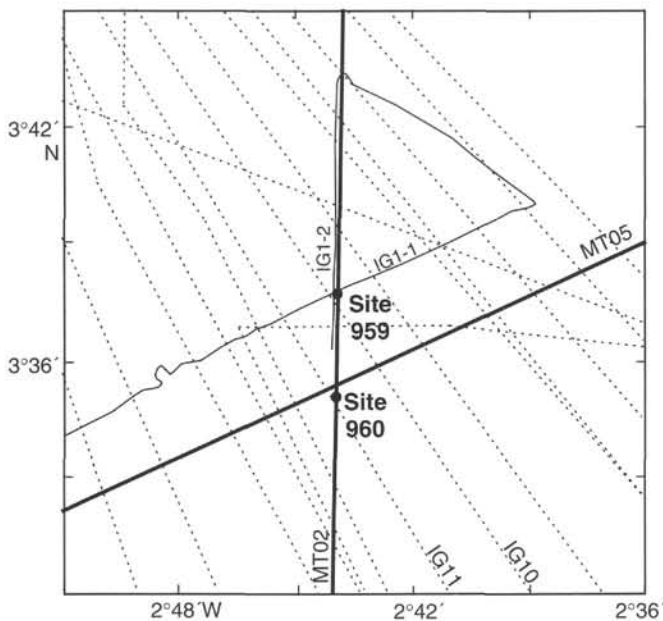


Figure 6. Track chart showing the location of Sites 960 and 959 and the seismic data available in the area. Thick lines correspond to multichannel data acquired during the *Equasis* program of 1990, dashed lines denote single-channel data of the *Equamarge II* program (1988), and thin lines show data collected at the beginning of Leg 159.

pulled out of the hole, clearing the seafloor at 2215 hr, 3 February. The positioning beacon was released and recovered, with the bit reaching the rig floor at 0230 hr, 4 February, thus ending Hole 960C.

Results with the XCB PDC bit had been encouraging enough to consider deployment of the RCB PDC anti-whirl version on Site 961 (proposed site IG-2).

SITE GEOPHYSICS

Site 960 is located at proposed Site IG1-bis, near the summit of the Côte d'Ivoire-Ghana Marginal Ridge. This site was initially an alternative for Site 959, and as such, was not included in the site seismic survey shot at the beginning of Leg 159. However, both single (IG11) and multichannel (MT02, MT05) seismic data were already available from lines located close to the site (Fig. 6). These data all allow the identification of a thin sedimentary cover over acoustic basement. While the multichannel data are more penetrative, the single-channel data provide slightly better resolution in the uppermost part of the section.

Integration of Seismic Profiles and Site Observations

Although sonic data were recorded during the downhole logging of Hole 960C, the large hole diameter meant that these data are too poor in quality to warrant further processing or interpretation (see "Downhole Measurements" section, this chapter). Therefore, the only available velocity data are discrete physical properties measurements (see "Physical Properties" section, this chapter). The conversion from two-way traveltimes to depth is based on the measured vertical velocities. Two clear reflectors could be determined on the seismic profiles. The depth estimates of these reflectors are summarized in Table 2 and the tie of Site 960 to seismic Lines IG11, MT02, and MT05 is shown in Figure 7.

Table 2. Depth of reflectors at Site 960.

Reflector	Time (s TWT)	Depth (mbsf)	Origin of reflector*
R1	0.17	140	Chert, top of lithologic Subunit IIB
R2	0.24	330	Transition from limestone (lithologic Subunit IVB) to claystone (lithologic Unit V)

Note: *See "Lithostratigraphy" section, this chapter.

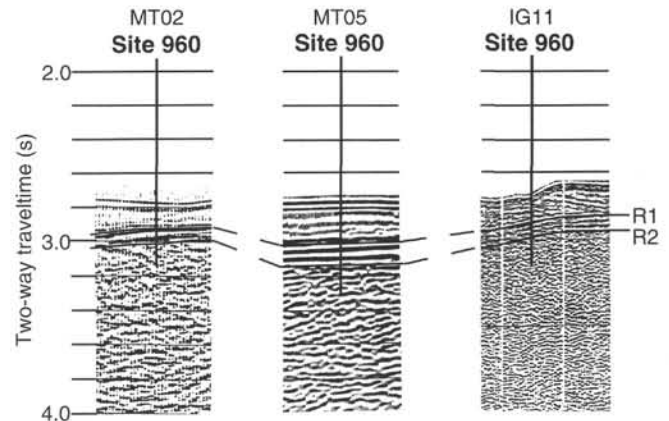


Figure 7. Ties of the principal reflectors observed on multichannel Lines MT02 and MT05 and single-channel Line IG11 to Site 960.

Reflector R1: 0.17 s TWT Below Seafloor

This corresponds to a strong, laterally continuous reflector that marks the base of an acoustically transparent sediment package below the seafloor. This reflector corresponds to the top of lithologic Subunit IIB (see "Lithostratigraphy" section, this chapter) and represents the interface between chalk and porcellanite (lithologic Subunit IIA) and underlying chert. The depth of this interface is 136 mbsf in Hole 960A and 165 mbsf in Hole 960C. Multichannel seismic Line MT05, located just north of Site 960 (Fig. 6), shows a slightly thicker sedimentary sequence above Reflector R1 than is observed at the intersection of the site with Line MT02. This agrees well with observations at Hole 960C (located approximately 90 m north of Hole 960A) where the top of the chert (lithologic Subunit IIB) is located at 165 mbsf, as opposed to 136 mbsf at Hole 960A.

Reflector R1 defines the top of a thin, less than 0.1-s-TWT-thick layer characterized by bright, laterally continuous reflectors. The base of this unit is defined by Reflector R2.

Reflector R2: 0.24 s TWT Below Seafloor

Reflector R2 marks an abrupt change in acoustic facies from the bright, well layered reflectors below Reflector R1 to an acoustic basement devoid of continuous events. This reflector corresponds to the top of lithologic Unit V, at 329 mbsf (Hole 960A). The transition from lithologic Units IV to V represents an unconformity between Turonian quartz sand limestones of lithologic Subunit IVB to sandstones, siltstones, and claystones of unknown age at the top of lithologic Unit V. From the discrete velocity measurements (see "Physical Properties" section, this chapter) the vertical *P*-wave velocity can be seen to decrease from approximately 5.0 km/s above this interface to between 3.0 and 4.0 km/s below. Lithologic Unit V corresponds to seismic Unit A.

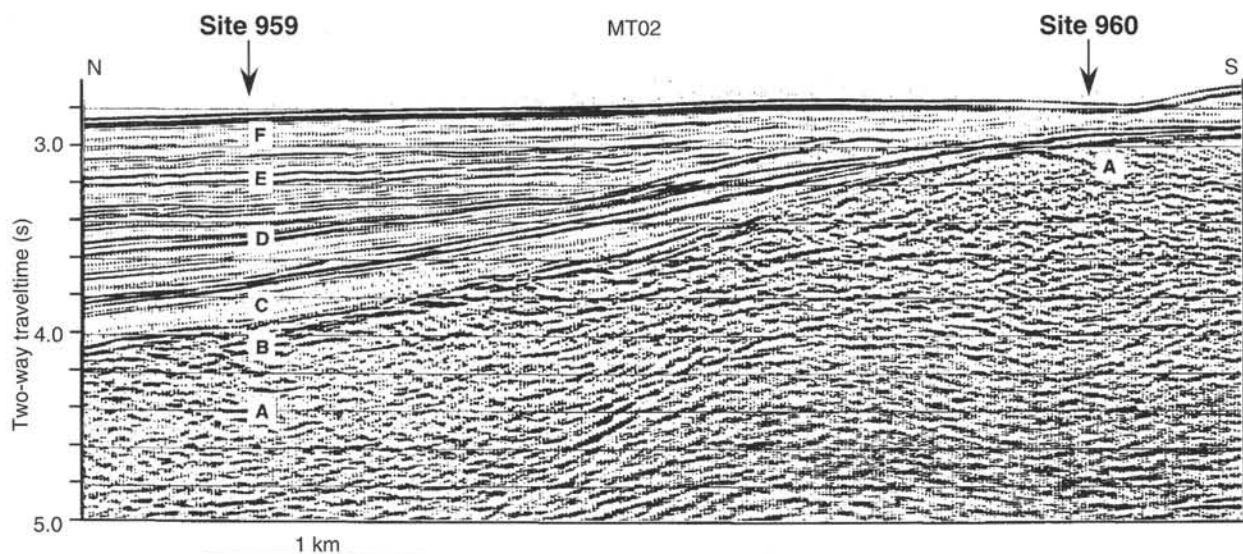


Figure 8. Multichannel seismic Line MT02 showing the progressive pinch-out between Sites 959 and 960 of seismic Units B through F against the CIGMR.

From these results it becomes apparent that the top of lithologic Subunit IVB cannot be resolved from lithologic Subunit IIB, Unit III, and Subunit IVA on the seismic reflection profiles. Lithologic Unit III comprises palygorskite claystone underlying the chert of lithologic Subunit IIB, while lithologic Subunit IVA is composed of glauconitic claystone and micritic chalk. These layers are too thin (in Hole 960A, lithologic Subunit IIB is 28.6 m thick, Unit III is 20.5 m thick, and Subunit IVA is 9.6 m thick) to be resolved by the seismic wavelet, which has a wavelength of 40 to 100 m for velocities of 1.5 to 4.0 km/s. The base of Hole 960A (451 mbsf) corresponds to 0.31 s TWT.

Comparison with Site 959

Sites 959 and 960 are linked by multichannel seismic profile MT02 (acquired during the *Equasis* survey of 1990), which runs north-south (Fig. 6). Examination of this multichannel line (Fig. 8) shows a rapid thinning of the upper seismic units (above seismic Unit A) from Site 959 to Site 960. The thickness of the sediments above seismic Unit A is reduced from more than 1158 m at Site 959 to 329 m (Hole 960A) at Site 960. This thinning is largely the result of the pinch-out of seismic Units C to E against the slope of the CIGMR. Seismic Unit F (which corresponds to lithologic Unit I and comprises nannofossil/foraminifer ooze and chalk) is reduced in thickness from a maximum of 208 m at Site 959 to 111 m at Site 960 (see "Lithostratigraphy" section, this chapter). At both sites this unit is represented on the seismic profiles by largely transparent seismic facies. Underlying seismic Units E through C are represented by just 85 to 97 m of sediment at Site 960. These condensed sequences are a function of the elevated position of the CIGMR, which led to a reduced sedimentation rate coupled with increased erosion from the ridge top (see "Lithostratigraphy" section, this chapter).

On the seismic reflection profiles it is difficult to recognize seismic Unit B toward the top of the CIGMR, as it too appears to thin considerably as the ridge top is approached. From the integration of the seismic data with the lithology at both Sites 959 and 960 it seems reasonable to correlate seismic Unit B with lithologic Unit IV at Site 960, which comprises limestones of Turonian to Santonian age.

LITHOSTRATIGRAPHY

Three holes were drilled at Site 960, which lies on the north side of the Côte d'Ivoire-Ghana Marginal Ridge as discussed in the

"Background and Objectives" section (this chapter). Hole 960A was drilled in 2059.7 m of water and 451.2 m of section was penetrated by RCB drilling. APC coring recovered 7.1 m from Hole 960B at a water depth of 2045.4 m (this mud-line core was archived and is not discussed further in this chapter). Hole 960C (2046.3 m water depth) was cored with a combination of methods: using APC, 0.0 to 140.2 mbsf was cored and Cores 159-960C-1H through 16H were recovered; using XCB, 140.2 to 210.7 mbsf was drilled and Cores 159-960C-17X through 24X were recovered; the interval from 210.7 to 333.2 mbsf was drilled without coring; the interval from 333.2 to 352.8 mbsf was XCB cored and Cores 159-960C-25X and 26X were recovered; drilling without coring continued to a total depth of 377.7 mbsf. This series of holes provided 451.2 m of the stratigraphic section ranging in age from Quaternary through Late Mesozoic.

Based on lithologic variations compiled from Holes 960A and 960C, five lithologic units were identified (Figs. 9, 10; Table 3). Lithologic Unit I comprises calcareous sediments of Pleistocene to early Miocene age. Nannofossil/foraminifer ooze in the upper part of the section (lithologic Subunit IA) is replaced by nannofossil/foraminifer chalk with depth (lithologic Subunit IB). The first downhole appearance of siliceous microfauna and -flora marks the upper boundary of lithologic Unit II, which has a lithology characterized by radiolarian/nannofossil chalk, claystones, and porcellanites of early Miocene to early Eocene age and chert of early Eocene age. The base of lithologic Unit II and the top of lithologic Unit III are marked by the last downhole occurrence of chert and the presence of a palygorskite-rich claystone interval containing barite concretions and nodules. This unit is distinctive in its bluish green color, its high natural gamma emission (see "Physical Properties" section, this chapter), and the co-occurrence of abundant authigenic barite. Lithologic Subunit IVA is a condensed/hiatal interval containing abundant fish debris, hardgrounds, glauconitic claystones and micritic chalks. The age of this subunit encompasses Maastrichtian through Santonian/Coniacian time over a stratigraphic thickness of less than 10 m. Lithologic Subunit IVB is a calcareous interval composed of quartz sand and intraclastic limestones, skeletal packstones and grainstones, and sandy/silty limestones. The top was identified as the first downhole occurrence of bioclastic and intraclastic limestones (containing variable amounts of quartz sand) and the disappearance downcore of glauconite and fish debris. In Hole 960A, this boundary is marked by a brecciated surface, where glauconitic sandstones overlie limestones that vary from quartz sand limestones to skeletal grainstones composed of oolitic and peloidal grains and red algal, molluscan, and

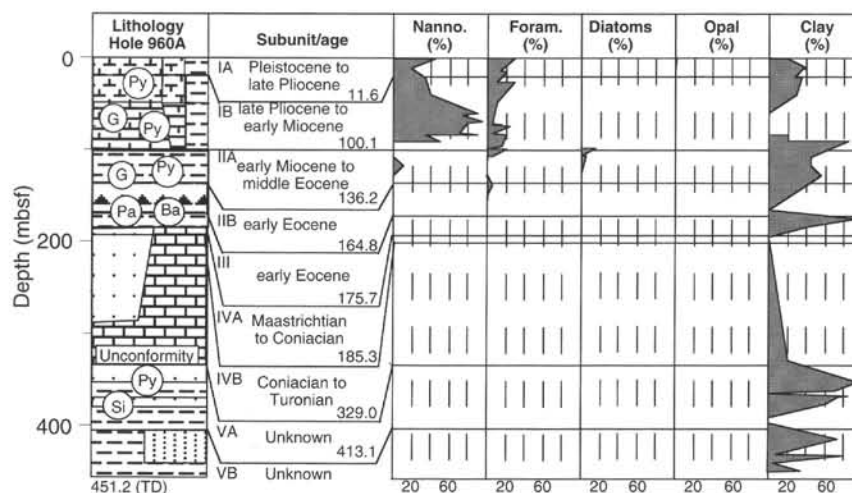


Figure 9. Stratigraphic column for Hole 960A.

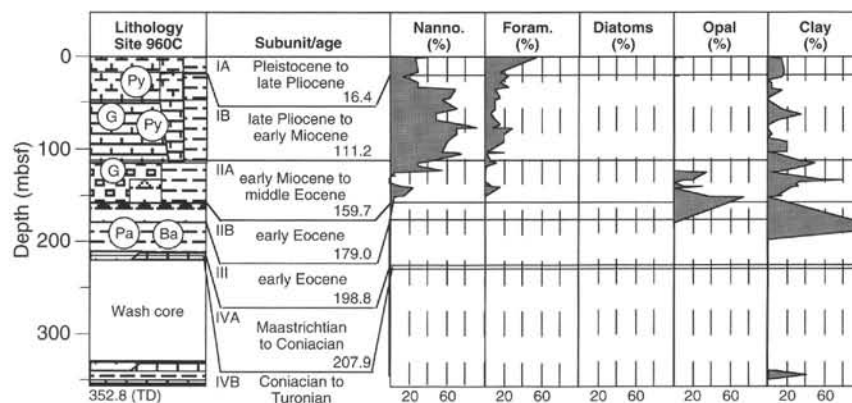


Figure 10. Stratigraphic column for Hole 960C.

echinoderm bioclasts. The age of lithologic Subunit IVB is Coniacian to Turonian. The lower boundary of this unit (observed only in Hole 960A) was placed where bioclastic limestones of lithologic Subunit IVB overlie lithologic Unit V. Lithologic Unit V was characterized by the dominance of siliciclastic sediments, which include carbonate-cemented quartz sandstones and siltstones in lithologic Subunit VA, changing to silty sandstones, siltstones, and clayey siltstones in lithologic Subunit VB. The age of this unit is unknown.

Description of Lithologic Units

Unit I

Description: Nannofossil ooze and chalk, foraminifer nannofossil ooze and chalk, nannofossil ooze with clay, and clayey micrite chalk with nannofossils
Interval: Sections 159-960A-1R-1, 0 cm, through 12R-2, 95 cm, and 159-960C-1H-1, 0 cm, through 13H-1, 55 cm
Depth: 0–100.1 mbsf, Hole 960A; 0–111.2 mbsf, Hole 960C
Age: Pleistocene to early Miocene

Lithologic Unit I at Site 960 is similar to but thinner than lithologic Unit I at Site 959, which is only 5 km to the southwest. As this unit is discussed in detail in the “Site 959” chapter, only a brief summary will be given here, with emphasis placed on differences within the unit between the two sites. Hole 960A was rotary cored, which yielded poor recovery and sediment highly disturbed by drilling. Hole

960C was cored with the APC, which yielded excellent recovery and a minimum of drilling disturbance. Consequently, much of this discussion is based on observations made on the sediment from Hole 960C.

Lithologic Unit I comprises dark to light gray, massive or laminated, calcareous pelagic ooze and chalk. It is divided into two subunits based on variation in color, which is a reflection of variation in pyrite and organic matter content. The upper Subunit IA is distinctly darker because of higher pyrite and organic matter content and is Pleistocene to late Pliocene in age. Subunit IB is a lighter, upper Pliocene to lower Miocene calcareous pelagic ooze that grades downward into chalk. At Site 960, lithologic Unit I is thinner (100 vs. 185 m thick) and contains many more scoured (erosional) surfaces, especially in the upper subunit, than the same unit at Site 959. In addition, there is considerably more diagenesis in the sediment at Site 960. Glauconitic material fills burrows within the upper 3 m of sediment, and micrite comprises as much as 35% of the sediment at a depth of 16 mbsf.

Subunit IA

Description: Nannofossil/foraminifer ooze and foraminifer/nannofossil ooze with clay
Interval: Sections 159-960A-1R-1, 0 cm, through 3R-1, 95 cm, and 159-960C-1H-1, 0 cm, through 3H-1, 65 cm
Depth: 0–11.6 mbsf, Hole 960A; 0–16.4 mbsf, Hole 960C
Age: Pleistocene to late Pliocene

Table 3. Lithologic units for Site 960.

Unit	Subunit	Cored interval	Depth interval (mbsf)	Thickness (m)	Lithology	Age (Epoch)
I	A	159-960A-1R-1, 0 cm, to 3R-1, 95 cm 159-960C-1H-1, 0 cm, to 3H-1, 65 cm	0–11.6 0–16.4	11.6 16.4	Nannofossil/foraminifer ooze, dark gray (more pyrite)	Pleistocene to late Pliocene
	B	159-960A-3R-1, 95 cm, to 12R-2, 95 cm 159-960C-3H-1, 65 cm, to 13H-1, 55 cm	11.6–100.1 16.4–111.2	98.5 94.8	Nannofossil/foraminifer ooze to chalk, partly glauconitic	late Pliocene to early Miocene
II	A	159-960A-12R-2, 95 cm, to 15R-CC, 25 cm 159-960C-21X-1, 55 cm, to 18X-CC, 42 cm	100.1–136.2 111.2–159.7	36.1 48.5	Glauconite radiolarian nannofossil/micrite chalk and claystone and porcellanite	early Miocene to middle Eocene
	B	159-960A-16R-CC, 0 cm, to 19R-1, 0 cm 159-960C-19X-CC, 0 cm, to 20X-CC, 20 cm	136.2–164.8 159.7–179.0	28.6 19.3	Chert, porcellanite, and claystone	early Eocene
III		159-960A-19R-1, 0 cm, to 20R-1, 115 cm 159-960C-21X-CC, 0 cm, to 23X-1, 53 cm	164.8–175.7 179.0–198.8	10.9 19.8	Palygorskite claystone with barite nodules	early Eocene (base is barren)
IV	A	159-960A-20R-CC, 0 cm, to 21R-1, 115 cm 159-960C-23X-1, 53 cm, to 23X-CC, 19 cm	175.7–185.3 198.8–207.9	9.6 9.1	Glauconite claystone, micrite chalk with foraminifers, phosphate nodules, and fish debris (hardground)	Maastrichtian to Santonian/Coniacian
	B	159-960A-21R-1, 115 cm, to 37R-1, 45 cm 159-960C-24X-1, 0 cm, to 26X-CC, 32 cm	185.3–329.0 207.9–352.8	143.7 144.9	Quartz sand limestone, and skeletal grainstone, and skeletal packstone with mudstone intraclasts	Santonian/Coniacian to Turonian
V	A	159-960A-37R-1, 45 cm, to 53R-CC, 23 cm	329.0–413.1	84.1	Micritic and silty sandstones, sideritic siltstone, sideritic claystone	Unknown
	B	159-960A-54R-1, 0 cm, to 61R-CC, 4 cm (TD)	413.1–451.2	38.1	Silty sandstone, siltstone, and silty claystone	Unknown

Note: TD = total depth

Lithologic Subunit IA comprises interbedded nannofossil foraminifer ooze with clay and foraminifer nannofossil ooze with clay. As at Site 959, increased abundance of foraminifers gives the sediment a lighter color over 10- to 80-cm intervals, with gradational bed boundaries that are usually the result of bioturbation. Bioturbation and lamination are similar to those at Site 959, and, again, disseminated pyrite occurs throughout this subunit. Many more scoured contacts were observed at this site, probably accounting, at least in part, for its decreased thickness. There is usually a millimeter-thick lag of foraminifers above the scoured contact. Green glauconite pellets occur in burrows below 3 mbsf. Several burrows are filled with a mixture of glauconite pellets, pyrite, and foraminifers. No glauconite was observed in coeval sediment at Site 959.

Subunit IB

Description: Clayey nannofossil/foraminifer/micrite ooze to chalk
Interval: Sections 159-960A-3R-1, 95 cm, through 12R-2, 95 cm, and 159-960C-3H-1, 65 cm, through 13H-1, 55 cm
Depth: 11.6–100.1 mbsf, Hole 960A; 16.4–111.2 mbsf, Hole 960C
Age: late Pliocene to early Miocene

The transition from lithologic Subunit IA to lithologic Subunit IB is more gradual at Site 960 than at Site 959, with the color lightening over a 1-m interval and accompanied by a decrease in the pyrite and organic matter content. Considerable dissolution of calcitic shells is indicated by the 35% micrite content in the ooze of Sample 159-960C-3H-1, 69 cm (16.4 mbsf), which is accompanied by traces of dolomite(?) rhombs. Although the rhombs appear to be dolomite in smear slides, XRD analysis of similar rhombs, concentrated in burrows in Samples 159-960A-8R-1, 125–126 cm, and 8R-2, 22–23 cm, indicates siderite (Fig. 11A, B). In addition, the d-spacing of the principal peak is somewhat high (2.82 vs. 2.79 Å in JCPDS Card 29-0696), which suggests that some calcium may be substituting for ferrous iron in this mineral. Glauconite persists as a rare burrow fill and locally colors the sediment green as faint bands and as sharp, thin laminae beginning in the first core of this subunit. Darker beds, with a brownish tinge, occur over 1- to 2-m intervals. These are less than 50 cm thick, and have gradational upper and lower contacts that have been smeared by bioturbation. These beds contain more micrite, plant debris, quartz, mica, and glauconite than the intervening lighter intervals. They also contain a few silicoflagellates and siliceous sponge spicules. The darker beds at Site 959 merely had fewer foraminifers.

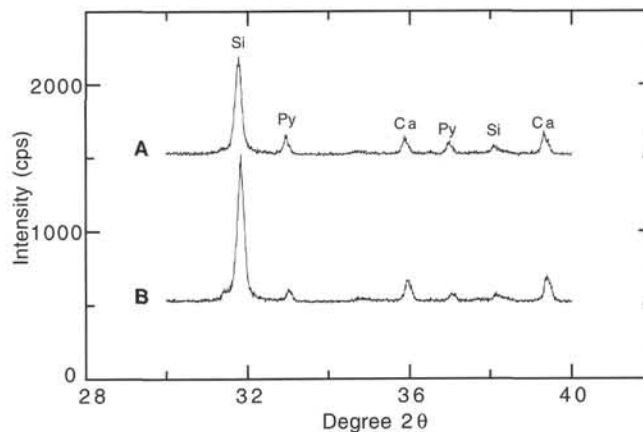


Figure 11. X-ray diffractograms for selected samples from lithologic Subunit IB. **A.** Sample 159-960A-8R-1, 125–126 cm, from the fill of a brown burrow. Peak at 2.82 Å is siderite, probably with some calcium substitution. **B.** Sample 159-960A-8R-2, 22–23 cm, from the fill of a brown burrow: calcium-substituted(?) siderite. Si = siderite; Ca = calcite; Py = pyrite.

The transition from pelagic ooze to chalk at Site 960 is again gradual, but occurs at a shallower level: 49.1 mbsf in Hole 960A and 53.7 mbsf in Hole 960C. The same transition occurs near 75 mbsf at Site 959. Although physical properties do not show a large change at 50 mbsf (see “Physical Properties” section, this chapter), this level may correspond to a diagenetic front as indicated by the pore-water composition (see “Inorganic Geochemistry” section, this chapter). As at Site 959, there is a gradual increase in clay content downcore in this subunit, and this increase is accompanied by a gradual decline in CaCO_3 content (see “Organic Geochemistry” section, this chapter).

Color banding and laminations occur in this subunit as they did at Site 959, with green colors arising from glauconitization of the sediment and from glauconite pellet lags, and light brown colors arising from increased foraminifer levels. A distinctive zone of brown nannofossil chalk with foraminifers, apparently enriched in iron oxide, occurs in Sections 159-960C-10H-4, 0 cm, to 10H-6, 140 cm. In Cores 159-960C-12H and 13H, the darker beds become even darker

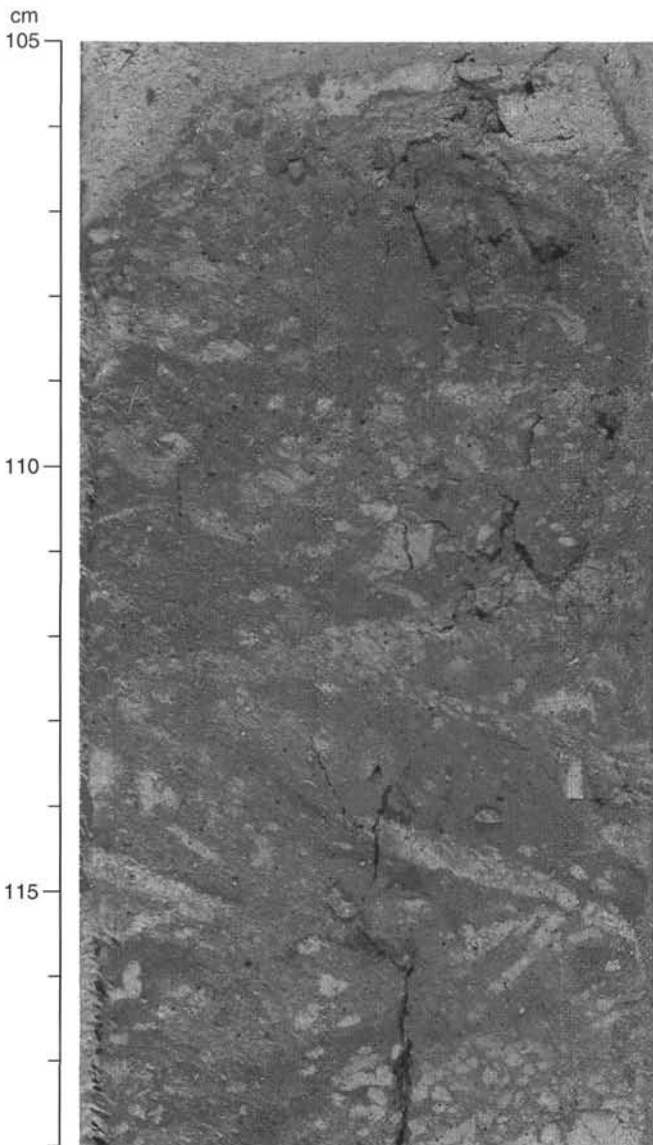


Figure 12. Section 159-960A-10R-5, 105–118 cm. Dark brown beds near the base of lithologic Subunit IB contain more pyrite, clay, zeolite, quartz, and plant debris than the intervening, lighter sediment. *Chondrites* burrows are abundant; *Zoophycos* is faintly visible at 112 cm. Beds with a similar color at Site 959 contain abundant siliceous microfossils and no zeolite.

brown, exhibit more bioturbation than the intervening lighter sediment, and contain higher levels of pyrite, zeolite, clay, quartz, and plant remains (Fig. 12). The principal burrow is *Chondrites*, but *Zoophycos* burrows are also present. Similar beds at the base of lithologic Unit I at Site 959 contain small amounts of siliceous microfossils and no zeolite. Bioturbation in this subunit is only slight to moderate, compared with moderate to heavy at Site 959. Siliceous fossils preserved in these brown beds at Sections 159-960A-12R-2, 95 cm, and 159-960C-13H-2, 118–120 cm, mark the top of the underlying lithologic Unit II. Glauconite pellets gradually increase downcore.

Beginning in Section 159-960C-12H-3, 120 cm, the beds begin to dip markedly away from the horizontal, with the dip increasing downcore. Over the next several cores, the dip increases until the beds become chaotic within lithologic Unit II. Farther downcore, horizontal beds are again present, which suggests that this part of the

core was drilled through a slumped block (see “Structural Geology” section, this chapter).

Unit II

Description: Interbedded nannofossil/micrite chalk, glauconitic claystone with zeolites, chalk with radiolarians, porcellanite, and chert

Interval: Sections 159-960A-12R-2, 95 cm, through 19R-1, 0 cm, and 159-960C-13H-1, 55 cm, through 20X-CC, 20 cm

Depth: 100.1–164.8 mbsf, Hole 960A; 111.2–179.0 mbsf, Hole 960C

Age: early Miocene to early Eocene

Lithologic Unit II was characterized by its significant siliceous component such as radiolarians, opal-CT, and zeolite, in addition to nannofossils and micrite. In this respect, it is similar to lithologic Unit II at Site 959, except that the siliceous fossils are radiolarians rather than diatoms. In addition, this sediment is greatly enriched in glauconite, both as abundant pellets, locally comprising more than 50% of the sediment, and as fully developed hardgrounds. Hardgrounds are weakly developed in sediment of lithologic Unit I at Site 959 and form faint bands or thin wisps. In contrast, in lithologic Unit I at Site 960, the hardgrounds are several centimeters thick. Rip-up clasts from these hardgrounds are sprinkled throughout the unit and are concentrated in zones above the hardgrounds. Although micrite is abundant, and calcite content decreases downcore, nannofossils are sufficiently preserved at this site to provide good age control (see “Biostratigraphy” section, this chapter). Chert occurs principally at the base of this unit, comprising lithologic Subunit IIB, but is early Eocene in age rather than late Oligocene to early Oligocene, as at Site 959. Finally, Subunit IIA was characterized by its chaotic bedding at the macro-, meso-, and microscale. Dipping beds at the top of the unit give way to beds dipping at nearly 90°, which are highly fractured in some places and subjected to plastic flow in others. Beds of different sediment types have flowed together, mixing sediment of biosiliceous, biocalcareous, terrigenous, and diagenetic origin to form every permutation of lithotypes that contain these components: clayey nannofossil chalk with radiolarians, micrite claystone with nannofossils and opal-CT, and zeolitic porcellanite with nannofossils and clay, for example. At Site 959, there is an orderly decrease of recognizable biosiliceous fossils and a concomitant downhole increase in their diagenetic product, opal-CT. This progression is less obvious at this site; opal-CT first appears within 9 m of the top of the unit, and radiolarians comprise 5% of the sediment 20 m above the base. In addition to the chaos imposed by local, syndepositional processes, rotary drilling in Hole 960A further added to the confusion by churning this sediment into biscuits, which, when rotated 180° from one another, gave a zig-zag appearance to the core (Fig. 13). During splitting, glauconite pellets poured out of the burrows and were spread over the core surface, forming a dark green, uniform slurry, which gave the appearance of a 4-m-thick greensand. Only by scraping this material away was some semblance of the real nature of the sediment revealed (Fig. 14). Dipping beds are not evident in the cores from this unit from Hole 960A; this sediment may have been entirely mixed by the rotary drilling process.

Unit II was divided into two subunits: the overlying mixture of sediment types (lithologic Subunit IIA) and the underlying chert (lithologic Subunit IIB). This division is probably spurious, because small chert fragments were recovered in sediments from lithologic Subunit IA, and lithologic Subunit IA lithotypes were recovered clinging to and mixed with chert fragments. The chert probably occurs as several thin, nodular beds, which likely occur where drilling recovery drops precipitously. However, this lower Eocene chert, Horizon A^c (Ewing, Worzel, et al., 1969) from the Atlantic, which is known from the Indian and Pacific Oceans as well, has been the plague of ocean drilling since the first Deep Sea Drilling Project leg, and as such, deserves its own subunit designation.

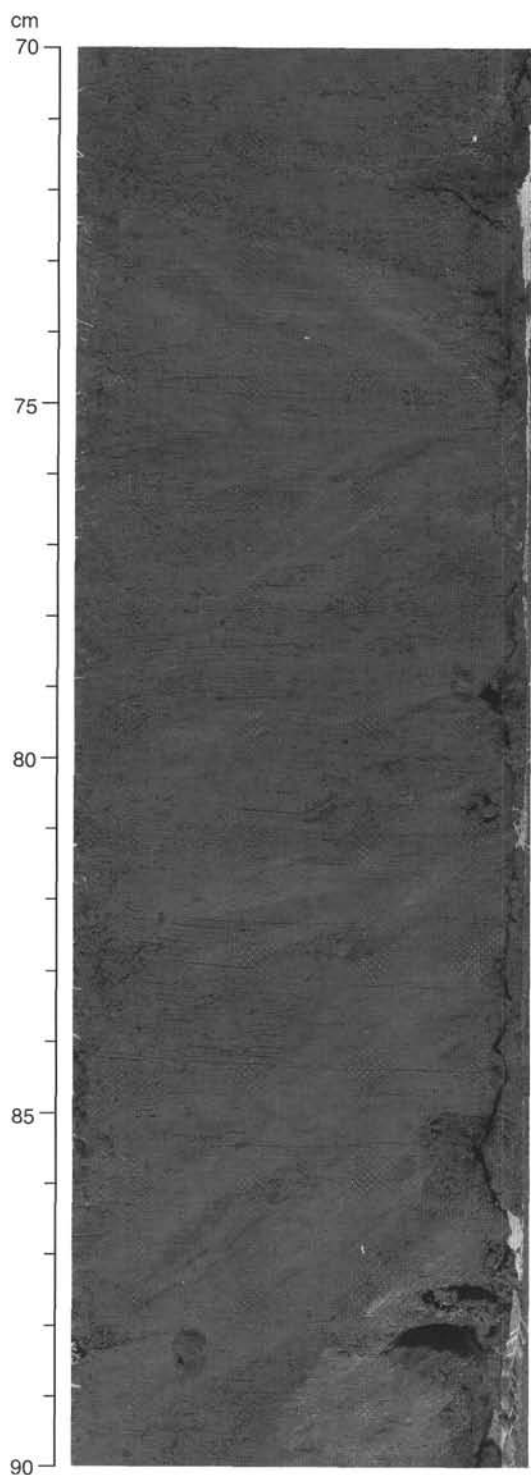


Figure 13. Section 159-960A-12R-6, 70–90 cm, lithologic Subunit IIA, as it initially appeared in the split core from Hole 960A. Dipping beds of clayey porcellanite were turned into drilling biscuits by rotary coring. Independent rotation of the biscuits gives a zig-zag appearance to the coring. This effect was revealed only after scraping away a uniform coating of glauconite pellets, which had extruded out of burrows and covered the core surface during splitting. Dark and light patterns are actually burrows of *Planolites* and *Chondrites*.

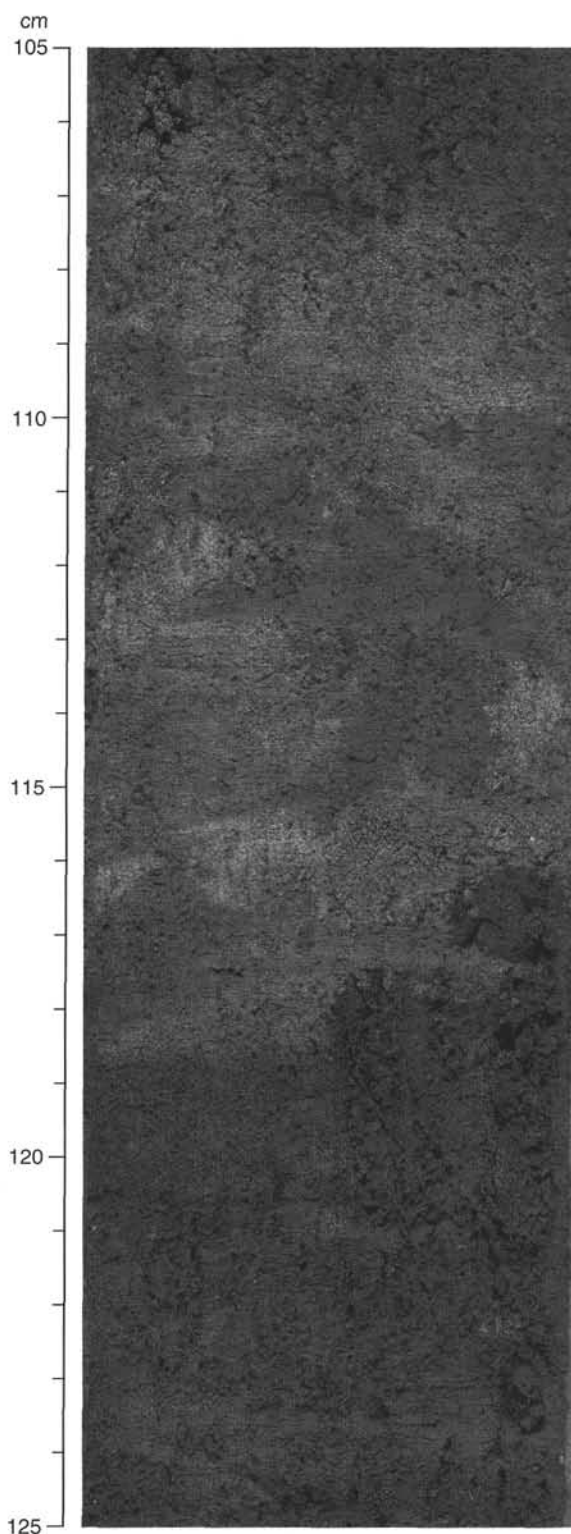


Figure 14. Section 159-960A-12R-3, 105–125 cm. Beds in Subunit IIA in Hole 960A do not appear to be dipping, as they are in Hole 960C. Dense glauconite pellets appear intermixed as well as interbedded with lighter claystone with zeolite. This appearance may be entirely due to the rotary coring technique, as no such alternation was observed in coeval sediment from adjacent Hole 960C, which was XCB cores

Subunit IIA

Description: Interbedded and intermixed, nannofossil chalk, micrite chalk, radiolarians, porcellanite, chert, glauconite, and clay
 Interval: Sections 159-960A-12R-2, 95 cm, through 15R-CC, 25 cm, and 159-960C-13H-1, 55 cm, through 18X-CC 42 cm
 Depth: 100.1–136.2 mbsf, Hole 960A; 111.2–159.7 mbsf, Hole 960C
 Age: early Miocene to middle Eocene

The upper contact of Subunit IIA was designated in Hole 960C at the first bed enriched in siliceous microfossils, a 2-cm-thick bed of clayey nannofossil chalk with radiolarians, and in Hole 960A at a sharp contact between green, glauconitic, weakly calcareous claystone and an underlying glauconitic silty sandstone (Fig. 15). As discussed previously, this subunit in Hole 960A is almost certainly highly disturbed by the rotary drilling technique as well as the core splitting process, and, consequently, this discussion is based on observations made on the sediment from Hole 960C.

The upper 11.3 m of this subunit comprises steeply dipping, alternating beds of light to medium gray nannofossil or micrite chalk and olive brown beds enriched in radiolarians or their diagenetic products, opal-CT and/or zeolite. Nannofossils comprise up to 55% of the sediment, and micrite up to 30%. There is a significant component of clay throughout, from 15% to 50% of the sediment, and of foraminifers (up to 12%). In the darker, olive-colored beds, radiolarians comprise up to 20% of the sediment. Glauconite pellets are a common component, and are especially concentrated in burrows. Glauconitic hardgrounds, up to 7 cm thick, occur at the tops of the lighter or darker beds. Rip-up clasts from these hardgrounds are dispersed throughout the sediment and are especially concentrated just above the hardgrounds. Bioturbation is moderate to heavy, indicating an abundant benthic fauna, including *Zoophycos*, *Planolites*, *Ophiomorpha*, *Chondrites*, and composite burrowers. The darker, biosiliceous beds range from a few centimeters to 30 cm thick, whereas the lighter beds are thicker, from 15 to 50 cm thick. Pyrite is a persistent component throughout, comprising up to 10% of the sediment in the darker intervals.

In Section 159-960C-14H-2, 83 cm (122.5 mbsf), a fault separates the dipping beds from a massive bed of unknown dip. Below this level, beds dip at all angles, separated by faults. The orientation of some beds can be discerned from the abundant *Zoophycos* burrows. Locally, these are so glauconitized that only faint, three-dimensional images of them can be seen. In some places the sediment is clearly fractured; in other places it has clearly deformed plastically to give a folded appearance to *Zoophycos* burrows (Fig. 16; see "Structural Geology" section, this chapter). The sediment composition ranges widely among the principal components: clay; radiolarians or their diagenetic products, opal-CT and zeolite; and nannofossils and foraminifers and their diagenetic product, micrite.

In Section 159-960C-15H-4, 85 cm, the drilling process has further disturbed this already chaotic sediment. Probable flow-in occurs to the base of this core, and recovery drops in the next few cores. A fragment of chert in Section 159-960C-15H-6 reveals a likely suspect for causing the drilling disturbance and poor recovery. Drilling disturbance in the underlying cores is severe, but the composition remains the same as previously, with the exception that radiolarian preservation drops to nil. Fragments of chert occur in Cores 159-960C-16H through 20X.

Subunit IIB

Description: Black chert, porcellanite, and claystone
 Interval: Sections 159-960A-16R-CC, 0 cm, through 19R-1, 0 cm, and 159-960C-19X-CC, 0 cm, through 20X-CC, 20 cm
 Depth: 136.2–164.8 mbsf, Hole 960A; 159.7–179.0 mbsf, Hole 960C
 Age: early Eocene

Lithologic Subunit IIB comprises brownish black, translucent chert, recovered as drilling breccia and mixed with drilling breccia of sediment similar to lithologic Subunit IIA. Most of the chert is mas-

sive, but some of the fragments retain the faint outlines of burrows. Other fragments are laminated, and a few contain ghosts of foraminifers or radiolarians. In Hole 960A the chert is weakly calcareous, and yielded nannofossils that have an early Eocene age. The poor recovery of this interval most likely reflects the alternation of brittle chert layers with a ductile clayey or at least nonlithified lithology. Large intervals were missed by drilling with retrieval of only sporadic cobble-sized fragments of chert. The base of this unit was defined as the first downcore occurrence of a bluish gray palygorskite clay containing barite concretions.

Unit III

Description: Palygorskite claystone with barite nodules
 Interval: Sections 159-960A-19R-1, 0 cm, through 20R-1, 115 cm, and 159-960C-21X-CC, 0 cm, through 23X-1, 53 cm
 Depth: 164.8–175.7 mbsf, Hole 960A; 179.0–198.8 mbsf, Hole 960C
 Age: early Eocene

Lithologic Unit III consists of laminated or structureless claystone with a conspicuous blue to bluish green color (5B 5/1 to 5BG 5/1). Lamination results from an alternation of the blue claystone with brownish gray (5Y 4/1) millimeter-thick layers richer in organic debris. In addition to the presence of quartz, calcite, and siderite (or ankerite), found by XRD analysis of a bulk claystone sample, a clay separate of the blue claystone revealed appreciable amounts of palygorskite and smectite with minor sepiolite and kaolinite (Fig. 17). Intercalated with these claystones are irregular accumulations of single barite crystals, barite siltstones, or subspherical barite nodules that reach 4 cm in diameter, with individual prismatic crystals up to 1 cm in length protruding into the surrounding claystone (Figs. 18, 19). Poor recovery of this interval may be related to the alternation of hard barite layers and soft claystones.

Because of the ease with which the blue claystone can be identified and the poor recovery of the upper contact, the top of lithologic Unit III was placed at the first downcore occurrence of blue claystone with palygorskite. Similarly, the base of lithologic Unit III was placed at the last downcore occurrence of this claystone above the underlying glauconite and biogenic phosphate-bearing lithologies of Subunit IVA.

The age of this unit is early Eocene, derived from an intercalated layer of calcareous porcellanite with calcareous nannofossils in Section 159-960C-22X-CC, 10–13 cm (see "Biostratigraphy" section, this chapter).

Unit IV

Description: Biogenic phosphate and glauconite grainstones, and intraclast/skeletal grainstones and packstones
 Interval: Sections 159-960A-20R-CC, 0 cm, through 37R-1, 45 cm, and 159-960C-23X-1, 53 cm, through 26X-CC, 32 cm
 Depth: 175.7–329.0 mbsf, Hole 960A; 198.8–352.8 mbsf, Hole 960C
 Age: Maastrichtian to Turonian

Lithologic Unit IV consists of two distinct lithologies: lithologic Subunit IVA, a condensed/hial interval comprising biogenic phosphate grainstones containing variable amounts of glauconite, and lithologic Subunit IVB, a carbonate-rich interval consisting of limestone that include quartz sand limestones, skeletal and intraclastic grainstones/packstones, and bioclastic claystones. These two subunits were combined into one lithologic unit because the Upper Cretaceous age subunit appears to be a series of hardgrounds and condensed intervals more associated with the underlying Cretaceous calcareous sediment than with the overlying Tertiary-age palygorskite-rich claystone. The top of this unit was defined as the last occurrence of blue-green, palygorskite claystone with barite and the first occurrence of biogenic phosphate and glauconite. The base is marked by

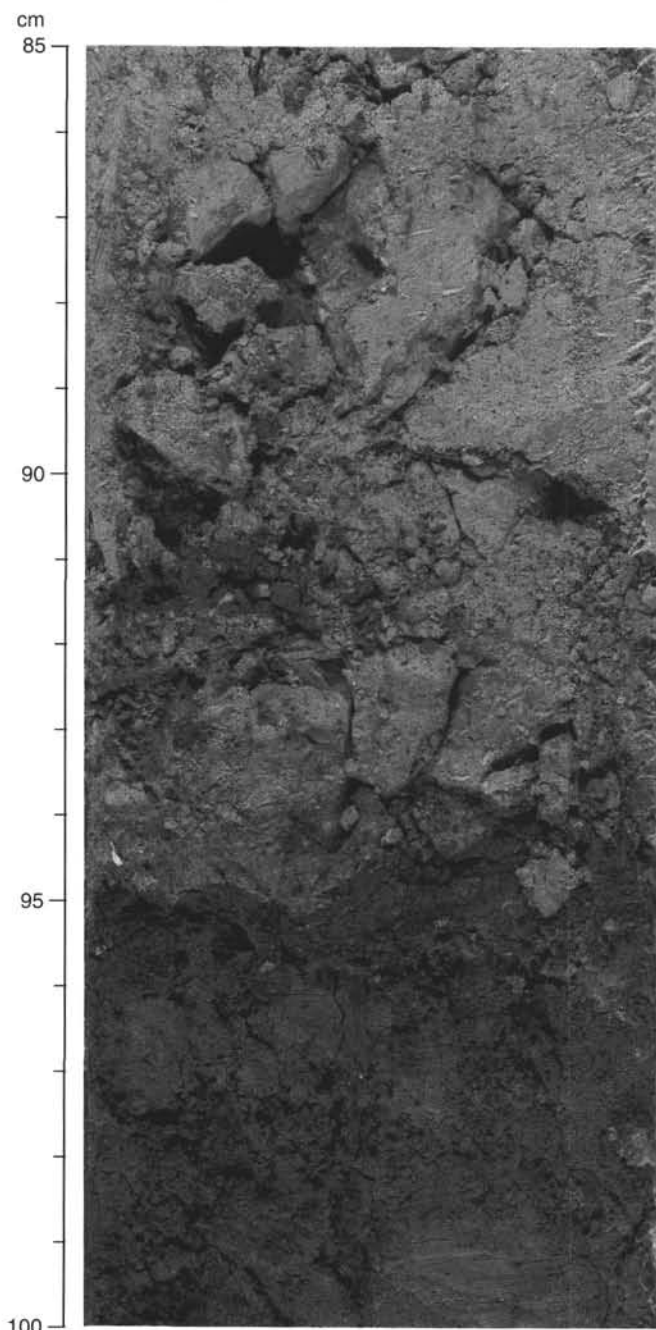


Figure 15. Section 159-960A-12R-2, 85–100 cm, contact between nannofossil claystone of lithologic Subunit IB and glauconitic claystone and silty sandstone of lithologic Subunit IIA in Hole 960A. This sharp contact was not observed in the better-recovered section from Hole 960C.

an inferred unconformity between calcite-cemented sandstones and siltstones of lithologic Unit V and the overlying bioclastic and intraclastic limestones of lithologic Subunit IVB (Fig. 20).

Subunit IVA

Description: Micrite claystones and chalk with biogenic phosphate, glauconite, and foraminifers Interval: Sections 159-960A-20R-CC, 0 cm, through 21R-1, 115 cm, and 159-960C-23X-1, 53 cm, through 23X-CC, 19 cm

Depth: Hole 960A, 175.7–185.3 mbsf; Hole 960C, 198.8–207.9 mbsf

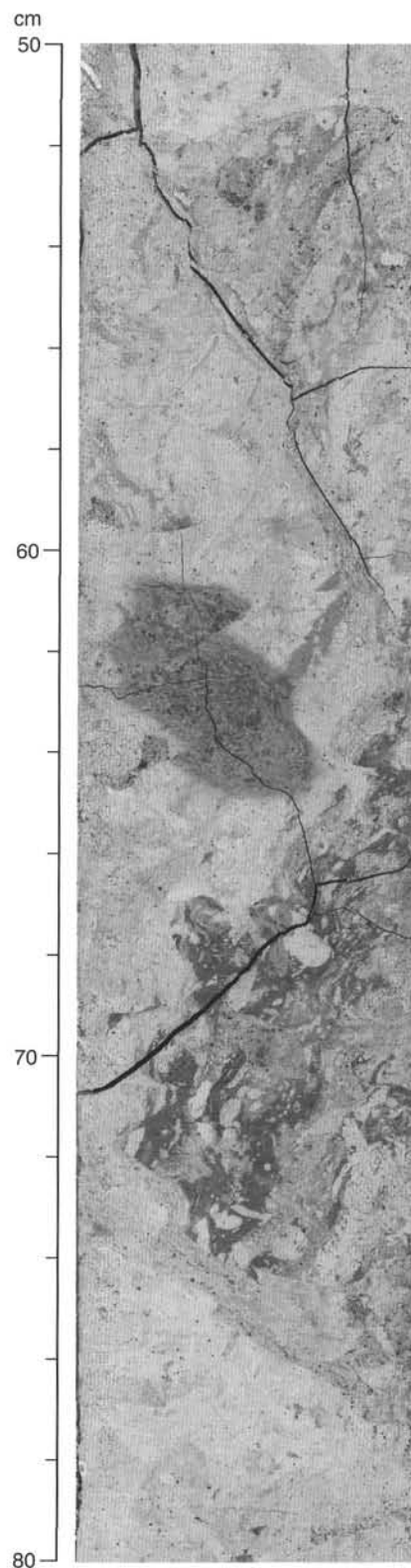


Figure 16. Section 159-960C-14H-5, 50–80 cm, the chaotic part of lithologic Subunit IIA. A burrow at 60–65 cm has been fractured, whereas olive sediment from 66 to 74 cm has deformed plastically, giving a zig-zag appearance to the sediment.

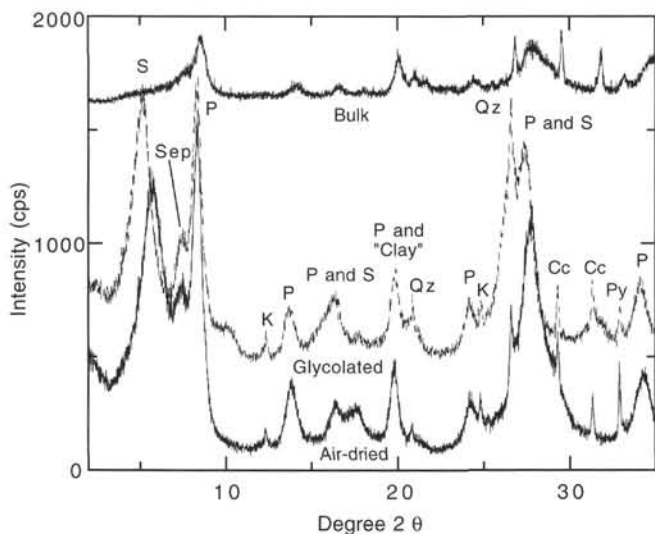


Figure 17. X-ray diffractogram from clay separates of the bluish claystone of lithologic Unit III from Sample 159-960A-20R-1. 92–94 cm. S = smectite, P = palygorskite, Sep = sepiolite, K = kaolinite, Qz = quartz, Cc = calcite. Note that the trace of glycolated mount is offset by 400 cps relative to the air-dried mount. Intensity for bulk sample is not to scale.

Age: Maastrichtian to Santonian/Coniacian

The upper boundary of Subunit IVA is the last downcore occurrence of blue palygorskite claystone and the first downcore appearance of phosphatic biogenic debris and glauconite. This interval is distinctive both in its greenish gray (5GY 5/1) color, which is imparted by the presence of disseminated glauconite, and by the brownish gray (5Y 5/1 to 5Y 7/1) massive grainstones composed of biogenic phosphate (Sections 159-960A-20R-1, 0–5 cm, 20R-CC, 0–12 cm, and 21R-1, 0–20 cm). These phosphate-bearing beds are intercalated with glauconitic claystones throughout this interval. Although the green claystones are relatively free of phosphatic debris, the grainstones contain a large proportion of quartz, glauconite pellets, and phosphatic fish teeth and scales (Fig. 21).

The age of lithologic Subunit IVA is problematic. A sample from the grainstone in Section 159-960A-20R-CC, 0–12 cm, gave a late Coniacian to early Santonian age based on calcareous nannofossils. An early Eocene calcareous nannofossil age and a Maastrichtian planktonic foraminifer age were determined for the bottom of the core catcher (see “Biostratigraphy” section, this chapter).

The lower contact of Subunit IVA is stratigraphically sharp. At this contact, the underlying limestone is brecciated, and fragments are supported within a calcite-cemented, quartz sand and glauconite-rich matrix.

Subunit IVB

Description: Quartz sand limestones, skeletal and intraclastic packstones and grainstones, and micrite chalk with quartz silt

Interval: Sections 159-960A-21R-1, 115 cm, through 37R-1, 45 cm, and 159-960C-24X-1, 0 cm, through 26X-CC, 32 cm

Depth: 185.3–329.0 mbsf, Hole 960A; 207.9–352.8 mbsf, Hole 960C
Age: Coniacian to Turonian

Lithologic Subunit IVB comprises dominantly quartz sand and bioclast grainstones, quartz sand floatstone (coarse intraclasts floating in a finer grained matrix), and pure limestones including skeletal grainstones and packstones. The upper contact of this unit (Section 159-960A-21R-1, 115 cm) is defined as the last occurrence of glauconite and the first occurrence of bioclastic limestones (Fig. 22). Although obscured by drilling disturbance, the lower boundary of litho-

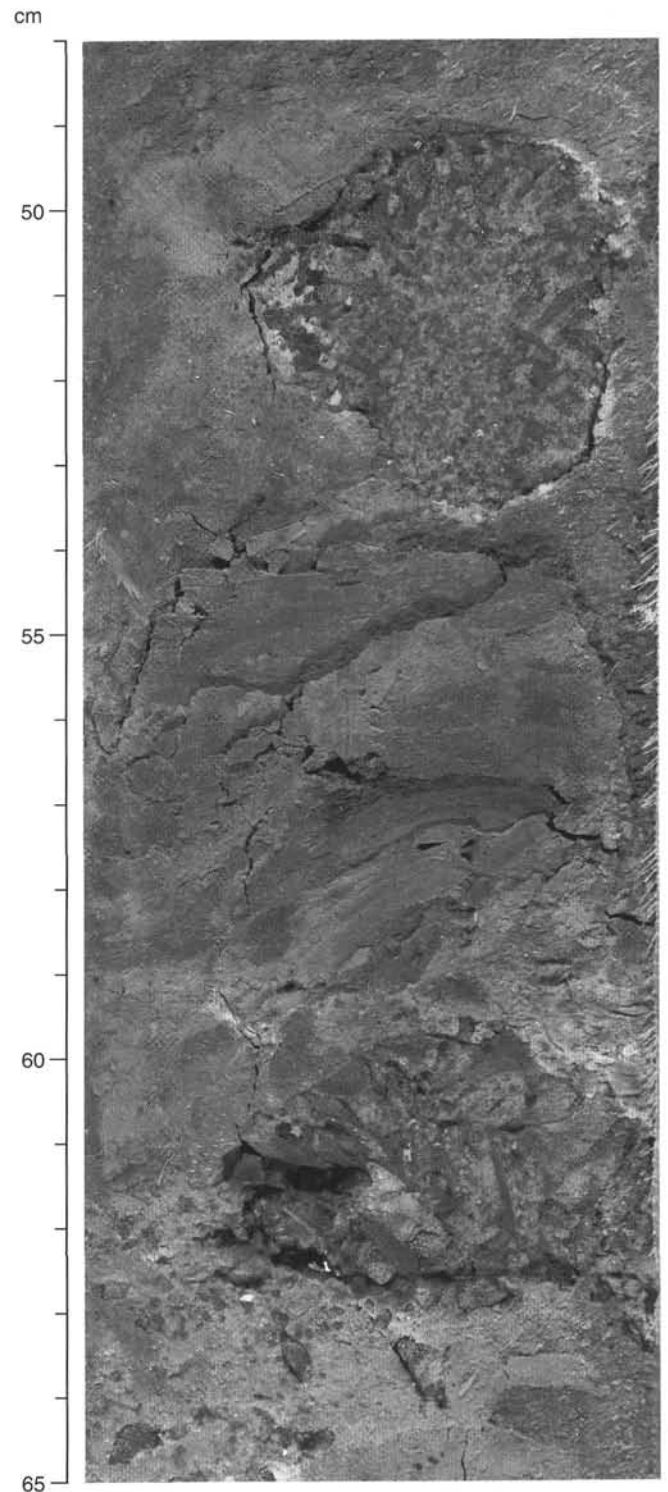


Figure 18. Section 159-960A-19R-1, 48–65 cm, coarse crystalline barite nodule and irregular accumulation of barite crystals within blue palygorskite claystone.

logic Unit IV is inferred to be unconformable, reflecting an erosional contact with the underlying siltstones and sandstones of lithologic Unit V, which lack bioclasts. Lithoclasts of quartz sandstone and siltstone from Unit V are incorporated in limestones of basal lithologic Subunit IVB.

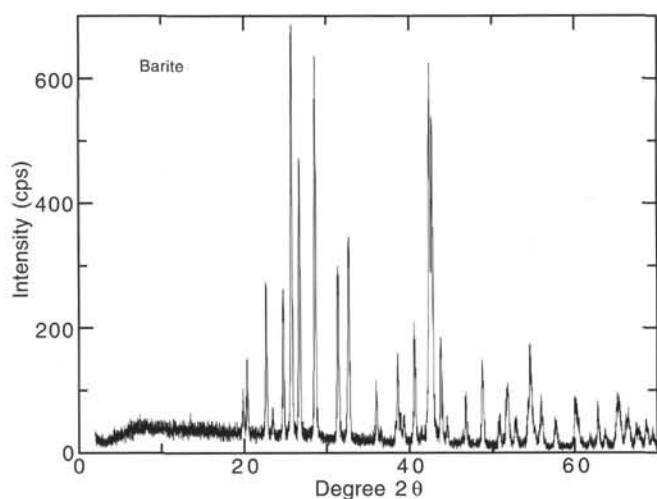


Figure 19. X-ray diffractogram from a barite nodule of lithologic Unit III only shows barite peaks. Sample 159-960A-19R-CC, 23–24 cm.

Lithologic Subunit IVB is variable in its abundance of siliciclastic components estimated from thin sections and smear slides. The lithology of the upper and lowermost parts of lithologic Subunit IVB contains abundant angular to subangular quartz and feldspar (10% to 40%), intermixed with carbonate bioclasts and allochems (Fig. 23). In contrast, the middle of this subunit (Sections 159-960A-31R-1, 0 cm, through 37R-1, 50 cm; 271.1–329.0 mbsf) is characterized by nearly pure bioclastic limestones largely devoid of detrital siliciclastic grains (less than 5% quartz). Skeletal components include molluscan fragments (bivalves and gastropods), echinoderm debris, red and green algae (both as fragments and boundstones), bryozoa(?), and foraminifers. Changes in the abundance of siliciclastic components are gradual, both into and out of the interval of nearly pure limestones. For example, the lower part of Subunit IVB above the unconformity with Unit V was cored in Hole 960C using XCB methods (Cores 159-960C-24X, 25X, and 26X). Interbedded bioclastic limestones and silty/sandy micrite chalks recovered at the base of this unit show a gradual upward decrease in the abundance of quartz silt and sand into relatively pure limestones.

The quartz sand-rich lithology of the upper part of lithologic Subunit IVB consists of light gray (5GY 6/1 to 7/1), medium- to coarse-grained, bioclastic grainstones alternating with gray (5Y 8/1 to N6) quartz sand grainstone and darker gray (N5 to N6) floatstone. Poorly sorted floatstone includes large quartz sandstone clasts, up to 3 cm in diameter, and bioclasts comprising up to 40% of the total components embedded in a carbonate-cemented, quartz sand-rich matrix. Framework grains include shell fragments, limestone intraclasts, and angular quartz. In Core 159-960A-22R, the 30–40 cm thick floatstone beds fine upward to bioclastic grainstones dominated by molluscan fragments. The interval from 232.4 to 271.1 mbsf consists largely of structureless, moderately to poorly sorted, medium gray (N5 to N6) quartz sand grainstone. Carbonate grains comprise benthic foraminifers, echinoderm debris, gastropods, and bivalve shell fragments up to 2 cm in diameter. Calcareous red and green algae are also abundant, occurring as bioclasts and fragments. Red algae, and what are interpreted to be bryozoa, develop small boundstone encrustations although none of these are in-place reefal boundstones. Rather, we interpret this lithology to represent allochthonous deposits into deeper water settings where quartz sand (up to 30%) can be intermixed. The quartz sand grainstones present in this interval are typically cemented by micritic calcite, but sparry calcite cement fills late fractures and remaining intergranular porosity.

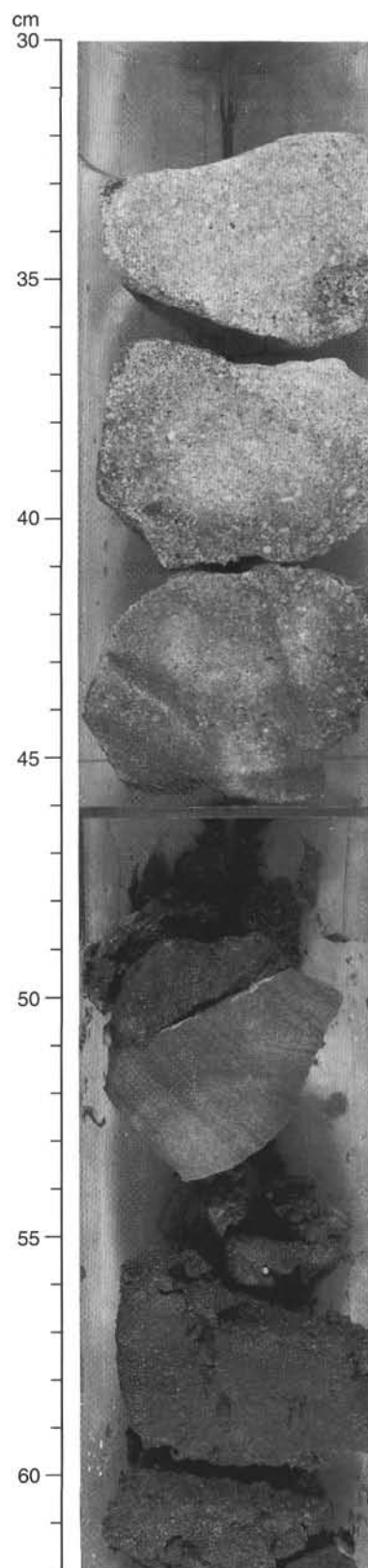


Figure 20. Section 159-960A-37R-1, 30–62 cm. The contact between skeletal grainstone and packstone of lithologic Unit IV and micritic sandstone of Lithologic Unit V is interpreted as an unconformity. Drilling breccia occurs just below the boundary at 45 cm, but the first coherent sandstone bed is steeply dipping.

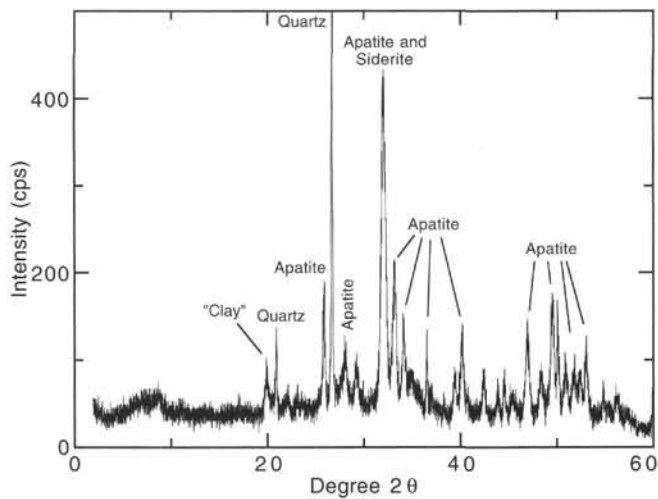


Figure 21. X-ray diffractogram from the brownish gray calcareous sandstone with fish debris of lithologic Unit III shows strong quartz peaks (4.24 Å; 3.34 Å) and several apatite peaks in Sample 159-960A-21R-1, 8–10 cm. The presence of clay is indicated by a peak at 20° 2θ and a broad hump between 6° and 10° 2θ.

Limestones, skeletal grainstones and packstones, contain less than 5% siliciclastics and are light to medium gray (5Y 8/1 to 5GY 5/1). In Core 159-960A-31R, poorly sorted grainstones grade upward into fine-grained packstones, or as in Core 159-960C-23X, these lithologies are interbedded. Vuggy porosity, developed where aragonitic molluscan debris has been dissolved, is locally filled by equant calcite cement (Fig. 24). The degree of cementation increases downcore, resulting in well-cemented, less porous limestone.

Sections 159-960A-32R-1, 40–41 and 120 cm, and 159-960A-32R-2, 1–8 cm, contain abundant lithoclasts of sandstone and siltstone 1 mm to 1 cm in size. Micritized ooids, occurring in Section 159-960A-33R-1, 80–100 cm, are intermixed with peloidal, intraclastic, and skeletal grains. These indicate a very shallow water depth for the source area of these carbonates. Moreover, the presence of quartz sand as nuclei of some ooids suggests an environment where terrigenous siliciclastic and carbonate sediments are coeval and not merely intermixed during deposition. In contrast, the angular to sub-angular grain shape of these quartz grains requires close proximity of their source to the depositional basin.

The lower quartz sand-rich interval, recovered from Cores 159-960C-25X and 26X, provides further constraints on the nature of the depositional system. For example, medium- to very coarse-grained, poorly sorted, skeletal grainstones, containing granule-sized clasts of dark brown claystone, are interbedded with skeletal packstones containing planktonic foraminifers (Fig. 25) and with finely laminated, dark brown (5Y 2.5/1) micrite claystones (similar to the claystone intraclasts mentioned previously). The lack of a fine-grained matrix in the limestones suggests a grain-flow depositional origin with periods of intervening quiescence recorded by pelagic and hemipelagic sedimentation.

Unit V

Description: Claystone, silty claystone, siltstone, silty sandstone and sandstone

Interval: Sections 159-960A-37R-1, 45 cm, through 61R-CC, 4 cm (TD)

Depth: 329.0–451.2 mbsf

Age: Unknown

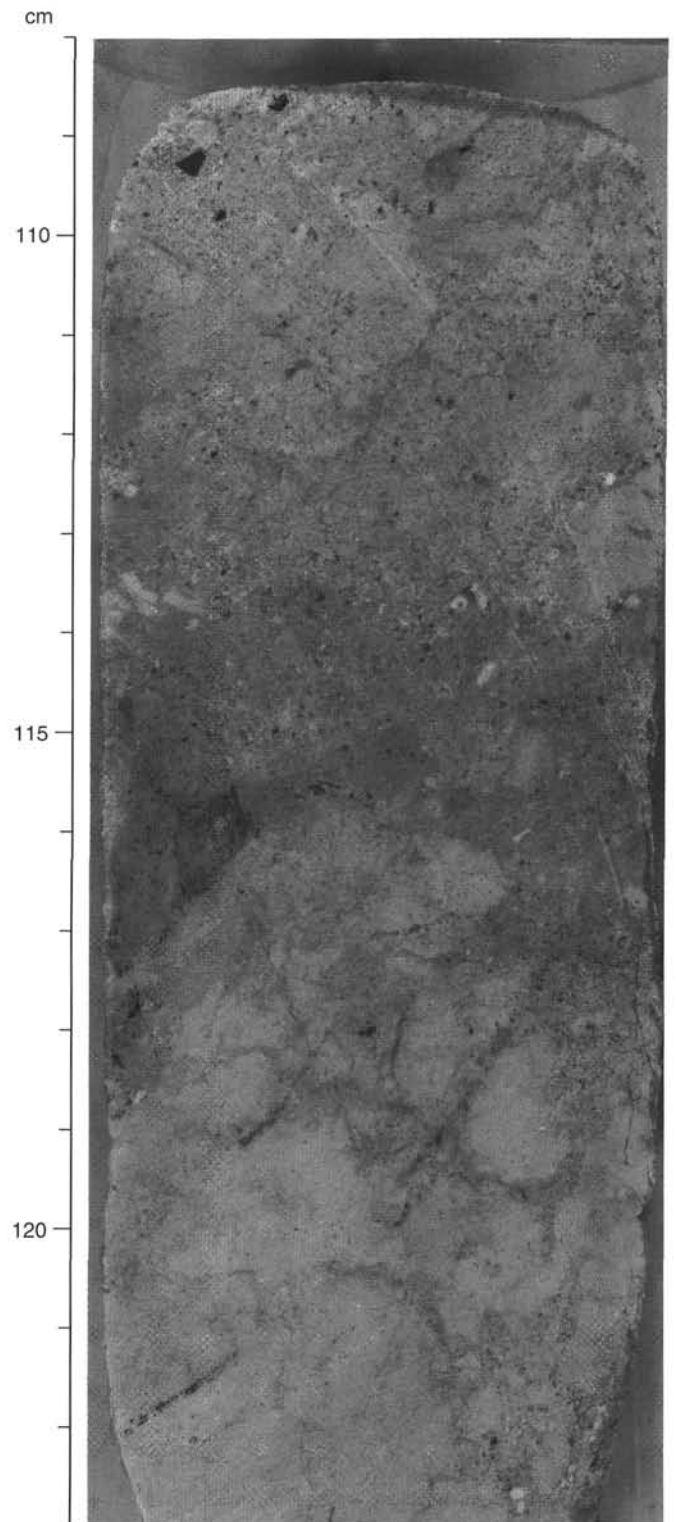


Figure 22. Section 159-960A-21R-1, 108–123 cm, dolomitic limestone breccia with a calcareous clay-rich matrix forming the upper boundary of lithologic Unit IV.

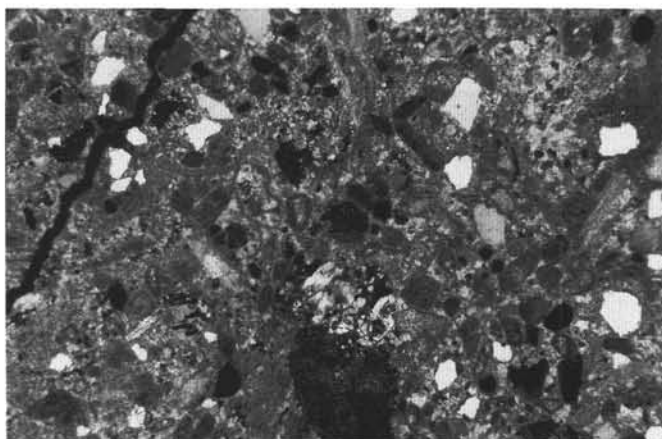


Figure 23. Photomicrograph of the quartz sand floatstone of the upper part of lithologic Subunit IVB showing abundant angular to subangular quartz and feldspar intermixed with carbonate bioclasts and allochems (Sample 159-960A-22R-2, 25–30 cm).

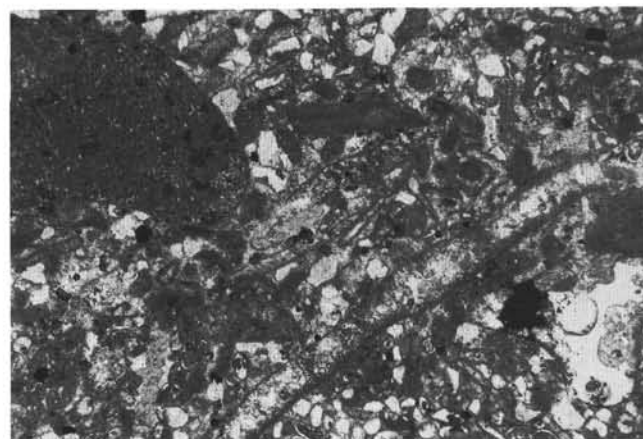


Figure 24. Photomicrograph of vuggy porosity developed where aragonitic molluscan debris has been removed by dissolution. Note that intergranular and dissolution porosity is now filled by equant calcite cement (Sample 159-960A-22R-1, 20 cm).

Lithologic Unit V comprises dominantly silty sandstone, micritic sandstone, massive claystone, and parallel laminated silty claystone. The age of the unit has not been determined because it is barren of microfossils. The upper boundary of this unit was defined by the first occurrence of steeply dipping micritic sandstone beneath the succession of lithologic Unit IV, that comprises skeletal grainstone and packstone with mudstone intraclasts (Fig. 25). This boundary is inferred to be an unconformity based on the abrupt change in lithofacies between quartz sandstones and the overlying succession of pelagic and hemipelagic limestones and claystones, and the inclusion of lithoclasts in the limestones derived from erosion of the underlying sandstones and claystones.

The sediments in this unit are divided into two subunits. Lithologic Subunit VA comprises fine- to medium-grained, cross-bedded to parallel laminated, micritic sandstone and massive black claystone associated with siderite, marcasite, and pyrite. The subunit grades downward into massive to faintly cleaved, black claystone. Lithologic Subunit VB consists of finely laminated black to gray silty claystone and silty sandstone, with some intercalations of siltstone beds.

Lithologic Unit V has been tectonically deformed (see “Structural Geology” section, this chapter), and several intervals have faults, breccias, sedimentary dikes, and mineral-filled veins, fractures, and tensional gashes (Fig. 26). Generally, steeply dipping beds occur underneath the unconformity and in some intervals down to Core 159-960A-54R.

Subunit VA

Description: Sandstone and claystone

Interval: Sections 159-960A-37R-1, 45 cm, through 53R-CC, 23 cm

Depth: 329.0–413.1 mbsf

Age: Unknown

Lithologic Subunit VA contains 84.1 m of claystone and sandstone of unknown age. Drilling disturbance is pronounced throughout this subunit. The top 9.7 m (Sections 159-960A-37R-1, 45 cm, to 38R-1, 50 cm) of the subunit begins with micritic sandstone, with varying amounts of mudstone and siltstone intraclasts. The sandstone varies downward in Core 159-960A-37R from a cross-bedded to laminated, dark gray (10Y 4/1), fine- to medium-grained sandstone into a sandstone that is structureless to crudely bedded and medium to coarse grained. Water escape structures and clastic dikes are present in the upper part of this unit (see “Structural Geology” section, this chapter, Fig. 44). Veins infilled with authigenic clays, calcite, and py-

rite occur sporadically (Fig. 26). A thin, conglomerate bed with intraclasts, exhibiting size grading, is also present at the top of this subunit, which has been overturned by syndepositional slumping. Section 159-960A-38R-1, 0–50 cm consists of a moderately fractured, structureless, very fine- to fine-grained sandstone. Some of the fractures are filled with pyrite.

The interval from 338.7 to 362.3 mbsf (Sections 159-960A-38R-1, 50 cm, through 43R-CC) comprises massive, black (N2 to 5GY 2/1) claystone, most of which is churned into drilling breccia. Pyrite, siderite, and marcasite are disseminated throughout the claystone, whereas calcite concretions are locally present. Large pyrite nodules, 1.5 cm across, occur in Core 159-960A-38R. Thin veins infilled by authigenic books of kaolinite and pyrite are present throughout much of this interval. The claystone varies from massive to slightly fissile at some intervals. Several slickensided fault planes are present in the lower part of the interval, in Sections 159-960A-42R-1 through 43R-1, 50 cm.

The claystone between 362.3 and 370.7 mbsf (Sections 159-960A-44R-1 through 45R-3, 47 cm) is grayish black to medium gray (N2 to N5) and structureless to finely laminated. Carbonate cements (siderite and calcite) are common with sideritic claystone at some intervals. The claystone also grades into sideritic siltstone and claystone with quartz silt and siderite, in Cores 159-960A-44R and 45R. Whereas the claystone is only slightly bioturbated, the siltstone is heavily bioturbated. Burrows are indistinct and less than 5 mm in diameter. Parallel and cross-laminations are visible in less bioturbated intervals of the siltstone. Very light gray to white (N8 to N9) kaolinite intermixed with siderite fills veins and tension gashes throughout the claystone.

Sections 159-960A-45R-3, 47 cm, through 48R-CC, 26 cm (370.7–384.9 mbsf), consist of silty sandstone, clayey siltstone, and silty claystone. The silty sandstone is gray (N5 to N6), moderately sorted, structureless to plane parallel laminated, with thin intervals containing wavy and convolute laminae and flaser bedding. Sections 159-960A-45R-CC and 46R-4, 62–76 cm, consist of sedimentary breccia, containing clasts of laminated, rippled, and massive silty sandstone (Fig. 27). The sandstone grades downcore into grayish black (N2.5) clayey siltstone and silty claystone, but there is a thin bed of sandstone in Section 159-960A-48R-CC. The clayey siltstone shows some lenticular bedding, whereas the claystone is structureless.

Grayish black to dark gray (N2 to N3) claystone occurs between 384.9 and 413.1 mbsf (Sections 159-960A-48R-CC, 26 cm, through 53R-CC, 23 cm). This lithology contains no primary sedimentary

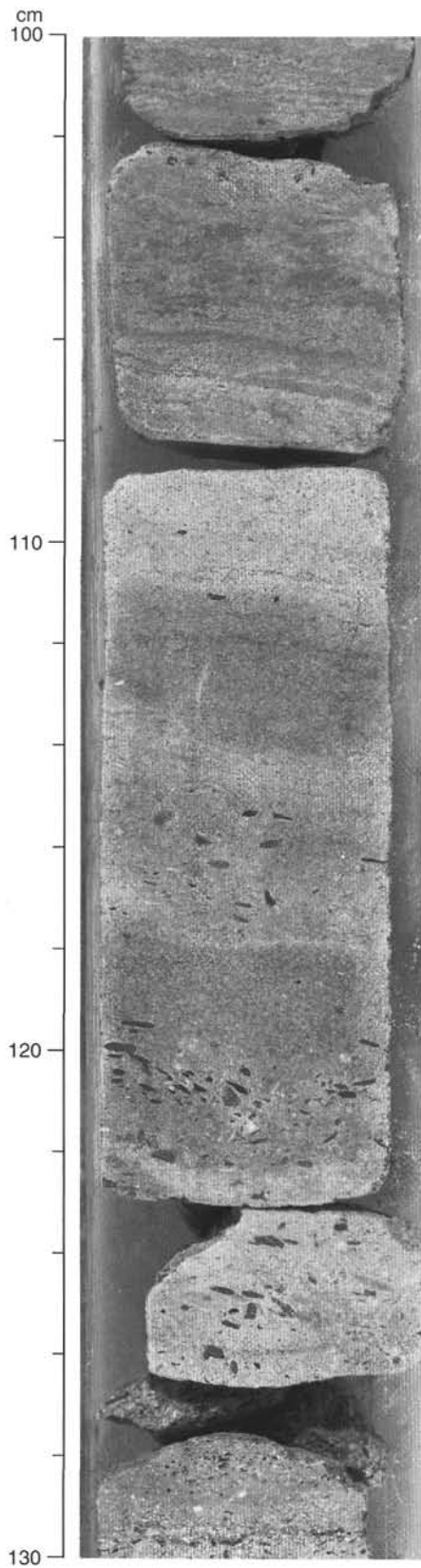


Figure 25. Section 159-960C-25X-1, 100–130 cm. Medium- to very coarse-grained, poorly sorted skeletal grainstone with granule-sized clasts of dark brown claystone is interbedded with skeletal packstones containing planktonic foraminifers.

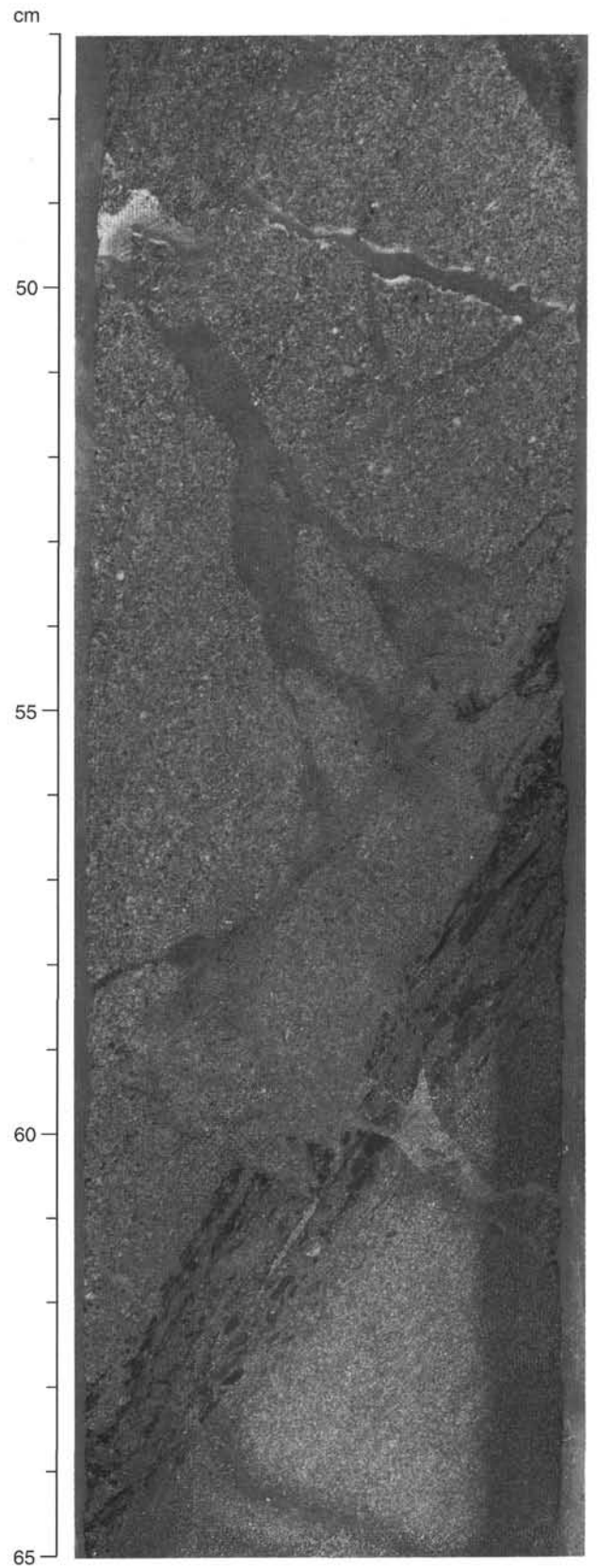


Figure 26. Section 159-960A-37R-2, 47–65 cm. Water escape structures, clastic dikes, and veins in the micritic sandstone of lithologic Subunit VA. These structures are filled with clayey material, calcite, and pyrite.

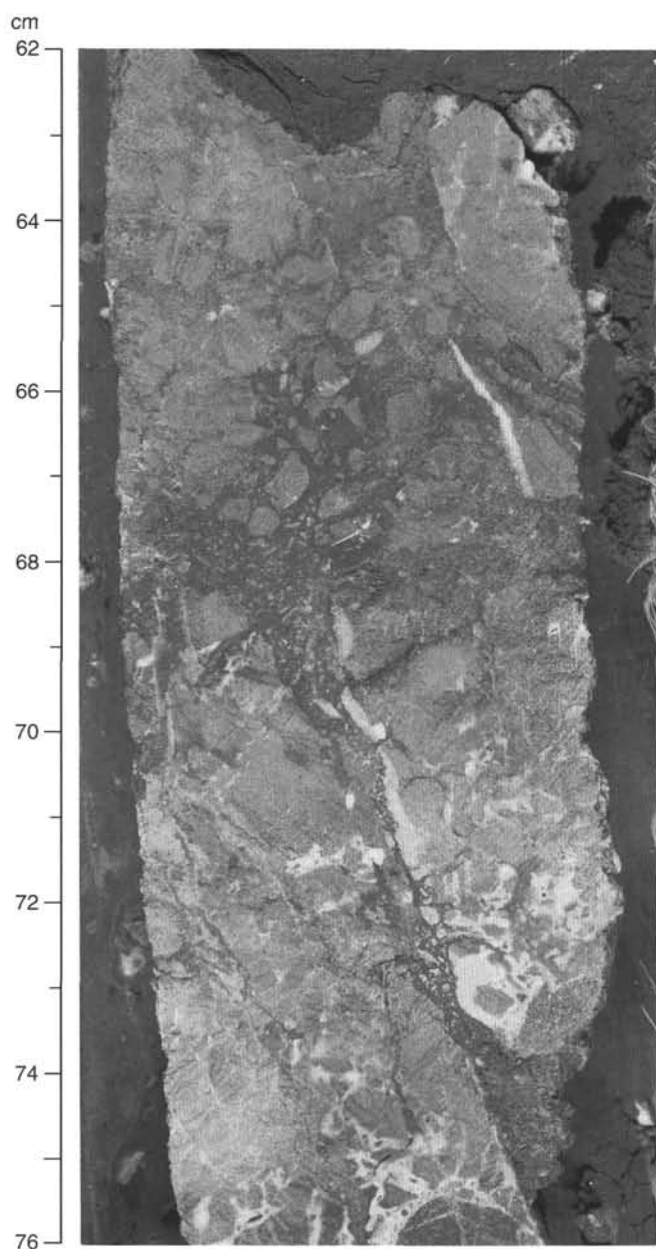


Figure 27. Section 159-960A-46R-4, 62–76 cm, sedimentary breccia comprising clasts of laminated, rippled, and massive silty sandstone in a clayey siltstone matrix of lithologic Subunit VA.

structures, and contains veins and fractures filled by kaolinite and carbonate (siderite and calcite). The top of this interval is moderately bioturbated, whereas parallel fracture cleavage is faintly visible at several horizons.

Subunit VB

Description: Silty sandstone, siltstone, and silty claystone
 Interval: Sections 159-960A-54R-1, 0 cm, through 61R-CC, 4 cm (TD)
 Depth: 413.1–451.2 mbsf
 Age: Unknown

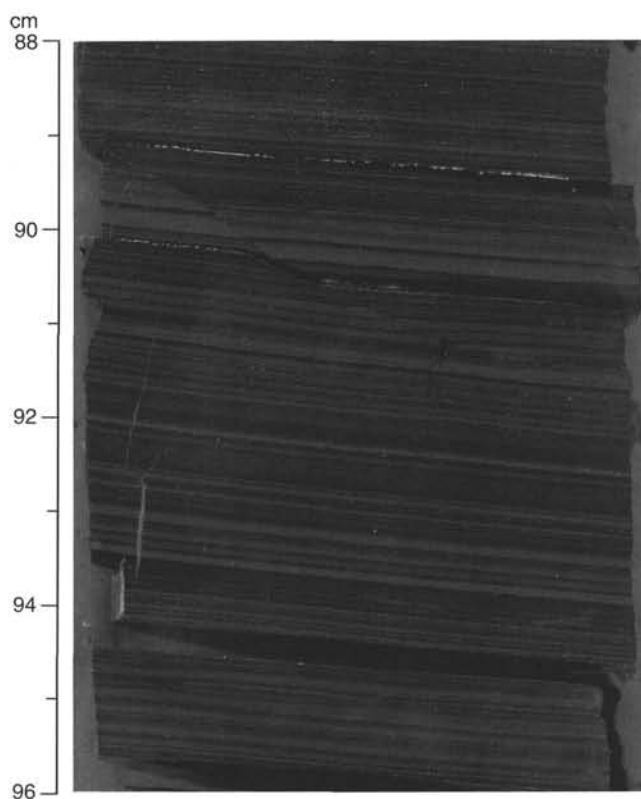


Figure 28. Section 159-960A-54R-2, 88–96 cm, prominent parallel lamination in silty claystone of lithologic Subunit VB. Darker colored laminae are richer in plant debris and carbonaceous material, whereas lighter laminae are richer in quartz and clay minerals.

Lithologic Subunit VB comprises a succession of laminated, dark gray to medium gray (N3 to N4) silty sandstone, grayish black to gray (N2 to N6) sandy siltstone, dark gray (N3) clayey siltstone, and black to grayish black (5G 2/1 to N2) silty claystone of unknown age. The principal differences between this subunit and Subunit VA are the absence of pyrite, near-absence of bioturbation (except in Section 159-960A-56R-1, 18–40 cm), and millimeter-scale parallel laminations (Fig. 28) in lithologic Subunit VB. Drilling disturbance is also less pronounced.

Parallel laminations are much more prominent in the silty claystone than in the other lithologies, in particular from Cores 159-960A-54R through 58R, where typical, alternating lighter and darker laminae are 0.5 to 2 mm thick and continuous across the core. The darker laminae are 0.5 to 2 mm thick and continuous across the core. The darker laminae are richer in plant fragments and carbonaceous material, whereas the lighter laminae are more quartz-rich. In the lower part of lithologic Subunit VB (Cores 159-960A-57R through 61R), silty sandstone and sandy siltstone occasionally have some fining-upward intervals. The thickest is 20 cm, but most are 2 to 4 cm thick, with sharp, scoured lower contacts, or lower contacts having 3- to 6-mm-size load structures (Fig. 29). Above the contact, massive sediment is overlain by faintly planar laminae, which are in turn overlain by rippled laminae. Water escape structures occur in a few intervals. Some beds are steeply dipping, although some layers have been deformed as a result of extensional, and to some extent compressional, tectonism (see “Structural Geology” section, this chapter; Fig. 42). Mineral-filled veins and fractures are common. Mica flakes are

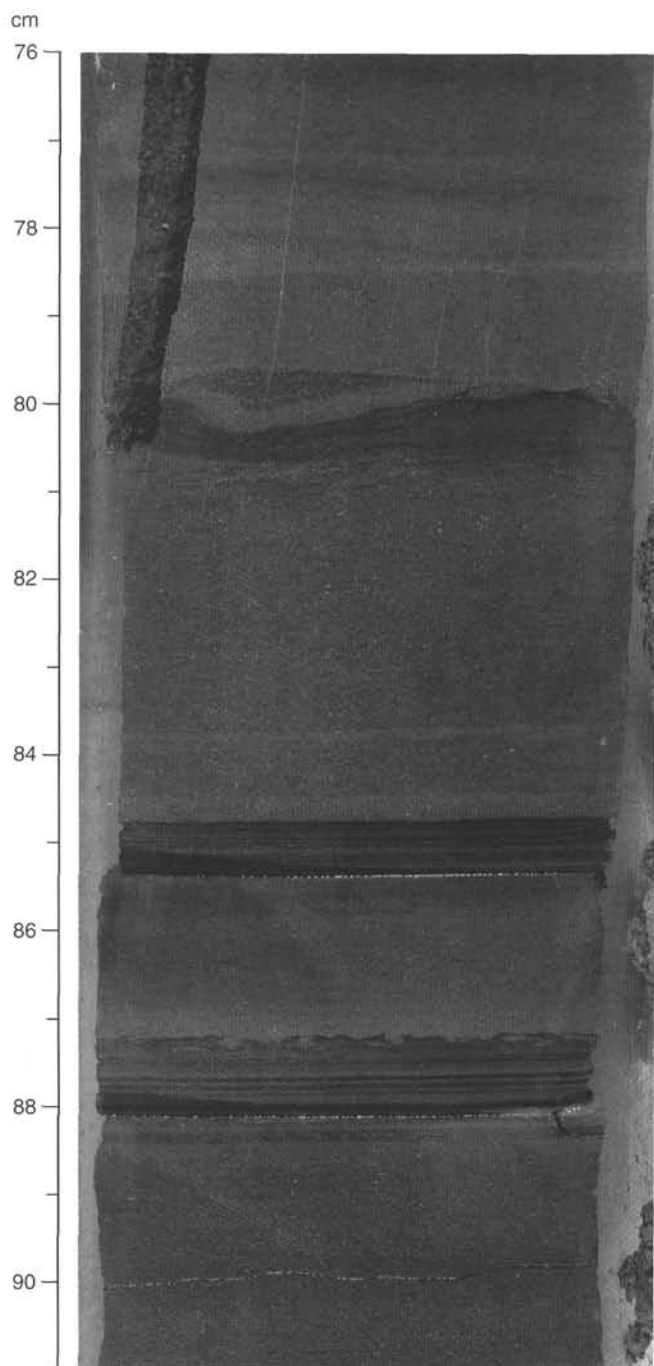


Figure 29. Section 159-960A-57R-1, 76–91 cm, fining-upward beds with sharp scoured lower contacts, load casts, and ball-and-pillow structures in lithologic Subunit VB. Parallel-laminated silty claystone beds are interbedded with fining-upward silty sandstone beds.

present in all the lithotypes, and the silty sandstone contains micritic carbonate cement in Core 159-960A-59R.

Discussion

The succession of lithofacies at Site 960 provides insight into the evolution of the depositional environments for this region (also see Fig. 4 of “Principal Results” chapter, this volume).

Four related sequences can be identified:

1. A “synrift” stage, comprising nonmarine to brackish/marine siliciclastic sediments (Unit V);
2. A marginal marine, shallow shelf-to-basin stage comprising shallow-shelf clastics and carbonates and deep-shelf gravity-flow deposits (lithologic Subunit IVB deposited unconformably above lithologic Unit V);
3. A stage of Marginal Ridge submergence comprising a glauconite- and phosphate-rich condensed interval (lithologic Subunit IVA), which reflects isolation from sources of terrigenous clastics. This in turn grades upward into palygorskite and barite claystone (lithologic Unit III); and, finally,
4. A subsiding passive margin stage comprising chert (lithologic Subunit IIB), glauconite radiolarian nannofossil chalk (lithologic Subunit IIA), and nannofossil chalk and ooze (lithologic Unit I).

Synrift—Lacustrine to Shallow Marine

The lower part of lithologic Subunit VB (Sections 159-960A-54R-1, 0 cm, through 61R-CC, TD) consists of sediments that exhibit alternations of laterally continuous, 0.5- to 2-mm-thick, darker and lighter laminae (Figs. 28, 29). The darker layers are much richer in plant debris and carbonaceous material (up to 10% of total sediment by visual estimate), whereas the lighter laminae are dominantly quartz- and clay-mineral-rich. These characteristics are consistent with varves or rhythmites formed in a freshwater lake environment (Reineck and Singh, 1980) and similar to features observed at DSDP Site 380 in the Black Sea (Shipboard Scientific Party, 1978). They are different from shallow marine varves, which characteristically have tidal bedding and are discontinuous, and from those formed in low-energy estuarine and coastal bay environments, which contain rhombs of biogenic carbonate and diatom-rich layers (Reineck and Singh, 1980). Primary evidence for lake deposition is the rarity of bioturbation, the absence of pyrite, and the abundance of siderite in the sediments. A synrift origin for this late Albian or older sequence is compatible with the timing of rifting of the south Atlantic proposed by Sibuet et al. (1984) and the predicted depositional environments and lithologic signatures summarized by Pickering et al. (1989).

The lower part of lithologic Subunit VB consists of alternating lithologies of silty sandstone, sandy siltstone, and minor clayey siltstone and silty claystone (Sections 159-960A-57R-1 through 61R-CC). The presence of scoured basal contacts exhibited by some fining-upward units within the sedimentary sequence probably suggests that density currents periodically deposited sediments within the lake. As the environment became deeper, finely laminated silty claystone was deposited (Sections 159-960A-53R-CC, 23 cm, through 56R-CC, 2 cm).

The silty claystone is overlain by massive to finely laminated siliciclastic sediments containing pyrite and cemented by siderite. These claystones are slightly to heavily bioturbated and contain a few fossils. If interpretation of lithologic Subunit VB as a deep lacustrine environment is correct, then lithologic Subunit VA could reflect the onset of brackish conditions (formation of siderite and pyrite) as a result of inundation by marine waters. Pyrite framboids and marcasite crystals disseminated throughout these sediments, in contrast to lithologic Subunit VB, indicate a shift to a marine setting where sulfate would be available from overlying seawater.

The upper contact of lithologic Unit V is marked by an unconformity beneath the quartz sand and intraclast-rich limestones of lithologic Subunit IVB. Even though the contact between these units is obscured by drilling disturbance, an unconformity is inferred based on several observations. The graded sandstones of the upper part of lithologic Unit VA are deformed by synsedimentary slumping with overturned beds. These beds are also brittle fractured with veins

mineralized by kaolinite and siderite. Such veins have not been observed in the overlying limestones. Moreover, the basal limestones of lithologic Subunit IVB contain abundant lithoclasts of cemented siltstone and sandstone derived from the underlying unit. Independent of the extent of erosional deflation across this surface, the boundary between lithologic Unit V and lithologic Subunit IVB represents a marked shift in the depositional environment.

Marginal Marine, Shallow Shelf to Basinal Setting—Erosion of the Marginal Ridge

The limestone sequence present at Site 960 suggests deposition in deeper water settings basinward of a shallow-water carbonate platform. These limestones, although formed in shallow water (evidenced by the abundance of benthic green and red algae, ooids, and shallow benthic mollusks) are intercalated with thin-bedded, foraminifer-rich packstones that cap the coarse bioclastic and intraclastic grainstones. Such a lithology is indicative of allochthonous deposits (allodapic limestones of Meischner, 1964) reflecting the periodic seaward delivery of sediment into deeper water, quiescent conditions. The absence of coarse reefal debris or reefal breccia argues against deposition in a proximal, fore-reef setting dominated by reef talus. Rather, the lithology recovered at Site 960 as well as at Site 959, must reflect more distal, periplatform deposition of platform- and slope-derived sediment (Enos and Moore, 1983). These most closely resemble grain-flow deposits that might form in response to episodes of bank margin oversteepening and collapse or seaward transport as storm deposits. Notably, reefal or platform interior limestone facies were not observed at either Site 959 or Site 960.

The progression of lithologic change within the limestone interval suggests that the proximity of the platform to Site 960 changed through time. Overall, Subunit IVB grades upward from distal, siliciclastic-rich, gravity-flow deposits into relatively pure limestones. However, the abundance of siliciclastic grains again increases in the upper part of lithologic Subunit IVB. This stratigraphic pattern could result from either the rejuvenation of the source of the clastic sediments, a migration of the siliciclastic source (e.g., delta or estuarine migration) or a change in the proximity of the carbonate platform. Based on the initial paleontologic correlations, the first limestones at Site 959 may be older than those occurring at Site 960. If correct, the diachroneity of this unit would imply a regional migration of the carbonate platform in response to either eustatic or tectonic changes in sea level.

The diagenetic history of these limestones could provide additional constraints on fluctuations in sea level over the Marginal Ridge. The development of vuggy porosity, resulting from the dissolution of aragonitic bioclasts, could have resulted from periodic subaerial exposure of this sequence and subsequent alteration by meteoric waters. Furthermore, the development of equant calcite cements filling this porosity, and the resultant preservation of micritic envelopes, requires a setting of early cementation prior to extensive burial compaction. These observations, however, are not conclusive evidence of subaerial exposure, given that dissolution of aragonitic bioclasts and early cementation can also occur under deep marine conditions. Nevertheless, they are consistent with the regional tectonic model that provides for episodic relative uplift and subsidence of the Marginal Ridge.

Submergence of Marginal Ridge—Sediment-starved Shelf

The lithologic transition from limestones of lithologic Subunit IVB into hardgrounds and glauconitic and phosphatic sediments of Subunit IVA requires inundation of the underlying carbonate platform by deeper marine waters in response to either basin subsidence or a rapid rise of sea level. Changes in the lithology at Site 959 are compatible with observations made at this site. For example, the completeness of lithologic Subunit IVA with biogenic phosphate and

glauconite suggests that it may be correlated with the base of lithologic Unit III at Site 959 in Cores 159-959D-52R through 66R. Specifically, the reworked biogenic phosphate and glauconite pebbles of Core 159-959D-66R may correspond to the enrichments in fish debris and glauconite layers observed at the top of lithologic Unit IV at Site 960. At Site 959, these coarse sediments are late Coniacian to early Santonian in age, which coincides with one of the ages provided for Core 159-960A-21R.

The preponderance of authigenic minerals and the reduced thickness of lithologic Unit III and lithologic Subunit IVA at Site 960 can be explained by sediment starvation on a Marginal Ridge isolated from external terrigenous clastic sediment supply. Currents could have swept sediment from the crest of that ridge into deeper environments such as the one envisaged for the black claystones at Site 959 (lithologic Unit III). Cessation of clay deposition, except from eolian sources, would promote the formation of authigenic minerals. Such a scenario is compatible with the observations of lithologic Subunit IVA made at Site 960, where more than 10 m.y. is represented by less than 10 m of sediment accumulation. Similar conditions of a low terrigenous or pelagic flux of sediment must have prevailed for the deposition of the palygorskite claystones of lithologic Unit III.

The blue claystones with barite nodules encountered in lithologic Unit III at Site 960 are characterized by the scarcity of both detrital and biogenic components. In turn, they contain palygorskite, sepiolite, and smectite that point to alkaline chemical sedimentation (Millot, 1964). Palygorskite and sepiolite are fibrous, Mg-rich clay minerals that require high pH and elevated concentrations of Si and Mg to precipitate (Kastner, 1981). Both palygorskite and sepiolite are known to form in soils and duricrusts of arid and subarid zones and in lacustrine and shallow marine environments (Singer and Galan, 1984). They also form in the deep sea in the proximity of volcanic ridges by the alteration of ocean-floor basalt (Bonnatti and Joensuu, 1968; Couture, 1977), but this process is thought to contribute only a minor portion to the widespread occurrence of palygorskite-sepiolite (Chamley, 1989).

The unusual enrichment of palygorskite in lithologic Unit III could be explained as a result of differential settling processes that tend to favor the continued suspension of smectite (probably also palygorskite and sepiolite) and transport into distal environments while other clay minerals (chlorite, illite, and, notably, kaolinite) segregate earlier (Gibbs, 1977). Deconinck et al. (1985) have made the case that differential segregation has had a more pronounced effect on the composition of clays off the shelf in the geologic past due to increased shelf areas, which acted as traps for the easily segregated minerals. The presence of kaolinite in lithologic Unit III, however, does not support this explanation. Eolian transport has also been cited as responsible for palygorskite accumulations in the sea other than in chemical sedimentary environments (Tomadin et al., 1984; Coudé-Gaussen and Blanc, 1985; Debrabant et al., 1993) but the scarcity of silt-sized quartz renders this interpretation unlikely.

Alternatively, Weaver and Beck (1977) described brackish shallow marine and lacustrine environments where palygorskite and sepiolite deposits formed by transformation of Al-Fe smectites (beidelites). They concluded that many other palygorskite-sepiolite deposits might also have formed in shallow water marked by elevated temperature and strong evaporation.

The association of palygorskite-sepiolite deposits with authigenic carbonates, chert, phosphate, sulfates, glauconite, and organic matter is common along the latest Cretaceous to Paleogene Atlantic seaboard of Africa (Lucas and Prévôt, 1975) and particularly abundant in early Eocene marginal marine basins of western Africa (Millot, 1964, 1970; Chamley, 1989). According to these authors, the widespread occurrence of this association is related to strong leaching of alkaline ions from the hinterland during a phase of low detrital input.

In light of these studies, we interpret the palygorskite-rich claystone to have formed in a restricted shallow shelf environment char-

acterized by high evaporation rates induced by a hot, semiarid climate. The low clastic input likely resulted from the geographic isolation of the Marginal Ridge from the nearby continent.

The source of barium and the mechanism responsible for precipitation of the abundant barite concretions is not known. Degradation of terrigenous organic matter present in the coeval carbonaceous black claystones observed at Site 959 might have supplied the dissolved Ba to form barite concretions either syndepositionally or during early diagenesis.

Passive Margin Subsidence—Pelagic and Hemipelagic Deposition

The transition from the Mg-rich palygorskite clays of lithologic Unit III to the chert, biosiliceous and biocalcareous claystones of lithologic Unit II is poorly recovered in both holes at this site because of the drilling problems caused by chert. No large time gap is apparent between these two units, however, as the top of lithologic Unit III and the base of lithologic Unit II are both assigned to nannofossil Biozone CP10 (early Eocene; see "Biostratigraphy" section, this chapter). The chert is apparently interbedded with normal pelagic sediment, such as nannofossil chalk and biosiliceous (now porcellanite) sediment. The transition from a "shallow shelf setting" with high evaporation rates and restricted circulation to a normal pelagic marine setting was probably a gradual one, considering the units are the same age, although the actual contact was not observed. The transition could be effected by a sea-level rise and/or by the gradual subsidence of the Marginal Ridge. Such a deepening at this site is necessary to establish the open circulation with normal marine waters that is required for the formation of chert and porcellanites.

At the onset of deposition of lithologic Unit II, therefore, Site 960 was in an open-marine, unrestricted setting and in communication with the rest of the world's oceans. These were also experiencing the conditions that led to the deposition of Horizon A^c, a lower to middle Eocene chert layer found across the Atlantic, northwest Pacific, and Indian Oceans (e.g., Pisciotto, 1981), and correlative to lithologic Subunit IIB at this site. Although an influx of nutrients may explain a local or regional enrichment in biosiliceous matter to a basin, a global effect is more likely for this interval at Site 960. This effect may have been cyclical for a time, as indicated by alternations of chert with calcareous sediment.

Even before the onset of normal pelagic conditions at this site, large amounts of glauconitic material began to form (i.e., just above the palygorskite clay). This green, iron-rich material is a common component in continental shelf sediment today (e.g., Odin and Matter, 1981). It forms in slightly cooler (deeper) waters than its shallow tropical waters counterpart, odinite, which is found in very shallow marine waters of tropical areas where the water temperature is warmer than 25°C (Odin and Matter, 1981; Bailey, 1988). Aside from this distinction, glauconite pellets, films, and hardgrounds are not indicative of any particular water temperature, depth, sedimentation rates, or salinity, other than that they form only in a marine environment (Odin and Matter, 1981; McRae, 1972; the latter cites one possible lacustrine occurrence). The mineral composition of this green material is widely variable, and confusion has arisen over whether the term "glauconite" refers to the green material itself or to a ferric mica of distinct mineralogical structure. Odin and Matter (1981) suggested the term "glaucony" for the green material and "glauconite" for the mineral. However, this terminology has not found widespread use in American literature, where the terms "glauconitic pellets" and "mineralogical glauconite" are preferred (e.g., Thompson and Hower, 1975; Odum, 1984). In general, the green material evolves over time from various starting materials, through a smectite, to interlayered glauconite/smectite, and finally to mineralogical glauconite. The degree to which the material has become mineralogical glauconite (a 10-Å mineral) is an indication of the length of the depositional hiatus that promoted its formation (Odin and Matter, 1981). The other conditions that

promote glauconitization include organic matter in confined spaces (i.e., pores), oxidizing conditions in the water above the sediment/water interface, locally reducing conditions in the sediment, and marine transgression or shelf subsidence (Odin and Matter, 1981). Frequent currents, which redistribute grains being altered to glauconite, allow the grains to come in contact with fresh sources of potassium and iron and promote new mineral growth. Such an environment is generally an outer shelf to upper slope. Most glaucony today is found in water depths from 100 to 500 m, and at latitudes from equatorial to 50°S and 65°N.

Three samples were examined by XRD from lithologic Unit II in Hole 960C, and none of them indicates mineralogical glauconite (Fig. 30), but all contain smectite or some 10/17-Å mixed-layer minerals. The zeolite, clinoptilolite, is present, as well as kaolinite and detrital illite. The absence of mineralogical glauconite suggests that the hiatuses involved in the alteration of pelletal material, and the formation of films and hardgrounds in this sediment, are on the order of 10³–10⁴ yr by comparison with similar material on modern shelves (Odin and Matter, 1981).

The occurrence of biosiliceous sediment at this site after the middle Eocene and through the early Miocene indicates that the local conditions of upwelling or increased continental runoff that promoted blooms of diatoms and/or radiolarians at Site 959 (see "Lithostratigraphy" section, "Site 959" chapter, this volume) persisted at Site 960 for this time as well. The section is greatly condensed here (36–48 m thick) compared to that at Site 959 (248 m). Site 960 on the ridge top was clearly subject to greater winnowing effects.

The same holds true for lithologic Unit I, which is fairly typical of pelagic, calcareous sediment, but is approximately one-half as thick as it is at Site 959 and is more enriched in glauconite pellets and films. Lithologic Unit I accumulated in a normal, open-marine environment. Whatever the conditions were that promoted enhanced siliceous productivity, they were terminated in the early Miocene and have not recurred. This area has been subject to greater winnowing than Site 959, as indicated by more scoured surfaces and nascent hardgrounds and decreased sediment thickness. The darker beds of lithologic Unit I indicate periods of decreased carbonate accumulation, as indicated by increased micrite and terrigenous debris levels. The lack of glauconitization in these beds suggests that they do not represent hiatuses, but perhaps periods of increased terrigenous input, such as that caused by storms.

Summary

1. Lithologic Unit V represents a synrift stage, comprising lacustrine siltstones and claystones that grade upward into deep-shelf marine sandstones. This sequence is terminated by an unconformity where lithologic Unit V sandstones were deformed, uplifted, and eroded.
2. Lithologic Subunit IVB, comprising carbonate grain and debris flows, formed in deeper, sub-wave base settings adjacent to shallow carbonate platforms containing local reefs and oolitic shoals. The abundance of coarse, subangular quartz and feldspar siliciclastics associated with these limestones suggests coeval clastic and carbonate deposition around the margin of an exposed and eroding highland composed of sedimentary and metamorphic bedrock. Periodic sea-level rises and falls, exposing the carbonate terrain to subaerial weathering, are suggested by diagenetic features present within these limestones. Such fluctuations could result from either tectonic uplift and subsidence, or minor eustatic changes in sea level. This sequence, spanning Turonian through Coniacian time, was terminated by deepening and flooding of both the marine platform and the highland clastics source area, cutting off the delivery of terrigenous clastics.

3. Lithologic Subunit IVA and lithologic Unit III were formed after submergence of the Marginal Ridge. Lithologic Subunit IVA is a condensed/hiatal interval spanning more than 10 m.y. (Coniacian through Maastrichtian) comprising less than 10 m of glauconitic hardgrounds and phosphatic debris. The unusual occurrence of the lower Eocene palygorskite claystones and barite nodules of lithologic Unit III directly above lithologic Subunit IVA requires a depositional setting with low sediment-accumulation rates under conditions of warm, marine waters of possibly elevated salinity. Such a setting could develop across the broad upper surface of the submerged Marginal Ridge if sea level were lowered or the ridge uplifted, but without exposure of the underlying sediment surface. This could allow for local concentration of Mg and precipitation of Mg-rich clays, while maintaining normal marine conditions at Site 959 where siliceous microflora were abundant. Lithologic Subunit IVA and lithologic Unit III at Site 960 are roughly equivalent in age to the black claystones and porcellanites at Site 959.
4. Continued subsidence of the Marginal Ridge reestablished deeper, normal marine conditions at this site, and allowed for basin-wide deposition of the early Eocene to late Oligocene cherts and porcellanites (lithologic Subunits IIA and IIB at Site 960 and lithologic Subunits IIB and IIC at Site 959). Continued subsidence of this region from early Eocene through Holocene is recorded by the progression of pelagic and hemipelagic deposition recorded in diatomites and nannofossil/foraminifer cherts and oozes.

BIOSTRATIGRAPHY

Introduction

Rotary drilling (RCB) in Hole 960A severely disturbed the Pleistocene and Pliocene portions of the sequence, and recovery rates throughout the Cenozoic interval were typically only one to three sections per core. Hole 960B consisted of a single mud line core that penetrated to 7.1 mbsf; only the core catcher was studied. The combination of advanced piston corer (APC) and extended core barrel (XCB) coring in Hole 960C provided excellent recovery rates through nearly the entire cored sequence, so that we analyzed one sample per section through 129.7 mbsf (first 14 cores). Biostratigraphic control was provided by shipboard analyses of calcareous nannoplankton and planktonic foraminifers. Eocene radiolarians were also identified in Hole 960C.

Coring at Site 960 recovered a discontinuous sequence of Pleistocene to Turonian deposits. The pelagic drape includes a biostratigraphically complete early Pleistocene to latest Miocene sequence from the mud line to 75 mbsf in Hole 960C. This same interval is thinner by about 23 m in Hole 960A partly because of an unconformity or condensed section in the latest Pliocene that is not present in Hole 960C. Hole 960C was offset by about 100 m downslope from Hole 960A to a location where seismic stratigraphy indicates that the stratigraphic section is more expanded. A second unconformity has removed most of the late middle Miocene in both holes in Cores 159-960A-8R and 159-960C-10H. Early Miocene to early middle Miocene deposits are present in a condensed section between Cores 159-960C-10H and 159-960C-14H (91.5–130.0 mbsf). Early to middle Eocene radiolarian-bearing sediments occur below this unconformity and contain intervals of nannofossil-foraminifer chalk as deep as Core 159-960C-22X (198.0 mbsf). Eocene deposits rest directly on Cretaceous sediments at this site. Early Eocene nannofossils were found at about 164 mbsf in Hole 960A. At this same level, Late Cretaceous foraminifers together with Coniacian-Santonian nannofossils also were found. Similarly, Coniacian to Santonian foraminifers and nannofossils are present in a lag in Core 159-960C-23X (207 mbsf),

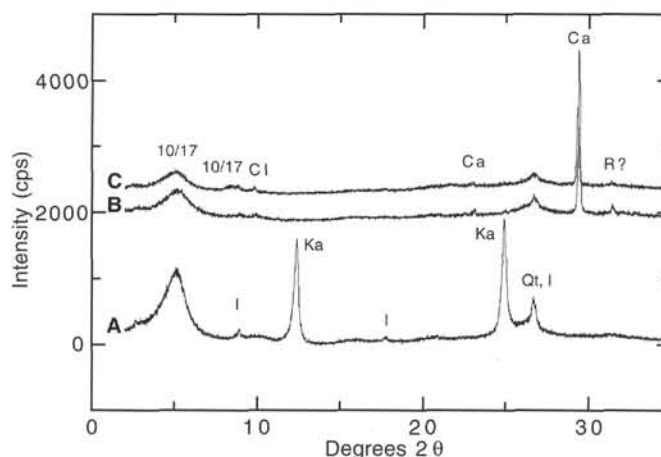


Figure 30. X-ray diffractograms of clay separates treated with ethylene glycol from glauconitic sediment, lithologic Unit I. 10/17 = 10/17-Å mixed-layer clay; I = discrete illite; Cl = clinoptilolite; Ka = kaolinite; Ca = calcite; Qt = quartz; R? = possible rhodochrosite. **A.** Sample 159-960C-13H-3, 141–143 cm. Mixed-layer 10/17-Å mineral is randomly interstratified with about 25% 10-Å layers. Detrital illite, nonferric, is indicated by the peak near 17° 2θ. Kaolinite and quartz are also present. **B.** Sample 159-960C-17X-1, 144–146 cm. Mixed-layer mineral is probably enriched in iron, as indicated by the absence of a peak near 17° 2θ. Calcite and quartz are also present, as is a trace of the zeolite, clinoptilolite. **C.** Sample 159-960C-19X-CC, 23–25 cm. Mixed-layer 10/17-Å mineral is randomly interstratified; interference from a clinoptilolite peak at 9 Å prevents estimation of the percentage of 10-Å layers. Calcite and quartz are also present.

immediately below early Eocene nannofossils in the same core. A similar lag at 352 mbsf in Core 159-960C-26X contains Turonian calcareous microfossils.

Calcareous Nannofossils

Hole 960A

A Pleistocene to lower Eocene sequence of nannofossil assemblages was identified in the first 20 cores from Hole 960A. This sequence is interrupted by two barren intervals, and contains at least two major hiatuses. The long middle Miocene Zone CN5 is missing. Nannofossils representing the time interval from Zone CP14 (middle Eocene) through to the top of Zone CP19 (late Oligocene) are missing. A barren interval characterizes the Neogene/Paleogene boundary. The lower/middle Eocene section also contains a barren interval near its base.

Sample 159-960A-1R-CC (1.2 mbsf) contains a well-preserved assemblage of calcareous nannofossils including small *Gephyrocapsa* spp., *Pseudoemiliania lacunosa*, *Pontosphaera indoceanica*, *Helicosphaera sellii*, and *Florisphaera profunda*, without the association of *Gephyrocapsa caribbeanica*, *G. oceanica*, or *Discoaster brouweri*. This indicates early Pleistocene Subzone CN13a. A similar early Pleistocene assemblage was retrieved from Sample 159-960A-2R-CC (10.6 mbsf).

Moderately preserved assemblages in Section 159-960A-3R-1 include common *Calcidiscus macintyrei* and *Pseudoemiliania lacunosa*, and frequent *Helicosphaera sellii*, *Discoaster brouweri*, *D. pentaradiatus*, and *D. surculus*. This indicates the upper part of Zone CN12 of late Pliocene age. The core catcher of Core 159-960A-3R (19.9 mbsf) contains a similar association of key species, with the addition of rare *Discoaster tamalis* and *D. asymmetricus*. This assemblage indicates the earlier Pliocene Subzone CN12a. Samples 159-960A-4R-CC through 5R-CC (29.6–39.3 mbsf) yielded assemblages

containing common *Reticulofenestra pseudoumbilica*, *Sphenolithus abies*, and *S. neobabies*, in addition to *Discoaster asymmetricus*, *D. surculus*, *D. pentaradiatus*, *D. brouweri*, and *Amaurolithus* spp. These assemblages are assigned to early Pliocene Zone CN11. The presence of low numbers of *Discoaster asymmetricus* in these assemblages suggests Subzone CN11a. Sample 159-960A-6R-CC (49.1 mbsf) contains an assemblage assignable to earliest Pliocene Subzone CN10b, based on the presence of (rare) *Ceratolithus acutus* and *C. armatus*.

This site contains a condensed Miocene section, apparently with a significant hiatus. Middle Miocene Zone CN5, which spans an interval of more than 3 m.y., according to Berggren et al. (in press), seems to be missing. Most of the identified zones/subzones are represented by thin segments of sediments, suggesting periods of very slow rates of deposition and/or nondeposition during much of the Miocene. Thus, in the 13.3-m-thick section comprising Samples 159-960A-7R-CC (58.9 mbsf) and 9R-2, 110 cm (68.6 mbsf), Zones CN9 through CN6 are identified.

Assemblages from Samples 159-960A-7R-CC through the top of Section 159-960A-9R-1 are assigned to the late Miocene Zone CN9, based on the presence of *Discoaster quinqueramus*. Sample 159-960A-7R-CC (58.9 mbsf) contains *Amaurolithus delicatus* and *A. primus*, which indicate Subzone CN9b. Species of *Amaurolithus* are absent from Samples 159-960A-8R-CC and 9R-1 (3–4 cm) (78.34 mbsf), suggesting Subzone CN9a. Sample 159-960A-9R-1, 19–20 cm, lacks *D. quinqueramus*, but contains *Minylitha convalis*, *Discoaster neohamatus*, and *D. prepentaradiatus*, suggesting Zone CN8. Assemblages from Samples 159-960A-9R-1, 130–131 cm, through 9R-2, 60 cm, include *Discoaster hamatus*, and are assigned to Zone CN7. Middle Miocene Zone CN6 is based on assemblages from Samples 159-960A-9R-2, 90 cm, and 9R-2, 110 cm. These contain *Catinaster coalitus*, without the association of *Discoaster hamatus*. Some reworking in the lower sample of Zone CN6 (159-960A-9R-2, 110 cm) is evident, with *Sphenolithus heteromorphus* (restricted to Zones CN3 and CN4) and *Triquetrorhabdulus carinatus* (disappears within Zone CN2) being present in it.

A hiatus exists between Samples 159-960A-9R-2, 110 cm, with an assemblage suggestive of Zone CN6, and 159-960A-9R-2, 140–141 cm, with an assemblage indicative of Zone CN4. Zone CN5 apparently is missing. The agent(s) that caused this hiatus may have caused the reworking evident in Sample 159-960A-9R-2, 110 cm.

Assemblages of Zone CN4 were retrieved from Samples 159-960A-9R-2, 140–141 cm through 9R-CC (78.3 mbsf). They include the index species *Sphenolithus heteromorphus*, in addition to *Calcidiscus macintyreii*, *Coccolithus miopelagicus*, *Cyclicargolithus floridanus*, *Discoaster braarudii*, *D. deflandrei*, *D. exilis*, *D. sanmigleunis*, *D. signus*, *Helicosphaera granulata*, *H. kamptneri*, and *Reticulofenestra pseudoumbilica*. Early Miocene Zone CN3 is represented by the thin interval from Samples 159-960A-10R-3, 80 cm, through 10R-3, 130 cm. Assemblages from these samples include common *Helicosphaera ampliaptera* and *Reticulofenestra gartneri*, together with *Sphenolithus heteromorphus*. The long Zone CN2 (more than 5 m.y., according to Berggren et al., in press) also is represented by a thin sequence of sediments bracketed between Samples 159-960A-10R-3, 130 cm, and 11R-CC (82.6–97.6 mbsf). Thus, an assemblage assignable to Zone CN2 was identified in Sample 159-960A-10R-CC (88.0 mbsf). It includes *Sphenolithus belemnus*, *Helicosphaera ampliaptera*, and *Reticulofenestra gartneri*. Assemblages assignable to Subzone CN1c of early early Miocene age were recorded from Samples 159-960A-11R-CC (97.6 mbsf) through 12R-1, 120–121 cm. These lack both *Sphenolithus belemnus* and *Helicosphaera ampliaptera*, but contain *Discoaster druggii*, *Helicosphaera intermedia*, *Reticulofenestra gartneri*, *Triquetrorhabdulus carinatus*, and *T. milowii*. The basal part of Zone CN1 was identified in Sample 159-960A-12R-2, 94–95 cm. This is based on the presence of *Cyclicargolithus abisectus*, *C. floridanus*, *D. deflandrei*, *Helicosphaera*

truempyii, *R. gartneri*, *R. lockeri*, *Sphenolithus conicus*, *S. moriformis*, *Triquetrorhabdulus auritus*, and *T. carinatus*. The remaining sections of Core 159-960A-12R, including the core catcher, through Sample 159-960A-14R-1, 4 cm (118.4 mbsf) are barren of calcareous nannofossils, with the exception of Sample 159-960A-13R-CC (116.9 mbsf) in which traces of *C. floridanus* and *T. carinatus* were found.

Sample 159-960A-14R-CC (126.6 mbsf) contains *Chiasmolithus expansus*, *C. solitus*, *Coccolithus formosus*, *Discoaster barbadiensis*, *D. saipanensis*, *Helicosphaera lophota*, *Nannotetrina pappii*, *N. quadrata*, *Neococcolithites dubius*, *Reticulofenestra dictyoda*, and *Sphenolithus radians*. This assemblage is assignable to middle Eocene Zone CP13. The assemblage in Sample 159-960A-15R-CC (136.2 mbsf) includes *Campylosphaera dela*, *Chiasmolithus grandis*, *Cyclicargolithus gammation*, *Discoaster cruciformis*, *D. kuepperi*, *D. lodoensis*, and *D. sublodoensis*. It is assignable to early Eocene Subzone CP12a. The assemblage in Sample 159-960A-16R-CC (145.8 mbsf) contains *C. dela*, *Chiasmolithus eograndis*, *C. solitus*, *Cyclicargolithus gammation*, *D. kuepperi*, and *D. lodoensis*. This suggests early Eocene Zone CP11, based on the absence of both the younger *D. sublodoensis* and the older *Tribrachiatulus orthostylus*. Sample 159-960A-17R-CC (155.2 mbsf) contains a residual assemblage that includes *T. orthostylus*, as well as *C. gammation*, *Discoaster gemmifer*, *D. kuepperi*, and *D. lodoensis*. This assemblage suggests early Eocene Zone CP10. The core catchers of Cores 159-960A-18R and 19R (164.8–174.5 mbsf) were barren of calcareous nannofossils. Sample 159-960A-20R-1, 108 cm (175.58 mbsf) contains a residual assemblage of *Discoaster multiradiatus/barbadiensis*, *D. binodosus*, *D. diastypus*, *D. elegans*, *D. kuepperi*, *Sphenolithus radiatus*, and *T. orthostylus*. This assemblage is assigned to the early Eocene interval CP9b/CP10, because of the co-occurrence of *D. kuepperi* and *T. orthostylus*, with the apparent absence of *D. lodoensis*. A few specimens of *D. multiradiatus/barbadiensis* and *T. orthostylus* found in Sample 159-960A-20R-CC (184.1 mbsf) indicate that this sample is still within Subzone CP9b. In a preparation from a lighter colored lithology in the same core catcher (159-960A-20R-CC), Late Cretaceous nannofossil species were found. These include *Eiffellithus eximius*, *Lithastrinus septenarius*, *Manivitella pemmatoides*, *Marthasterites furcatus*, *Micula concava*, *M. decussata*, *Pre-discosphaera cretacea*, *Watznaueria barnesae*, and *W. biporta*. Cores below Sample 159-960A-20R-CC (184.1 mbsf) are barren of calcareous nannofossils.

Hole 960C

A sequence of calcareous nannofossil assemblages ranging in age from Pleistocene to Turonian is identified from Cores 159-960C-1H through 26X. Within this sequence at least three pronounced hiatuses could be detected. One of these hiatuses, between early Miocene and middle Eocene assemblages, is associated with a barren interval in Core 159-960C-15H; three barren intervals were identified within the Turonian-Pleistocene sequence. The youngest hiatus is within Core 159-960C-10H, separating sediments with assemblages assignable to late Miocene Zone CN7 from those of early middle Miocene Zone CN4. The oldest hiatus is within Core 159-960C-23X, between assemblages assignable to early Eocene Zone CP9 and others of Coniacian to Santonian age.

Sample 159-960C-1H-2, 18–20 cm (1.7 mbsf) contains *Calcidiscus leptoporus*, *?Emiliania huxleyii*, *Florisphaera profunda*, *Gephyrocapsa caribbeanica*, *G. oceanica*, *Helicosphaera hyalina*, *H. kamptneri*, *H. neogranulata*, *Syracosphaera pulchra*, and *Umbilicosphaera sibogae*. This assemblage suggests late Pleistocene Subzone CN14b or the younger Zone CN15. Sample 159-960C-1H-CC (6.2 mbsf) contains a similar assemblage, with the addition of *Pseudoeumiliana lacunosa*, and is assigned to early Pleistocene Subzone CN14a. The Pleistocene/Pliocene boundary, approximated by the ex-

tion of discoasters, is within the bottom of Core 159-960C-2H. Sample 159-960C-2H-6, 35–37 cm (14.07 mbsf) lacks the large *Geophyrocapsa* spp. (such as *G. caribbeanica* and *G. oceanica*) as well as *Discoaster* spp. and contains *Calcidiscus macintyreii* and *Helicosphaera sellii* instead. This suggests Subzone CN13a (or the *C. macintyreii* Zone of Gartner, 1977). Late Pliocene Zone CN12 was identified in the core catchers of Cores 159-960C-2H and 3H. An assemblage containing *Ceratolithus rugosus*, *Coccolithus pelagicus*, *Discoaster brouweri*, *Florisphaera profunda*, *Helicosphaera sellii*, *Pontosphaera japonica*, and *Rhabdosphaera clavigera* in Sample 159-960C-2H-CC (15.7 mbsf) indicates Subzone CN12d. A similar assemblage was recorded from Sample 159-960C-3H-CC (25.2 mbsf) but with the notable addition of *Discoaster pentaradiatus* and *D. surculus*, suggesting Subzone CN12b.

Sample 159-960C-4H-CC (34.7 mbsf) contains *Ceratolithus rugosus*, *Discoaster asymmetricus* (common), *D. brouweri*, *D. tamalis*, *Helicosphaera sellii*, *Pontosphaera indoceanica*, *Sphenolithus abies* (common), *S. neoabies* (abundant), *Pseudoemiliania lacunosa* (frequent), and *Reticulofenestra minutula*. This assemblage is assignable to either Subzone CN12a or CN11b. The lower/upper Pliocene boundary is usually drawn at the base of Subzone CN12a or the top of Subzone CN11b, at the disappearance of *Reticulofenestra pseudoumbilica*, *S. abies*, and *S. neoabies*. The younger assignment (Subzone CN12a) is based on the absence of *R. pseudoumbilica*, but does not consider the common *S. abies* and *S. neoabies*. The common presence of *D. asymmetricus*, *S. abies*, and *S. neoabies* favors assignment to Subzone CN11b. In both Samples 159-960C-5H-CC and 6H-CC (44.2–53.7 mbsf) *R. pseudoumbilica* is present (together with *S. abies*, *S. neoabies*, and other Neogene species such as *Ceratolithus rugosus*, *D. brouweri*, and *D. pentaradiatus*, and *D. surculus*), but *D. asymmetricus* is either absent or extremely rare. This suggests early Pliocene Subzone CN11a. The assemblage in Sample 159-960C-7H-CC (63.2 mbsf) contains rare *Ceratolithus acutus* and *C. armatus*, indicating earliest Pliocene Subzone CN10b.

The assemblage in Sample 159-960C-8H-CC (72.7 mbsf) includes *Amaurolithus delicatus*, *Coccolithus miopelagicus*, *Discoaster pansus*, *D. quinqueramus*, *D. surculus*, *D. variabilis*, and *Triquetrorabdulus rugosus*. This association indicates Subzone CN9b of late Miocene age. Samples 159-960C-9H-CC through 10H-3, 143 cm (82.2–86.63 mbsf), contain assemblages assignable to late Miocene Subzone CN8b. *Discoaster neorectus*, *D. pentaradiatus*, and *Minylitha convalis* were noted among the assemblage in Sample 159-960C-9H-CC. In Sample 159-960C-10-3, 143 cm, *D. pentaradiatus* is absent or extremely rare, but *D. prepentaradiatus* is present. Also present in this sample are *D. bollii*, *D. braarudii*, *D. neohamatus*, *D. neorectus*, *Minylitha convalis*, and *T. rugosus*. The assemblage in Sample 159-960C-10-5, 34–36 cm, lacks both *D. neorectus* and *Minylitha convalis*, but contains *D. hamatus*, and is assigned to early late Miocene Zone CN7.

A hiatus exists between Samples 159-960C-10H-5, 34–36 cm (Zone CN7), and 10H-7, 34–36 cm (Zone CN4); Zones CN6 and CN5 are missing. Early middle Miocene Zone CN4 is found in Samples 159-960C-10H-7, 34–36 cm, through 10H-CC (87.74–91.7 mbsf), based on assemblages containing *Discoaster exilis*, *D. sanmiguelis*, and *Sphenolithus heteromorphus*. Sample 159-960C-11H-CC (101.2 mbsf) contains a similar assemblage, with the notable addition of *Helicosphaera ampliaptera*. This indicates early Miocene Zone CN3, which is based on the co-occurrence of *S. heteromorphus* and *H. ampliaptera*. Assemblages indicative of early Miocene Zone CN2 occur in Samples 159-960C-12H-CC through 13H-3, 43 cm (110.7–114.13 mbsf). These include *Orthorhabdus serratus*, *Sphenolithus belemnus*, and *Reticulofenestra gartneri*, in addition to *H. ampliaptera*, *H. intermedia*, and *Triquetrorabdulus carinatus*. Both *S. belemnus* and *H. ampliaptera* are absent from Sample 159-960C-13H-6, 83 cm (118.03 mbsf). In this sample, earliest Miocene Subzone CN1c was identified, based on the occurrence of *Discoaster*

druggii and *Orthorhabdus serratus*, in addition to *Helicosphaera intermedia*, *H. obliqua*, and *T. carinatus*.

Samples 159-960C-13H-CC and 14H-CC (120.2 and 129.7 mbsf) are barren of calcareous nannofossils. However, abundant nannofossils are present in Samples 159-960C-14H-3, 57–58 cm, and 14H-5, 51 cm (120.48–123.41 mbsf). These lack the key species for earliest Miocene Subzone CN1c (*D. druggii* and *O. serratus*) found in Sample 159-960C-13H-6, 83 cm. *Cyclicargolithus abisectus*, *C. floridaanus*, *Dictyococcites bisectus* (rare), *D. deflandrei*, *Helicosphaera recta* (frequent), *H. truempyi*, *Sphenolithus delphix* (rare), *S. dissimilis*, and *Zygrhablithus bijugatus* (rare) in Sample 159-960C-14H-3, 57–58 cm, and *Sphenolithus ciperoensis* (very rare) in Sample 159-960C-14H-5, 51 cm indicate late Oligocene Zone CP19. Nevertheless, the key species *Dictyococcites bisectus*, *Helicosphaera recta*, *Sphenolithus delphix*, *S. dissimilis*, and *Zygrhablithus bijugatus* are not found in the assemblage from Sample 159-960C-14H-5, 51 cm. Similarly, they were not encountered in Sample 159-960C-14H-5, 145 cm, which contains the Oligocene forms *Sphenolithus distentus* and *S. predistentus* (both very rare).

Several samples from Core 159-960C-15H, including the core catcher (139.2 mbsf) are barren of calcareous nannofossils, but the radiolarians are suggestive of an Eocene age (see “Radiolarians” section, this chapter). The nannofossil evidence, however, suggests that this core may represent a very condensed section and probably contains a hiatus between essentially lower Miocene (Core 159-960C-13H), uppermost Oligocene (Core 159-960C-14H), and middle Eocene (Core 159-960C-16H) sediments.

The preservation of nannofossils is generally poor below Core 159-960C-15H, with scattered moderately preserved assemblages. Sample 159-960C-16H-CC (140.2 mbsf) contains abundant nannofossil debris, and signs of partial dissolution are evident among most coccoliths; the assemblage is enriched in discoasters. In this sample *Discoaster barbadiensis*, *D. binodosus*, *D. elegans*, *D. subloadoensis*, *D. strictus*, *Helicosphaera seminulum*, *Nannotetrina quadrata*, *N. mexicana*, *Chiasmolithus solitus*, *Reticulofenestra samodurovii*, and *Sphenolithus radians* are recorded. These suggest middle Eocene Zone CP13 (probably Subzone CP13c). A sample from the base of Section 159-960C-17X-CC (150.0 mbsf) is almost barren of calcareous nannofossils, except for a few specimens including one of *N. quadrata*, suggesting Zone CP13. However, a more diverse, better preserved assemblage than that found in this core catcher occurs in a sample from the top of Section 159-960C-17X-CC. This assemblage includes *Blackites spinosus*, *Chiasmolithus expansus*, *C. grandis*, *Coccolithus formosus*, *C. staurion*, *Neococcolithes dubius*, and *Sphenolithus furcatolithoides*, in addition to those recorded in Section 159-960C-16H-CC. It is also assignable to Zone CP13.

Rare, poorly preserved nannofossils and abundant debris of these fossils occur in Sample 159-960C-18X-CC (159.7 mbsf). The early to middle Eocene *Coccolithus magnicrassus*, *C. pelagicus*, *Discoaster barbadiensis*, *D. cruciformis*, and *S. radians* were identified in this sample. Calcareous nannofossils are more common and better preserved in Samples 159-960C-19X-CC and 20X-CC (169.4 and 179 mbsf). The more diversified assemblage in Sample 159-960C-20X-CC includes *Campylosphaera dela*, *Coccolithus formosus*, *C. magnicrassus*, *Cyclicargolithus gammaton*, *D. binodosus*, *D. gemmifer*, *D. kuepperi*, *D. lodoensis*, *Helicosphaera seminulum*, *Neococcolithes dubius*, and *Tribrachiatus orthostylus*. This association indicates Zone CP10, of early Eocene age. Two samples from Section 159-960C-21X-CC (188.8–188.6 mbsf) are barren of calcareous nannofossils. Rare and poorly preserved nannofossils were recovered from Section 159-960C-22X-CC (198.3 mbsf). These include *D. lodoensis*, the index for early Eocene Zone CP10, together with very rare *Marthasterites contortus* (which is known to disappear at the top of Subzone CP9a), *Discoaster diastypus*, *D. binodosus*, *Sphenolithus radians*, and *T. orthostylus*. Two states of preservation are noted, particularly for the discoasters, suggesting some mixing. The co-occur-

rence of mutually exclusive species (e.g., *D. lodoensis* and *M. contortus*) in the assemblage supports the notion of mixing and reworking.

Rare, strongly corroded nanofossils in Sample 159-960C-23X-1, 26 cm (198.56 mbsf) suggest an early Eocene age, whereas those (also rare) in Sample 159-960C-23X-CC (207.9 mbsf) are indicative of a Coniacian/Santonian age. The early Eocene nanofossils are mostly ortholiths, which were concentrated as the less resistant nannoliths dissolved. These ortholiths include *Discoaster elegans*, *D. diastypus*, *D. binodosus*, *D. kuepperi*, and *T. orthostylus*. This association is assignable to the interval CP9b/CP10. The Coniacian/Santonian nanofossils in Sample 159-960C-23X-CC include *Eiffellithus eximius*, *E. turriseffellii*, *Gartnerago obliquum*, *Lithastrinus septenarius*, *Manivitella pemmatoides*, *Microrhabdulus decoratus*, *Micula decussata*, *Prediscosphaera cretacea*, *Tranolithus gabalus*, ?*T. orionatus*, and *Watznaueria barnesae*. Samples 159-960C-24X-CC and 159-960C-25X-CC (210.7–343.2 mbsf) are barren of calcareous nanofossils. Sample 159-960C-26X-CC (352.8 mbsf) contains *Eprolithus floralis*, *Quadrum gartneri*, *Eiffellithus eximius*, *E. turriseffellii*, *Gartnerago obliquum*, *Manivitella pemmatoides*, *Marthasterites furcatus*, *Microrhabdulus decoratus*, *Prediscosphaera cretacea*, *Tranolithus orionatus*, and *Watznaueria barnesae*. This association suggests Zone CC13 of late Turonian age. Cores below Sample 159-960C-26X-CC are barren of calcareous nanofossils.

Planktonic Foraminifers

At Site 960, 152 samples were studied for planktonic foraminifers. Zonal assignments are summarized in Figures 31 and 32. Where foraminifers are present, preservation is generally moderate to good above the middle Miocene but becomes moderate to poor below. Many samples are entirely barren from the deeper parts of Holes 960A and 960C. A very long sequence from Section 159-960A-21R-CC (193.7 mbsf) through 61R-CC (451.2 mbsf) contains no calcareous or siliceous microfossils.

In Pleistocene Zone N22, foraminifers are abundant but only moderately preserved, since the interiors of robust species such as *Neogloboquadrina dutertrei* and *Globorotalia tumida* are entirely dissolved. Common taxa include *Globorotalia menardii*, *G. tumida*, *G. scitula*, *Pulleniatina obliquiloculata*, *Globigerinoides ruber*, *G. sacculifer*, *Neogloboquadrina dutertrei*, *N. pachyderma* (dextral), and *Orbulina universa*, which are found in Samples 159-960A-1R-CC (1.2 mbsf), 159-960A-2R-CC (10.6 mbsf), 159-960B-1H-CC (7.1 mbsf) and 159-960C-1H-CC (6.2 mbsf). *Globorotalia tosaensis*, present in Samples 159-960A-1R-CC, 159-960B-1H-CC and 159-960C-1H, 17–19 cm (0.17 mbsf), indicates lower Pleistocene Subzone N22a.

This site recovered a nearly complete record of the Pliocene. The Pleistocene/Pliocene boundary, as estimated by the last appearance of *Globigerinoides fistulosus*, is present between Samples 159-960C-2H-5, 34–36 cm (12.5 mbsf, Zone N22) and 159-960C-2H-6, 35–37 cm (14.0 mbsf, Zone PL6), as well as between Samples 159-960A-2R-CC (10.6 mbsf, Zone N22) and 159-960A-3R-1, 95–97 cm (11.5 mbsf, Zone PL3).

The presence of *Globigerinoides fistulosus*, in the absence of *Globorotalia pseudomiocenica*, identifies Zone PL6 in Sample 159-960C-2H-6, 35–37 cm. Neither species is present in Sample 159-960C-2H-7, 34–36 cm (15.5 mbsf), but both occur in the core catcher. Hence, sediment representing Zone PL6 probably is very thin and exists between about 12.5 to 15.7 mbsf. As for the early Pleistocene, foraminifers in Zone PL6 include common to abundant *N. dutertrei*, *G. sacculifer*, and *G. ruber*. Species such as *Pulleniatina obliquiloculata*, *Globorotalia crassaformis*, *G. tumida*, *N. pachyderma* (dextral), and *Sphaeroidinella dehiscens* are rare to common members of the assemblage. Foraminifers are typically moderately preserved,

with much fragmentation in the fine fraction and shell interior dissolution.

Zone PL5 extends from Sample 159-960C-2H-CC (15.7 mbsf) to 3H-5, 34–36 cm (19.0 mbsf), with the presence of *Globigerinoides fistulosus*, *Globorotalia miocenica*, and *G. pertenuis*. *Neogloboquadrina dutertrei* and *G. sacculifer* remain dominant species throughout this zone but *G. hirsuta*, *Orbulina universa*, *S. dehiscens*, *N. pachyderma* (dextral), and *G. bulloides* are also present. Downward through Zone PL5 there is a reduction in fragmentation. Large *G. pertenuis* and *G. miocenica* are preserved with glassy walls throughout their stratigraphic range.

Zone PL4 has been recognized, with the last appearance of *Dentoglobigerina altispira*, in Sample 159-960C-3H-6, 35–37 cm (23.6 mbsf) and extends through 159-960C-4H-2, 34–36 cm (27.0 mbsf). Frequent to common species in this zone include *G. multicamerata*, *D. altispira*, *G. miocenica*, *G. pertenuis*, *G. crassaformis*, *N. dutertrei*, and *G. sacculifer*. Reworked specimens of *Sphaeroidinellopsis seminulina* and *Globoquadrina venezuelana* were found as single specimens in several samples from this zone. Foraminifer preservation is good to excellent.

The last appearance of *Sphaeroidinellopsis* in Samples 159-960A-3R-1, 95–97 cm (11.5 mbsf) and 159-960C-4H-3, 34–36 cm (28.7 mbsf) identified the top of Zone PL3. Associated species include well preserved, common to abundant, *G. sacculifer*, *G. extremus*, *G. menardii*, *G. tumida*, and *N. dutertrei*. *Globorotalia multicamerata*, *G. scitula*, *G. crassaformis*, *G. puncticulata*, *G. venezuelana*, and *G. pseudomiocenica* are common to rare members of the assemblage.

Samples 159-960A-4R-1, 50–52 cm (20.4 mbsf) to 159-960A-5R-CC (39.3 mbsf), and 159-960C-5H-1, 35–37 cm (35.0 mbsf) to 159-960C-6H-2, 34–36 cm (45.5 mbsf), contain abundant *G. tumida*, *D. altispira*, rare *G. venezuelana*, and common *Pulleniatina primalis*, and few *Globorotalia margaritae*. The occurrence of *Globorotalia margaritae* and the absence of *Globigerina nepenthes* indicates Zone PL2. Near its last occurrence, in Core 159-960C-5H, *G. margaritae* has only a weak keel, but otherwise has the smooth wall and biconvex shape that distinguishes it from the co-occurring more pustulose and four-chambered *G. hirsuta*. Foraminifers are common to abundant in this zone and are well preserved.

Zone PL1 is marked by the last occurrence of *Globigerina nepenthes* between Samples 159-960C-6H-3, 34–36 cm, and 6H-5, 34–36 cm (47.6–50.5 mbsf). Zone PL1 is subdivided by the last appearance of *G. cibaoensis* and the first appearance of *G. crassaformis* (Berggren, 1977) that define the Subzone PL1a/PL1b and Subzone PL1b/PL1c boundaries, respectively. *Globorotalia crassaformis* first appears between Samples 159-960C-6H-5, 34–36 cm and 159-960C-6H-6, 34–36 cm, (50.5–52.1 mbsf). We have not been able to recognize the last appearance of *G. cibaoensis* in Hole 960C because this species is generally rare and is not consistently present in successive samples within its recorded range. Therefore, we have tentatively used the first appearance of *G. crassaformis* to subdivide Zone PL1 into Subzones PL1a-b and PL1c. Foraminifer assemblages are well preserved in Zone PL1 and are dominated by *G. venezuelana*, *G. pleistotumida*, *G. obliquus*, *G. sacculifer*, *G. menardii*, and *Sphaeroidinellopsis* spp.

The base of the Pliocene is marked by the first appearance of *Globorotalia tumida*. *G. tumida* is present as low as Samples 159-960A-7R-2, 106–108 cm (52.2 mbsf), and 159-960C-8H-5, 34–36 cm (69.5 mbsf), but it is absent in Samples 159-960A-7R-3, 108–110 cm (53.8 mbsf), and 159-960C-8H-6, 34–36 cm (71.0 mbsf). Preservation is good across the boundary and indicates that the first appearance of *G. tumida* is not affected by dissolution.

Upper Miocene Zone M14 is indicated from Sample 159-960A-7R-3, 108–110 cm to the bottom of Core 159-960A-8R (68.6 mbsf) by the presence of *G. margaritae* and the absence of *G. lenguaensis*.

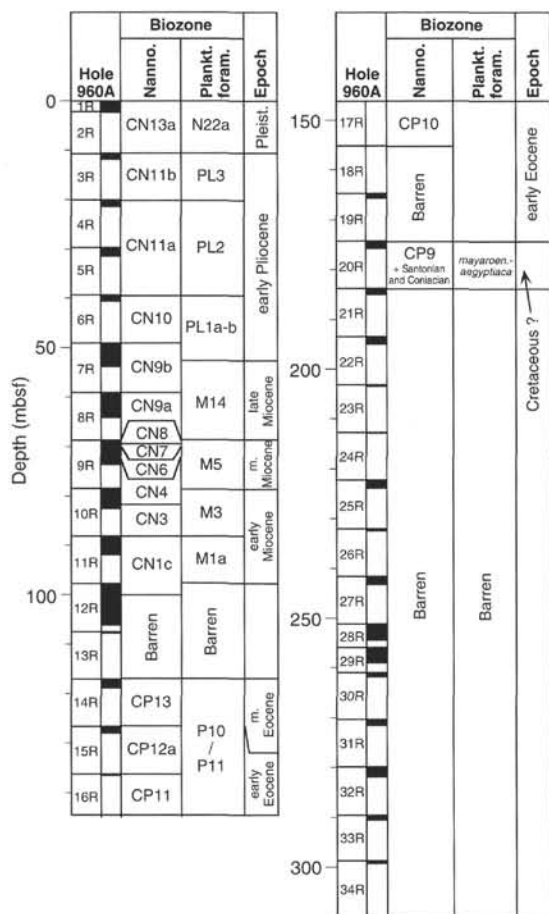


Figure 31. Biostratigraphic correlation of Hole 960A.

Preservation begins to deteriorate in this zone, and specimens of *G. margaritae* are fragmentary. Species with common to frequent occurrence include *G. menardii*, *G. venezuelana*, *Globigerina nepenthes*, *D. altispira*, *G. sacculifer*, and *Sphaeroidinellopsis* spp. Zones M14/M13 are indicated from Samples 159-960C-8H-CC (72.7 mbsf) to 10H-5, 34–36 cm (90.0 mbsf). The base of Zone M14 is identified by the first appearance of *G. margaritae*, which approximately coincides with the last appearance of *G. linguaensis*—the datum marking the base of Zone M14. The first appearance of *G. margaritae* is in Sample 159-960C-9H-2, 34–36 cm, but dissolution may have affected this datum. Subzone M13b can be identified only in Sample 159-960C-9H-3, 34–36 cm (76.1 mbsf) by the presence of *G. plesiotumida* and *G. extremus* in the absence of *G. margaritae*. Samples below this level to 159-960C-10H-5, 34–36 cm (89.5 mbsf), contain rare globorotaliids such as *G. menardii* and *G. merotumida*. *Globorotalia plesiotumida* and *G. extremus* are both absent.

A hiatus is present between Cores 159-960A-8R and 159-960A-9R (66.6 mbsf and 76.3 mbsf), and within Core 159-960C-10H (about 91.5 mbsf), so that much of the middle Miocene is inferred to be absent. The lowermost middle Miocene to lower Miocene sequence is present in Cores 159-960A-9R through 11R (76.3 through 97.6 mbsf) and spans Zones M5 to M1. Similarly, Samples 159-960C-10H-7, 34–36 cm, through 13H-3, 34–36 cm (91.5 through 114.0 mbsf), span Zones M7 to M1–M2. Sample 159-960A-9R-CC yields an assemblage of common to abundant *Globorotalia peripheroronda*, *G. archeomenardii*, and *Praeorbulina glomerosa glomerosa*, indicating lower middle Miocene Zone M5. Sample 159-960A-

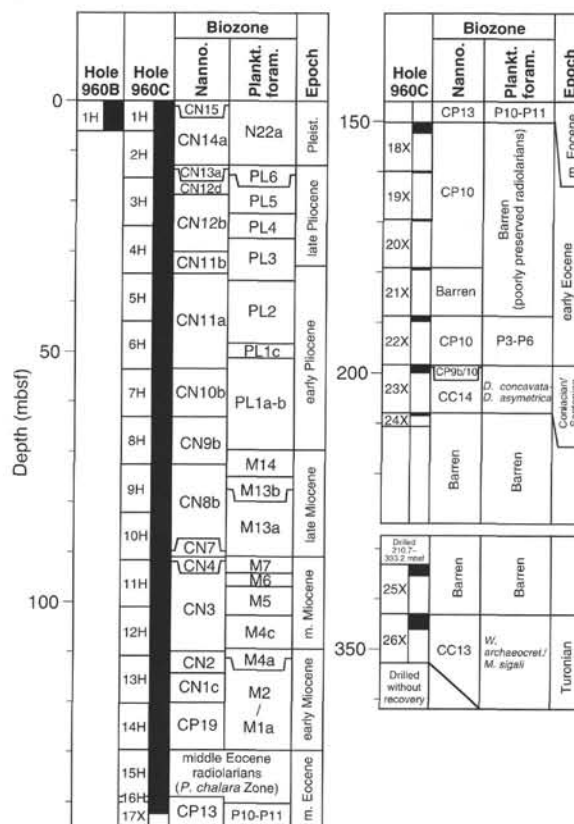


Figure 32. Biostratigraphic correlation of Holes 960B and 960C.

10R-CC contains rare *Globigerinatella insueta* and *Catapsydrax dissimilis*, indicative of Zone M3. Both *Globorotalia kugleri* (*G. kugleri mendacis*) and *G. dehiscens* are present in Sample 159-960A-11R-CC (97.6 mbsf) and identify Subzone M1a. Foraminifers are scarce in Sample 159-960A-11R-CC, but are moderately well preserved and include *G. primordius*, *G. euaperta* and *G. trilobus*. The contents of core catchers from Cores 159-960A-12R (107.3 mbsf) and 13R (116.9 mbsf) consisted exclusively of glauconite and siliceous spherules that may represent poorly preserved radiolarians.

Several samples per core were analyzed from Cores 159-960C-10H through 13H to identify the sequence of middle and lower Miocene zones. The occurrence of *Globorotalia peripheroacuta* together with *Globorotalia archeomenardii* indicates the base of Zone M7 in Sample 159-960C-10H-7, 34–36 cm (91.5 mbsf). *Orbulina suturalis* together with *G. archeomenardii*, *Globigerinoides diminutus*, *P. glomerosa glomerosa*, and *Globorotalia peripheroronda* suggests Zone M6 in Sample 159-960C-11H-3, 34–36 cm (95.1 mbsf). The first appearance of *Praeorbulina glomerosa* and *G. archeomenardii* identified Zone M5 in Samples 159-960C-11H-4, 34–36 cm, to 11H-7, 34–36 cm (96.5 to 101.1 mbsf). Associated species in Zone M5 include the common occurrence of moderately to well-preserved *G. peripheroronda*, *G. obliquus*, *G. dehiscens*, and *Globigerinoides sicanus*. Samples from 159-960C-12H-2, 34–36 cm, through 12H-3, 34–36 cm (103.1 to 104.5 mbsf), contain moderately preserved specimens of *G. sicanus* without *P. glomerosa* and indicate Subzone M4c. Samples below this level in Core 159-960C-12H contain moderately preserved foraminifers that are not age-diagnostic, but the absence of both *G. sicanus* and *Catapsydrax dissimilis*—both dissolution-resistant forms—suggests Subzone M4a or M4b. The presence of *Catapsydrax dissimilis* and *G. dehiscens*, and the apparent absence of *G.*

insueta in Samples 159-960C-12H-CC through 14H-5, 34–36 cm (110.7–138.0 mbsf) indicate a zonal assignment between Zone M2 and Subzone M1b in this interval. We have not been able to identify *G. kugleri* in this interval, perhaps because of extensive dissolution below Sample 159-960C-13H-2, 34–36 cm.

The middle Eocene has been recorded in Samples 159-960A-14R-CC (126.6 mbsf) through 16R-CC (145.6 mbsf) and in Samples from Cores 159-960C-15H through 17X (129.0–150.0 mbsf). The zonal attribution is imprecise, because the foraminifers are rare and poorly preserved. The succession of core catchers in Hole 960A contains "*Hastigerina*" *bolivariana*, *Turborotalia griffinae*, *Acarinina spinuloinflata*, *Clavigerinella eocanica*, and *C. colombiana*, the intermediate one only "*H.*" *bolivariana*, and the lowest one "*H.*" *bolivariana*, *T. griffinae*, *Acarinina* sp., and *Clavigerinella akersi*. A P11 to P10 zonal interval is probable for these three samples. Specimens of *Clavigerinella akersi*, *C. eocanica*, and *C. colombiana* are represented entirely by the tips of their digitate chambers. Chalk interbeds in Core 159-960C-17X carry a moderately to poorly preserved assemblage of *C. akersi*, *Truncorotaliodes rohri*, *Acarinina bullbrookii*, and *Subbotina inequispira* that suggests the presence of Zones P10 to P11 as low as 150 mbsf. Core catchers 159-960A-17R-CC (155.2 mbsf) to 159-960A-19R-CC (174.5 mbsf), 159-960C-20X-CC (179.0 mbsf), and 159-960C-21X-CC (188.3 mbsf) are barren of planktonic foraminifers.

In Sample 159-960C-22X-CC (207.9 mbsf), one specimen of *Parasubbotina varianta* may indicate the Paleocene (Zones P3 to P6). No other planktonic foraminifers were found, although the sample does contain rare specimens of well-preserved calcareous benthic foraminifers.

Sample 159-960A-20R-CC (164.1 mbsf) contains a species-poor assemblage of calcite-filled and recrystallized foraminifers. Species present in the assemblage include *Globotruncana* sp., *Rosita?* sp., *Rugoglobigerina?* group *rugosa*, and *Guembeltria cretacea*, all of Maastrichtian age.

Below this, samples from 159-960A-21R-CC (193.6 mbsf) through 61R-CC (451.2 mbsf) are barren of planktonic foraminifers. Limestones and calcareous sandstones in Cores 159-960A-21R to 159-960A-22R (184.1–203.4 mbsf) contain rare, very poorly preserved benthic and planktonic foraminifers that have not been identified.

Sample 159-960C-23X-CC (207.9 mbsf) contains calcite-filled and poorly preserved planktonic foraminifers of Coniacian–Santonian age. The sample consists almost entirely of fragmented and whole foraminifers, which suggests a lag deposit. Common to abundant species in this assemblage include *Dicarinella concavata*, *D. concavata-asymetrica*, *Marginotruncana sinuosa?*, *Rosita fornicata*, *Archaeoglobigerina cretacea*, *A. blowi*, and *Heterohelix* spp. (*D. concavata* to *D. asymetrica* Zones).

Sample 159-960C-26X-CC (352.8 mbsf) contains specimens of Turonian age: *Dicarinella hagni*, *Hedbergella delrioensis*, and *Heterohelix* sp. Nearly all specimens are fragmentary and partially overgrown with carbonate cement. Core catchers 159-960C-24X-CC (210.7 mbsf) and 159-960C-25X-CC (343.2 mbsf) were barren of foraminifers.

Radiolarians

Samples 159-960C-15H-CC and 16H-CC (139.2 and 140.2 mbsf) contain abundant, well-preserved radiolarians that indicate the late middle Eocene (*Podocyrtes chalara* Zone). Common species include *P. chalara*, *Lithochytris vespertilio*, *Sethochytris babylonis*, *P. trachoides*, and *Tristylispyris tricornus*. The *P. chalara* Zone was reported to be equivalent to planktonic foraminifer Zone P14 and calcareous nannofossil Subzone CP14b by Bolli et al. (1985). Poorly preserved radiolarians are present in Samples 159-960C-18X-CC through 21X-CC (159.7–188.6 mbsf) in sediments dated by calcareous nannofossils as early Eocene.

PALEOMAGNETISM

The investigation of magnetic properties at Site 960 included the measurement of the bulk susceptibility of whole-core sections and the natural remanent magnetization (NRM) of archive-half sections and discrete samples from the working-half sections. No Tensor tool orientation measurements were made at this site.

Bulk Susceptibility

Magnetic susceptibility measurements were made on whole cores from Holes 960A and 960C (Fig. 33). These data are included in Site 960 Appendix A on the CD-ROM. Poor core recovery by RCB coring in Hole 960A provides a discontinuous susceptibility record in this hole, with a significant data gap occurring between 195 and 250 mbsf. In the interval 0–20 mbsf, susceptibilities are $<10 \times 10^{-5}$ SI units. At 20 mbsf, susceptibility rises to 15×10^{-5} SI units and remains approximately constant to a depth of 50.7 mbsf, where it rises to values of up to 30×10^{-5} SI units. Susceptibility remains at values of 10 to 30×10^{-5} SI units to a depth of 71.5 mbsf, at which point values fall to $<10 \times 10^{-5}$ SI units. In the interval from 71.5 to 100.2 mbsf, susceptibility is approximately constant at 15×10^{-5} SI units. A sharp transition to susceptibilities of 50×10^{-5} SI units can be seen at 100.2 mbsf; below this, susceptibility values gradually decrease to $\sim 10 \times 10^{-5}$ SI units at 105 mbsf. This high-susceptibility interval occurs in the glauconitic sandstones and claystones of lithologic Unit II, immediately below the boundary with lithologic Unit I. In the interval from 110 to 350 mbsf, core recovery was low and the susceptibility record is incomplete. The limited measurements that exist indicate that the claystones of lithologic Unit III have susceptibilities of up to about 10×10^{-5} SI units, and that lithologic Unit IV has susceptibilities of about 0 SI units. Beneath the unconformity at 329 mbsf, bulk susceptibilities increase to values typically between 20 and 60×10^{-5} SI units, except for short intervals at depths of 348.5–349.5 and 396–398 mbsf, where susceptibility exceeds 80×10^{-5} SI units.

In Hole 960C, bulk susceptibility decreases from nearly 20×10^{-5} SI units to $\sim 10 \times 10^{-5}$ SI units in the interval from 0 to 8 mbsf. Below this depth, bulk susceptibility remains approximately constant at $\sim 10 \times 10^{-5}$ SI units to a depth of about 33 mbsf. From this depth, it gradually increases to a value of $\sim 30 \times 10^{-5}$ SI units at a depth of 90.4 mbsf. At this depth, a sharp decrease occurs in susceptibility values to $<10 \times 10^{-5}$ SI units within an interval <1 m wide. In the interval from 91 to 112 mbsf, the susceptibility remains constant, with values between 5 and 18×10^{-5} SI units. Below 112 mbsf (the transition from the nannofossil/foraminifer chalk of lithologic Unit I to the glauconitic chalk and claystones of lithologic Unit II), susceptibility gradually increases to values above 20×10^{-5} SI units, with maximum values ($>20 \times 10^{-5}$ SI units) encountered at a depth of 126 mbsf. Below 126 mbsf, susceptibility sharply decreases over a zone of <1 m thickness, followed by a sharp increase to $\sim 40 \times 10^{-5}$ SI units at about 131 mbsf. The interval from 131 to 135 mbsf has relatively high susceptibility values (around 40×10^{-5} SI units) and coincides with a significant increase in porcellanite and clay percentages in lithologic Subunit IIA. Below 135 mbsf, the susceptibility sharply decreases to $\sim 1 \times 10^{-5}$ SI units. This change occurs where the drilling process disturbed the lithified sediments and recovered fragments of rocks. Few data exist below 142 mbsf. The apparent cyclicity in the susceptibility records of Holes 959A through 959D was not observed in Holes 960A and 960C (see "Paleomagnetism" section, "Site 959" chapter, this volume).

Remanent Magnetization

Measurements of remanent magnetization were made on core sections and discrete cubes from Holes 960A and 960C. Cores 159-960C-1H through 16H were all measured using the whole-core cryo-

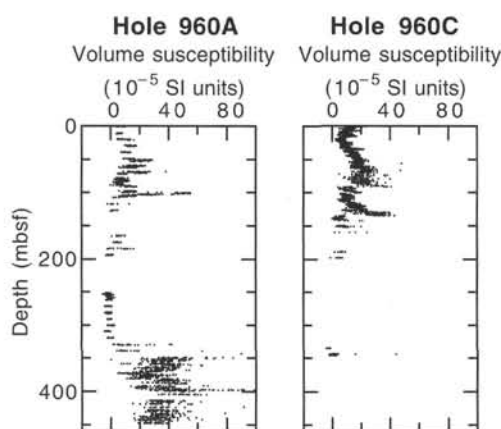


Figure 33. Bulk magnetic susceptibility vs. depth, Holes 960A and 960C.

genic (WCC) magnetometer and were demagnetized at 15 and 25 mT. NRM measurements were made on Cores 159-960C-17X through 24X and on Cores 159-960A-1R through 61R (Fig. 34). In addition, individual sections of XCB and RCB cores that appeared to be the least fragmented on visual inspection, and which possessed NRM intensities >0.5 mA/m, were measured using the WCC magnetometer and were then demagnetized to 25 mT. Fewer NRM measurements were obtained for Hole 960A compared to Hole 960C because of the lower recovery in the former hole. Below 142 mbsf in both holes, the NRM record is discontinuous and shows large data gaps. The data from both holes are archived in Site 960 Appendix B on the CD-ROM.

NRM intensity records from Holes 960A and 960C are broadly similar, although the depths of transitions are different in the two holes. In Hole 960A, the first two cores were not measured because of the intense drilling disturbance and poor recovery, so no measurements were made until Core 159-960A-3R, which yielded intensities between 1 and 5 mA/m. Intensity increases in the interval from 20 to 72 mbsf to values between 10 and 100 mA/m. Remanent intensity sharply decreases at 72 mbsf in Hole 960A. This sharp drop in the NRM intensity occurs over <1 m and corresponds to a hiatus between the upper and the lower middle Miocene (see "Biostratigraphy" section, this chapter). Between 72 and 345 mbsf, the NRM intensity is low (0.1–1 mA/m), at the practical limit of sensitivity of the WCC magnetometer. Below 345 mbsf in Hole 960A, a wide range of NRM intensities from 5 to 800 mA/m was measured. These higher intensities correspond to those sections in which quartz sandstones and silty claystones are present in lithologic Unit V.

The NRM intensity of the upper 140 m of Hole 960C shows three abrupt changes in the range of values. The NRM intensity in the upper 15 m gradually decreases from high values of ~ 10 mA/m to low values of ~ 0.1 mA/m. At a depth of 16 mbsf, the NRM intensity sharply increases to about 10 mA/m. This sharp change coincides with the transition between lithologic Subunits IA and IB. Below 15 mbsf, the NRM intensity gradually decreases to a minimum value of ~ 0.1 mA/m at 34 mbsf. Below this depth, another sharp change occurs in the NRM values: intensity jumps from 0.1 mA/m to ~ 50 mA/m over an interval of about 2 m. This sharp change does not correspond to any apparent lithologic change in lithologic Subunit IB, but it does mark a hiatus between upper and lower middle Miocene rocks. From 34 to 91 mbsf, intensity remains moderately high, with values >10 mA/m. At 91 mbsf, intensity abruptly decreases to values <0.1 mA/m. Below this depth, intensity remains low (<1 mA/m), except for high-intensity zones at 101, 111, and 117 mbsf. Between 91 and 117 mbsf, the NRM intensity record appears to comprise repetitive small cycles of decreasing and increasing intensities with depth. The high-intensity zone at 111 mbsf corresponds to the transition between

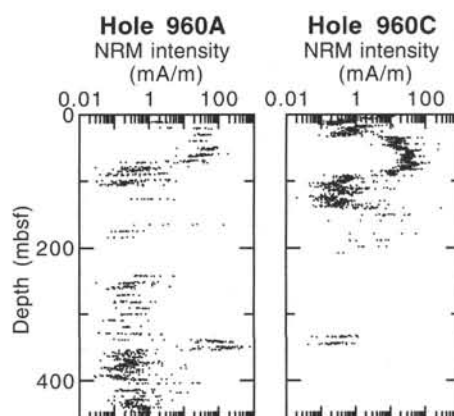


Figure 34. NRM intensity vs. depth, Holes 960A and 960C.

lithologic Units I and II. Below 126 mbsf, the NRM intensity remains moderately low, with values less than 10 mA/m. Below 140 mbsf, the data become sparse because of the poor recovery between 211 and 333 mbsf.

As at Site 959, measurements from Site 960 indicate that the rocks are either too weakly magnetized (NRM intensities <10 mA/m) to obtain the characteristic remanent direction, or they carry a strong magnetization (NRM intensities >10 mA/m) that varies systematically along the core. This latter effect probably represents a significant partial magnetic overprint induced by drilling (Fig. 35). Two characteristic patterns that occur alternately were recognized: (1) magnetization is consistently directed down the axis of the core, and (2) magnetization occurs downcore at the top and upcore at the bottom of each core. In both cases, the horizontal component is directed toward the cut face, in the archive as well as the working halves of each section (Fig. 36). This is probably the result of a radial magnetization, as recorded in Leg 154 cores (Curry, Shackleton, Richter, et al., 1995). The bimodal nature of the overprinting magnetization probably results from the alternation of two separate inner core barrels during APC coring.

The drilling-induced magnetization could not be removed by AF demagnetization to 25 mT, and no high-coercivity components could be isolated with confidence. AF demagnetization of certain intervals showed great-circle trajectories, which suggests that cleaning at higher fields may isolate a stable remanence. No reversals could be identified with confidence, and thus no magnetostratigraphic interpretation could be made.

Approximately one discrete cube sample was taken per core from Holes 960A and one per section from Hole 960C. Samples from Holes 960A and 960C that were measured for NRM on the WCC magnetometer show variations similar to the trend observed in the NRM record of the archive-half sections of both holes (Site 960 Appendix C, on the CD-ROM).

Correlation Between Holes

Three distinctive transitions in magnetic properties can be correlated between Holes 960A and 960C, and Site 959. The highest is marked by sharp increases in NRM intensity and in bulk susceptibility, which occur at 50 mbsf at Site 959, at 32 mbsf in Hole 960C, and at 20 mbsf in Hole 960A (Figs. 33 and 34). Although no lithologic change was noted at this depth in any of the holes, it does correspond to the upper/lower Pliocene boundary (planktonic foraminifer Biozones PL3/PL2). The second major boundary is a drop in intensity of magnetization and in susceptibility, which was encountered at 165 mbsf at Site 959, at 92 mbsf in Hole 960C, and at 74 mbsf in Hole 960A. At Site 960, this boundary does not have a significant litholog-

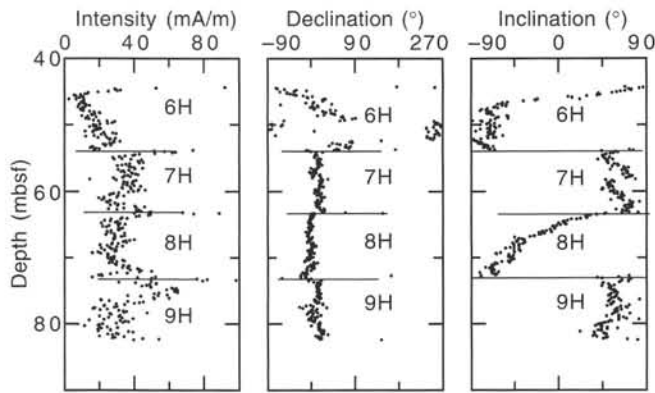


Figure 35. Example of drilling overprint in Cores 159-960C-6H to 9H, showing intensity, declination, and inclination of NRM. Cores 159-960C-6H and 8H both have a magnetization that is steeply inclined along the length of the core, whereas Cores 159-960C-7H and 9H have a magnetization that swings steeply downward at the top to steeply upward at the bottom of each core.

ic expression; nevertheless, it represents a hiatus (between planktonic foraminifer Biozones M14 and M5 in Hole 960A, and between planktonic foraminifer Biozones M13a and M7 in Hole 960C). At Site 959, the sequence is condensed and the boundary occurs in the middle of planktonic foraminifer Biozone M9. This suggests that sediments with relatively high magnetite contents were deposited from planktonic foraminifer Biozone M9 (~12 Ma) to the end of the early Pliocene (planktonic foraminifer Biozone PL3/PL2, ~4 Ma.). The third correlatable horizon is the unconformity at 1050 mbsf at Site 959 and at 329 mbsf in Hole 960A.

SEDIMENTATION RATES

Sediment accumulation rates were calculated based on preliminary biostratigraphic data from Site 960. Realistic sediment accumulation rates can be calculated only for the Neogene at Site 960 because of the discontinuous preservation of microfossils below the Neogene and the poor recovery from the Paleogene and Cretaceous sequences cored by rotary drilling. All data for the calculations were derived from Hole 960C, where APC coring provided 100% recovery of the Neogene record. The biostratigraphic datums used to calculate sediment accumulation rates are listed in Table 4.

Examination of the age vs. depth plot for the Neogene at Site 960 (Fig. 37) indicates that sediment accumulation during the early Miocene was punctuated by at least one significant hiatus, which spanned the interval from 17.4 to 18.4 Ma. This disconformity separates flat-lying upper lower Miocene sediment from the underlying, strongly dipping, early early Miocene sequence. The sample above the disconformity (Sample 159-960C-12H-6, 34–36 cm; 109.05 mbsf) contains reworked specimens of middle Eocene nannofossils (e.g., *Chiasmolithus solitus*, *Nannotetrina cristata*), indicating that older stratigraphic units were being eroded nearby during this hiatus in sediment accumulation at Site 960.

Figure 37 suggests that sediment accumulation during the early Miocene before the disconformity (23.8–18.8 Ma) was quite slow (1–8 m/m.y.). This apparent slow sediment accumulation history is, at least in part, an artifact of slumping that characterizes this underlying stratigraphic interval (see “Lithostratigraphy” section, this chapter). The strongly dipping to chaotic bedding exhibited in this sequence indicates large-scale movement of partially lithified sediments. The normal biostratigraphic sequence of biohorizons within this chaotic interval suggests several mass-movement events over a prolonged period of time (at least 5 m.y.). Similar mass-flow deposits of the

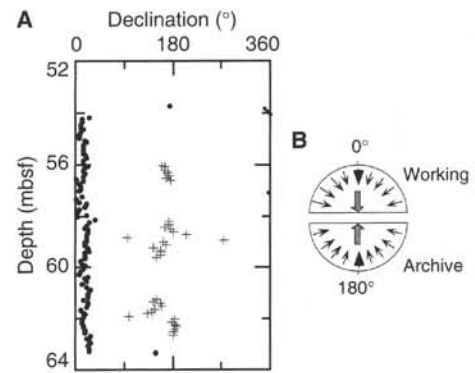


Figure 36. A. Declination of NRM for both working (plus sign) and archive (solid circle) halves of Core 159-960A-7H. B. Sketch illustrating how a radial component can produce a resultant magnetization directed toward the cut face in both the working and archive halves.

same age are known from several sites along the western Atlantic margin, where they have been designated as the Great Abaco Member (Jansa et al., 1979). Sediment accumulation rates at nearby Site 959 were higher (20 m/m.y.) for this interval and were probably more representative of sediment accumulation rates in this area during the early Miocene.

The low sediment accumulation rates (6–8 m/m.y.) of the late early Miocene continued during the early part of the middle Miocene. However, most of the middle Miocene (14.7–10.3 Ma) is absent at this site. The interval directly beneath this disconformity (as represented by Sample 159-960C-10H-7, 34–36 cm; 91.55 mbsf) contains a small component of specimens derived from the overlying upper middle Miocene (e.g., *Discoaster hamatus*, *Catinaster coalitus*). This suggests penetration by organisms burrowing into the underlying lower middle Miocene sediment.

The hiatus in sediment accumulation that characterized most of the middle Miocene continued into the early late Miocene. Sediment began to accumulate again at the site by 9.6 Ma, when a brief (1 m.y.) interval of chalk deposition and preservation began. The rate of sediment accumulation during this interval (9.6–8.6 Ma) was between 12 and 18 m/m.y. However, a distinct decrease in this overall rate occurred from 9.4 to 8.8 Ma. Calculation of a sediment accumulation rate for this interval yields an estimate of 1–5 m/m.y. It is likely that at least one additional hiatus occurred within this interval, but direct evidence of this is obfuscated by the method of calculation. The middle late Miocene was also characterized by a hiatus in sediment accumulation, spanning the interval from 8.6 to 6.5 Ma.

Sediment accumulation began again in the late late Miocene at rates of 7–10 m/m.y. Sediment accumulation accelerated in the early Pliocene to rates of 15–18 m/m.y. This rate was maintained throughout the early Pliocene, although a brief interval of lower rates may have occurred at around 5.0–4.6 Ma, as suggested by the inflection of the curve. The high pelagic sediment accumulation rate of 16–18 m/m.y. continued into the late Pliocene until 2.8 Ma, when a decrease in accumulation rates occurred. For the rest of the late Pliocene and the early Pleistocene, sediment accumulated at the reduced rate of 6–7 m/m.y. at Site 960. No upper Pleistocene sediment was recovered at Site 960.

STRUCTURAL GEOLOGY

Introduction

The structures measured at this site will be reoriented after the cruise, once the paleomagnetic and limited Formation MicroScanner (FMS) data have been fully processed. The large borehole diameter prevented the use of the FMS logging tool in Hole 960A and, owing

Table 4. Biostratigraphic datums, ages, and depths of these datums in the Neogene of Hole 960C.

Datum	Age (m.y.)	Maximum depth (mbsf)	Minimum depth (mbsf)
t <i>P. lacunosa</i>	0.46	4.68	5.68
t <i>H. sellii</i>	1.47	11.05	12.55
t <i>C. macintyreii</i>	1.60	12.55	14.05
t <i>G. fistulosus</i>	1.70	11.05	12.55
t <i>D. brouwerii</i>	1.95	14.05	15.55
reap <i>Pulleniatina</i>	2.30	15.55	15.80
t <i>G. miocenica</i>	2.30	15.55	15.80
t <i>D. pentaradiatus</i>	2.44	16.05	17.55
t <i>G. pertenuis</i>	2.60	15.80	16.05
t <i>D. surculus</i>	2.61	17.55	19.05
t <i>D. tamalis</i>	2.76	19.05	20.55
t <i>G. multicamerata</i>	3.00	22.05	23.55
t <i>G. altispira</i>	3.00	22.05	23.55
t <i>Sphaeroidinellois</i>	3.10	27.05	28.55
b <i>G. pertenuis</i>	3.50	30.05	31.55
dis <i>Pulleniatina</i>	3.50	29.70	35.05
b <i>G. miocenica</i>	3.60	30.05	31.55
t <i>Sphenolithus</i>	3.62	33.05	34.55
t <i>R. pseudoubilicis</i>	3.77	35.05	36.55
b <i>D. tamalis</i>	4.01	38.05	39.55
t <i>G. nepenthes</i>	4.30	49.05	50.55
t <i>Amaurolithus</i>	4.39	47.55	49.05
t <i>G. plesiotumida</i>	4.40	49.05	50.55
b <i>G. crassiformis</i>	4.70	50.55	52.05
b <i>C. rugosus</i>	5.04	57.05	58.55
t <i>N. acostaensis</i>	5.10	52.05	53.55
b <i>C. acutus</i>	5.34	63.55	68.05
t <i>T. rugosus</i>	5.34	63.55	68.05
t <i>D. quinqueramus</i>	5.56	68.05	69.55
b <i>G. tumida</i>	5.90	69.55	71.05
b <i>G. margaritae</i>	6.20	73.05	74.55
b <i>A. primus</i>	7.30	76.05	77.55
b <i>G. plesiotumida</i>	8.20	74.55	76.05
b <i>D. berggrenii</i>	8.40	76.05	77.55
b <i>D. loeblichii</i>	8.80	84.05	85.55
t <i>C. calyculus</i>	9.36	85.55	87.05
t <i>D. hamatus</i>	9.40	85.55	87.05
b <i>M. convallis</i>	9.40	85.55	87.05
b <i>D. neohamatus</i>	9.60	88.55	90.05
t <i>G. mayeri</i>	10.30	90.05	91.55
b <i>D. hamatus</i>	10.40	90.05	91.55
b <i>C. coalitus</i>	10.70	90.05	91.55
t <i>C. miopelagicus</i>	10.80	90.05	91.55
b <i>G. nepenthes</i>	10.80	90.05	91.55
t <i>C. nitescens</i>	12.10	90.05	91.55
t <i>S. heteromorphus</i>	13.60	90.05	91.55
t <i>G. periphroacuta</i>	14.70	90.05	91.55
t <i>P. glomerata</i>	14.80	93.55	95.05
t <i>H. ampliaptera</i>	15.80	98.05	99.55
b <i>C. premacintyreii</i>	17.40	109.05	110.55
b <i>S. heteromorphus</i>	18.10	109.05	110.55
b <i>S. belemnus</i>	18.40	109.05	110.55
b <i>S. belemnus</i>	19.70	117.05	118.55
b <i>D. druggii</i>	23.30	122.05	123.55

Note: t = top of occurrence, reap = reappearance, b = bottom of occurrence, and dis = disappearance.

to time constraints, the Tensor orientation tool was not used with the APC during recovery of the upper 16 cores of Hole 960C (Cores 159-960C-1H through 16H). Borehole bridges in Hole 960C restricted FMS coverage to the interval 173.7–354.5 mbsf (see “Downhole Measurements” section, this chapter). The RCB drilling of Hole 960A caused considerable core disturbance, resulting in rotation of individual blocks around a vertical axis within the core liner. The re-orientation of structures within Hole 960A will thus require the use of paleomagnetic data gathered from individual drilling biscuits.

Structures observed at Site 960 include bedding planes, micro-faults, veins, breccias, microfolds, and soft-sediment structures. Most tectonic features were observed in the sequence below the unconformity between lithologic Units IV and V. Veining is particularly intense below the unconformity, and mineralized faults in the siltstones of lithologic Subunit VB display evidence of strike-slip and compressional deformation.

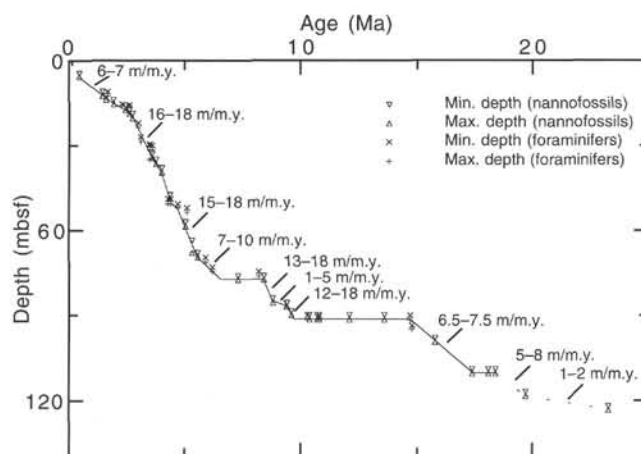


Figure 37. Distribution of biostratigraphic datums with depth in the Neogene of Hole 960C.

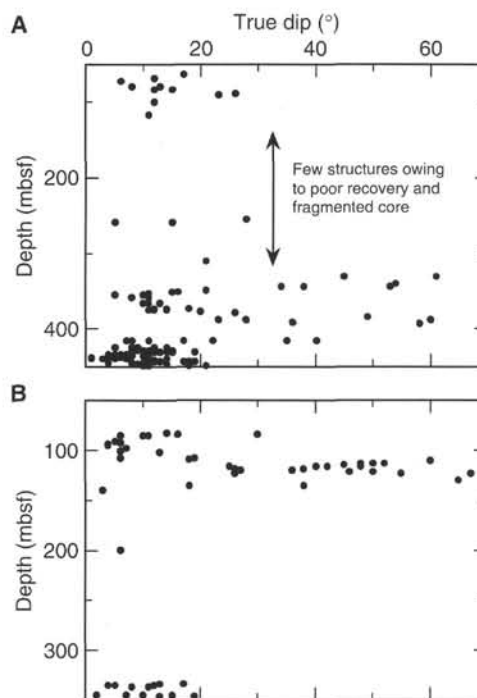


Figure 38. Variation of bedding dip with depth in (A) Hole 960A and (B) Hole 960C. Dip values are calculated from two apparent dips.

Bedding

The magnitude of the bedding dip from Hole 960A was plotted against depth (mbsf) as shown in Figure 38. Between 140 and 329 mbsf, the data are sparse owing to poor recovery and structureless/fragmented core. This interval corresponds approximately to lithologic Subunit IIB and lithologic Units III and IV, which comprise chert, palygorskite claystone, and limestone, respectively. An unconformity at 329 mbsf (Section 159-960A-37A-1) marks the abrupt transition from coarse grainstones (lithologic Subunit IVB) to laminated, quartzose sandstone (lithologic Unit V; Fig. 39). The unconformity is characterized by fissuring, veining, and brecciation. The

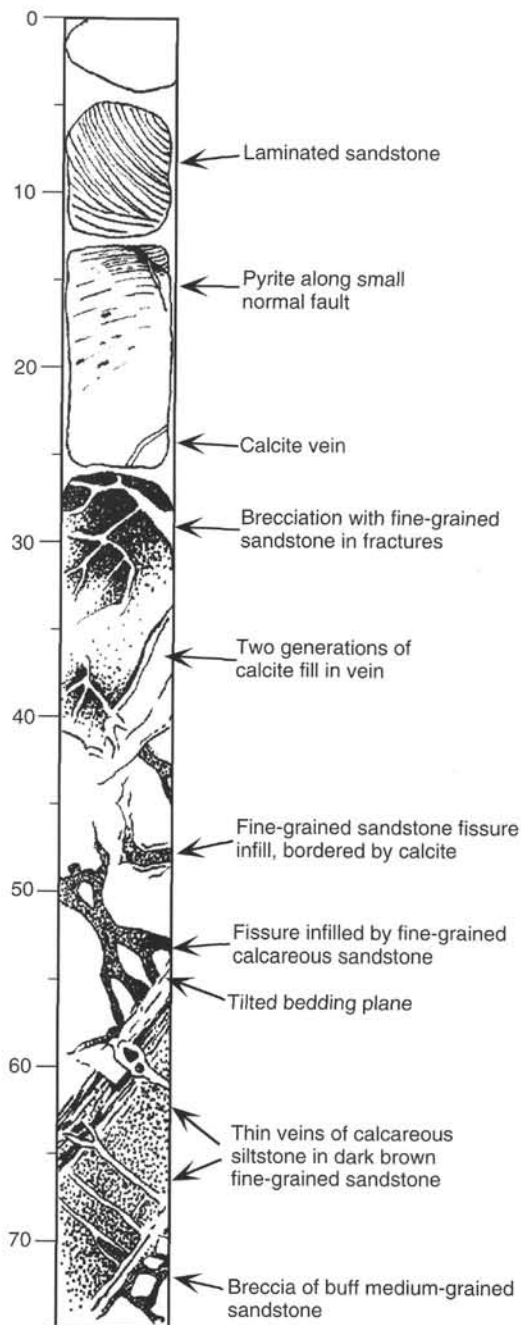


Figure 39. Sketch of the upper part of Section 159-960A-37R-2. This represents the 40–115 cm interval below the unconformity between lithologic Units IV and V.

bedding dip data collected from lithologic Unit V (329–451.2 mbsf) display a wide spectrum of values, from 5° to 60°. The steeper dips were measured directly below the unconformity (Cores 159-960A-37R and 38R) and within black claystone in Cores 159-960A-48R through 50R.

With the exception of the bedding dip values measured below the unconformity and in the black claystones of Cores 159-960A-48R through 50R, bedding dips in Hole 960A generally lie in the range of 0°–30°. Bedding planes become easier to measure and more consistent in the finely laminated sandstones and silty claystones between

Cores 159-960A-54R and 61R. The bedding dip amounts in this interval are predominantly between 0° and 20° and are generally <15°. The degree of dip does not appear to have any correlation with depth in Hole 960A. However, the lack of data from approximately 140 to 330 mbsf of Hole 960A makes the detection of any systematic trends difficult.

Bedding dips in Hole 960C display a wide range of values (Fig. 38). The first nine cores (0–82.2 mbsf) comprise soft nanofossil ooze and chalk. Laminations are visible but are too distorted by coring to be measured. Dips measured between 83 and 109 mbsf range in value from 4° to 30° but average <15°. Slumping causes an abrupt increase in dip in Section 159-960C-12H-7. Between Sections 159-960C-12H-6 and 15H-1, the dips lie between 25° and 67°. These cores are disrupted by microfaults and soft-sediment deformation. Bedding is largely defined by bedding-parallel *Zoophycos* burrows and layers rich in *Chondrites*. The beds are cut by smaller, lens-shaped burrows that appear to postdate the tilting of the beds. The interval between 210.7 and 333.2 mbsf was not cored. Grainstones of lithologic Unit IV were recovered between 333.2 and 352.8 mbsf (Cores 159-960C-25X and 26X). These rocks are equivalent to those found above the unconformity in Hole 960A. Bedding in these coarse-grained rocks is defined by silty and clayey laminations. Dips range from 2° to 10°.

Faults

In Hole 960A faulting within the nanofossil/foraminifer oozes and chalks of lithologic Unit I (0–100.1 mbsf) is characterized by minor normal faults with offsets of up to 4 cm. Recovery was poor between Cores 159-960A-14R and 28R and no structures were measured in this interval. In Hole 960C faults were observed between Cores 159-960C-10H and 15H. The sense and amount of offset of many of these faults are impossible to determine. They are generally more shallowly dipping than the faults observed in the upper levels of Hole 960A. Shallow faults in Sections 159-960C-15H-2 and 15H-3 cause slight dragging of the bedding. Faults in Sections 159-960C-15H-1 and 15H-2 bifurcate to enclose lenses of disrupted claystone.

In Hole 960A the coarse carbonate grainstones and packstones of lithologic Subunit IVB yielded few structures. The unconformity between lithologic Units IV and V is marked by intense fracturing, veining, and brecciation. A mineralized fault was observed in Section 159-960A-46R-1 where laminated brown sandstone is juxtaposed against laminated gray sandstone. The two lithofacies are separated by a calcite vein up to 2 cm wide, which contains pyrite (Fig. 40). Faults in the black claystones of lithologic Subunit VA are characterized by kaolinite veins. The kaolinite displays oriented fibers that were measured to obtain the direction of movement. Many of the faults have curved traces and look like veins on the core surfaces. The mineral lineations on the veins/faults are at oblique angles to the strike of the planes, thus providing clear evidence for a significant component of strike-slip movement.

Cores 159-960A-54R and 55R display complex microfaulting, associated with asymmetric microfolds (Fig. 41A). Small “pop-up” structures associated with asymmetric microfolds were observed in Section 159-960A-55R-1 (Fig. 41B). In this example, minor normal faults are associated with the diverging reverse faults, a characteristic feature of strike-slip faulting. Section 159-960A-54R-3 also displays excellent examples of microfaulting (Fig. 42). The fine laminations have been brittlely deformed and are slightly folded adjacent to the fault traces. Fault-related microfolds include rollover anticlines and synclinal drag folds associated with normal faults and anticlines associated with reverse faults. Section 159-960A-54R-2, 37–38 cm, displays a series of reverse microfaults that form a duplex structure. Many of the fold hinges are fractured and, in a few cases, broken. Normal faults are the predominant type. Although soft-sediment deformation features are also present within Section 159-960A-54R-3

(including water escape structures) the microfaults and folds are syn- to post-lithification tectonic features. Section 159-960A-54R-2 contains a well-preserved breccia of laminated sandstone clasts that range from 1 mm to 4 cm across (Fig. 43). Microfaults with offsets of 1 mm or less can be seen within some of the clasts.

Horizontal slickensides indicative of strike-slip faulting are not abundant but were observed in some places. In Sections 159-960A-40R-2 and 42R-1 steeply dipping fault planes (up to 75°) bear slickensides pitching 10° and 20° respectively. In the second case, the fault plane markings indicate a clear dextral motion. Section 159-960A-58R-CC contains a fault plane coated with kaolinite displaying clear strike-slip slickensides and mineral lineations. Directly below this fault there is a series of kaolinite fractures with normal offsets which displace bedding by about 1 cm. The upper terminations of the fault traces curve to become parallel with the bedding. All the kaolinite-filled faults have a similar aspect and appear to be part of the same fault generation. The fact that many display normal displacements and oblique slip slickensides may indicate fault rejuvenation in which extensional fractures were reactivated by subsequent strike-slip motion. Alternatively, the sense of movement on these faults may have been transtensional.

Veins

The lower part of the sequence (Cores 159-960A-37R through 61R) in Hole 960A is intensely veined. Kaolinite and calcite are the most common vein-filling minerals. Kaolinite predominates in the dark claystones and siltstones of lithologic Unit V (within both Sub-units VA and VB).

Calcite occurs as several different varieties. Clear gray calcite forms veins with sharp boundaries, whereas opaque white calcite forms more diffuse zones consisting of two generations of vein fill. The opaque veins contain a central seam of sparry calcite and are bordered by a region, 3–4 mm wide, of calcite recrystallization. The two types of veins are best observed in Section 159-960A-34R-1, where veins of the two types converge to become parallel, in a single loose block of coarse-grained grainstone. Opaque calcite forms irregular, diffuse patches in Section 159-960A-35R-1. Sparry gray calcite occurs in sharply defined veins, which are commonly sinuous. Intense calcite mineralization occurs in Core 159-960A-37R, directly beneath the unconformity between lithologic Units IV and V. The 1-m interval below the unconformity is characterized by steeply dipping, brecciated bedding planes. Fissures trending approximately perpendicular to the bedding planes are infilled with calcite-cemented quartz siltstone and fine-grained sandstone (Fig. 39). Veins of calcite in this interval show two generations of vein fill.

Pyrite is closely associated with calcite in Cores 159-960A-37R and 38R. In Section 159-960A-37R-2, pyrite and calcite occur together in veins up to 1 mm wide and are found along a minor normal fault. In thin section, the pyrite forms a sharply defined, discontinuous vein, 0.5 mm thick, along the fault trace. The fault itself is marked by a seam of calcite-cemented, angular quartz grains. Pyrite also forms thin seams (0.5 mm wide) and diffuse clusters within the sandstone. Calcite and pyrite give way to kaolinite veins in the dark silty claystones of Cores 159-960A-40R through 45R. The veins are generally thin and display sigmoidal and en échelon patterns. Kaolinite tension gashes are common features in Core 159-960A-44R. Core 159-960A-45R contains abundant wispy kaolinite veins and rare veins of barite. Pyrite is also common in this core, occurring as a fracture infill and as disseminated cubes within the sediment. In Section 159-960A-45R-CC kaolinite rims clasts in a breccia of fine-grained sandstone. The breccia is cut by an irregular vein of translucent gray calcite. In thin section it can be seen that the calcite crystals are oriented at approximately 30° to the vein walls, possibly because of shearing. The vein dies out into a thin seam of pyrite. Calcite, pyrite, and kaolinite veins are common in Section 159-960A-46R-1. Pyrite

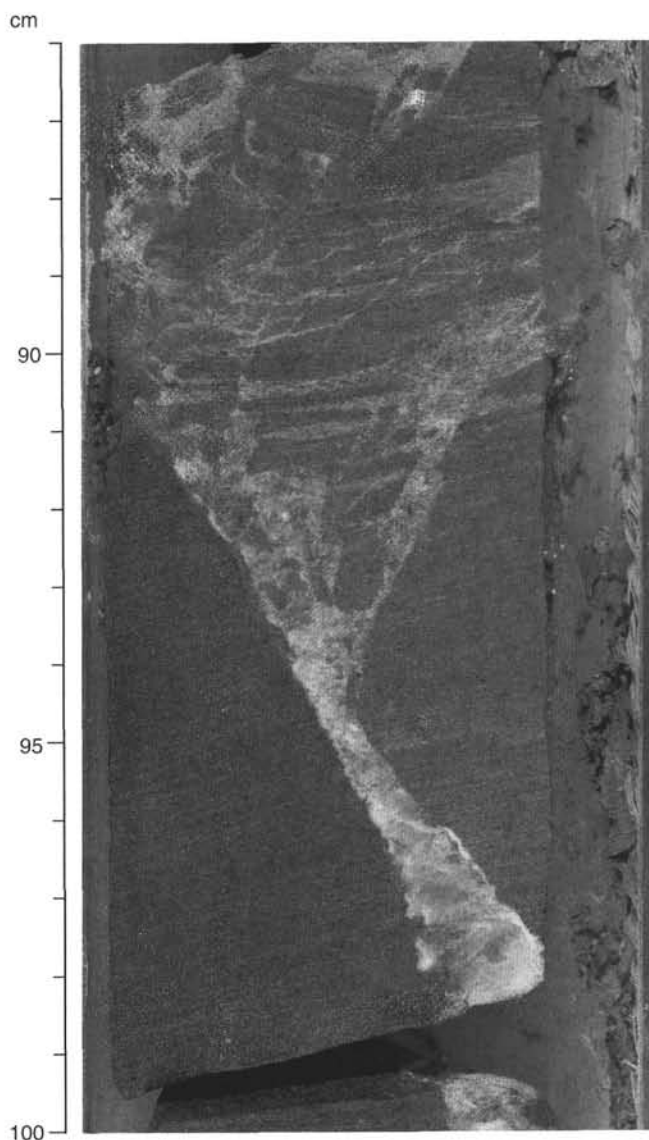


Figure 40. Fault juxtaposing two blocks of laminated sandstone in Section 159-960A-46R-1, 86–100 cm. The hanging wall is highly brecciated and the fault is infilled with calcite and minor pyrite.

forms diffuse haloes around calcite veins. Calcite forms a thick vein, which appears to mark the site of a fault between gray, laminated sandstone and brecciated brown sandstone. Kaolinite forms a rim at the edge of the calcite. In the cores below this level, kaolinite is common along fault planes and displays well-formed mineral lineations parallel to the direction of movement.

Large, well-formed crystals (up to 1 cm in diameter) of clear quartz occur as a crust on an exposed vein surface in sandstone in Section 159-960A-61R-1.

Soft-sediment Deformation

Soft-sediment deformation observed at Site 960 was predominantly in the siltstones, claystones, and sandstones of lithologic Unit V. A water escape structure 1.5 cm wide (Fig. 44) and convolute bedding were observed in Section 159-960A-46R-1 in a 4-cm-thick sandstone bed. A slump fold was observed in laminated claystone in

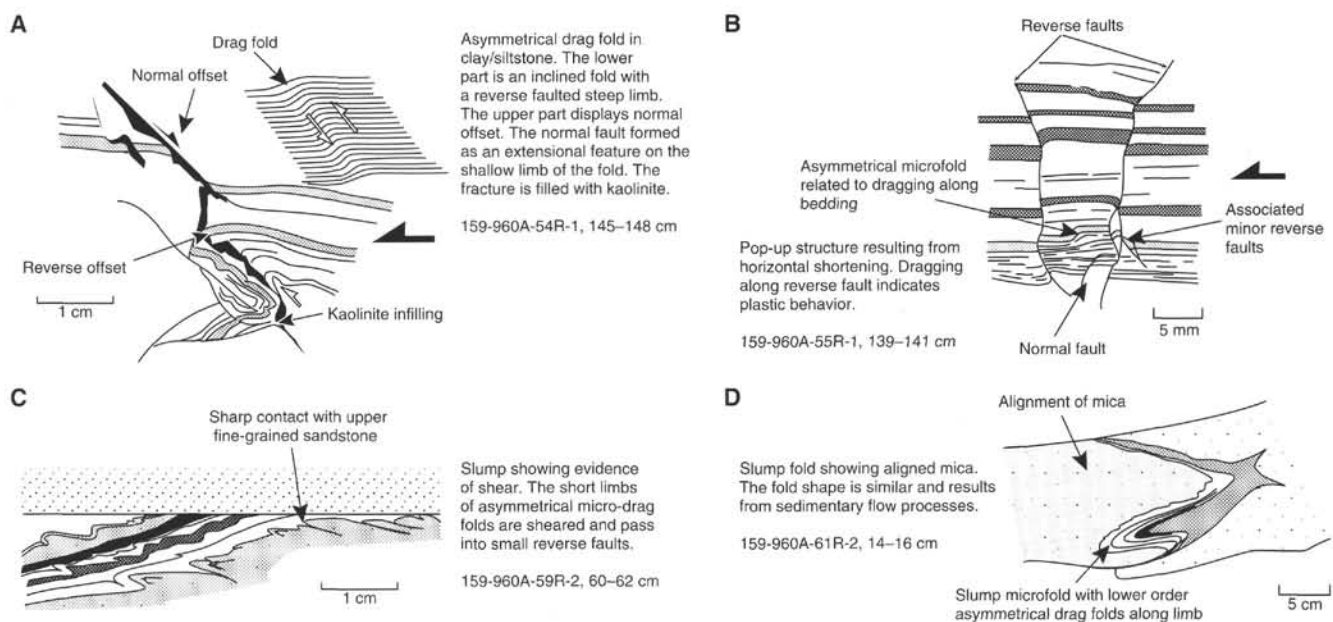


Figure 41. Examples of deformation in lithologic Unit V. **A.** Asymmetric fold with associated reverse fault filled with kaolinite. **B.** Pop-up structure with asymmetric drag fold. **C.** Sheared slump. **D.** Slump fold with aligned micas along its axial plane.

Section 159-960A-44R-2. In Section 159-960A-59R-1, well-preserved convolute bedding and cross-laminations were observed. Load structures are particularly common at the base of sandstone beds and range from irregular bedding surfaces to fully detached load casts. The soft-sediment features observed in Hole 960A were generated largely by sedimentary processes such as dewatering and loading. These can be explained in terms of the instability of the intercalated layers of unlithified sandstone and siltstone. Tectonic activity, however, may have played a role in the generation of the slumping.

In Hole 960C, intense slumping is observed in Cores 159-960C-13H through 15H. In Section 159-960C-15H-4, a distinct, sharply defined boundary marks the base of a slumped unit. The slumped unit consists of green, bioturbated claystone with steeply dipping bedding and folded, sheared burrows. The disrupted unit overlies a streaky, brown-green claystone, which may record soft-sediment shear at the base of the slump.

Discussion

Structural data from Site 960 cannot yet be described in geographic coordinates and, hence, we currently have no constraint on the true orientations of structures. Nevertheless, it is possible to make several initial interpretations regarding the nature and relative timing of tectonic events. The intense brecciation and fissuring of the sandstones below the unconformity between lithologic Units IV and V (Section 159-960A-37R-1) may reflect a phase of uplift and erosion. The steep dips of the beds directly underlying the unconformity (e.g., Section 159-960A-37R-2) may indicate a subsequent phase of localized tilting. The fact that the fissures are perpendicular to the bedding implies that they were formed before the tilting. Steeply dipping beds were not observed throughout the rest of lithologic Unit V. The fissure infills of calcite-cemented quartz sandstone may herald the onset of carbonate deposition in a shallow-water environment. The establishment of a proximal carbonate platform is recorded in Section 159-960A-37R-1 with the abrupt transition to coarse carbonate grainstones.

Most of the veining and faulting observed at Site 960 occurs below the unconformity (i.e., in lithologic Unit V), although normal faults do occur throughout the sequence. The age of lithologic Unit V is unknown but is probably pre-Turonian, based on the Turonian to Coniacian age of the overlying carbonates. The complex microfaulting observed in Cores 159-960A-54R to 159-960A-61R displays both normal and reverse senses of motion. The close association of normal and reverse faults may be interpreted in two ways:

1. Both normal and reverse faults may result from asymmetric microfolding developed by shear. Reverse faulting cutting across the steep limb is caused by continued shearing. The associated normal faults are caused by extension in the shallow limb.
2. The close association of normal and reverse faults is also a characteristic of flower structures in strike-slip zones. Other evidence for strike-slip is also clearly observed in Hole 960A (e.g., Sections 159-960A-40R-2, 42R-1, and 58R-CC) where kaolinite along fault planes displays mineral lineations at a high angle to the dip. Strike-slip faults were not observed above the unconformity.

The appearance of quartz in Section 159-960A-61R-1 (i.e., the deepest core of Hole 960A) may reflect the presence of hydrothermal fluids, possibly related to passage of the spreading ridge past the Marginal Ridge.

ORGANIC GEOCHEMISTRY

Introduction

At Site 960, real-time monitoring of volatile hydrocarbons, determination of inorganic carbon, total carbon, total nitrogen, and Rock-Eval measurements were performed ("Explanatory Notes" chapter, this volume). Results on volatile hydrocarbons are discussed in "Source Rock Geochemistry" section (this chapter).

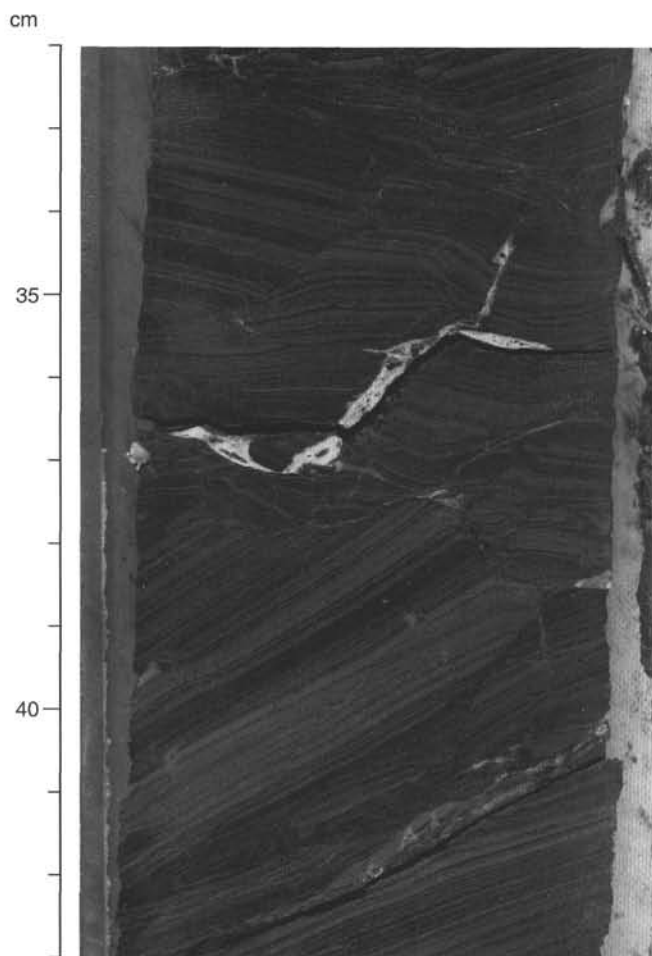


Figure 42. Microfaulting and associated folding in Section 159-960A-54R-3, 32–43 cm.

Carbonate and Organic Carbon Records

Inorganic carbon, organic carbon, and total nitrogen contents were measured in 132 samples. Sampling focused on APC cores recovered from Hole 960C. Sampling frequency ranged from one sample per section in the upper 70 mbsf (Cores 159-960C-1H through 8H) to three samples per core in lower parts of Hole 960C (Cores 159-960C-9H through 26X). This frequency was reduced in Hole 960A because of lower sediment recovery. The results of elemental analysis are summarized in Table 5 and are presented in Figures 45 and 46.

To facilitate correlation of organic geochemical results obtained at Site 960 with results of the adjacent Site 959, subdivisions defined at Site 959 (intervals A to I) were adapted for Site 960 (a detailed description of different intervals is given in the “Organic Geochemistry” section, “Site 959” chapter, this volume). Discussion of the upper 150 mbsf of the sediment column is based on Hole 960C (Fig. 45); deeper sections (100–450 mbsf) refer to Hole 960A (Fig. 46). Based on the organic carbon and carbonate carbon record, the sedimentary sequences from Holes 960A and 960C are divided into five intervals (A, B/C, D/E, H, and I).

Early Pliocene through Pleistocene nannofossil/foraminifer oozes of interval A (0–19 mbsf) show large amplitude fluctuations in carbonate similar to sediments from Site 959 but with slightly higher contents (33–52 wt%; Fig. 45). In contrast, the amount of organic car-



Figure 43. Breccia of laminated sandstone clasts in Section 159-960A-54R-2, 1–7 cm.

bon in Hole 960C is less variable and, in absolute terms, is lower compared with Site 959, except for two spikes in organic carbon (1.2 wt%) at the base of interval A (Sections 159-960-2H-6 and 3H-2). These pronounced shifts in carbonate and organic carbon are probably related to late Quaternary glacial-interglacial cycles.

Below interval A early Miocene to late Pliocene age nannofossil-foraminifer oozes and chalks (see “Lithostratigraphy” section, this chapter) comprise interval B/C (19–115 mbsf; Fig. 45). It was not possible to distinguish these two intervals as recognized at Site 959 because of the condensed sediment sequence in Hole 960C. Deposits from Hole 960C show persistent intermediate to high carbonate contents (45–55 wt%) with a few minor fluctuations, including slightly reduced contents toward the base. Average carbonate contents of interval B/C at Hole 960C exceed the corresponding amount of carbonate at Site 959 by approximately 10 wt%, which may suggest either reduced terrestrial dilution or less extensive carbonate dissolution at Site 960 during middle Miocene to late Pliocene time. Organic carbon in interval B/C gradually decreases with depth from 0.7 wt% at the top to 0.2 wt% at the base indicating effective diagenesis of labile organic matter. Average organic carbon content, however, is lower compared to Site 959 deposits, especially in lower Pliocene sections. Organic matter degradation rates appear to be lower at Site 960. The rather monotonous carbon records are interrupted by one pronounced peak in TOC (5.66 wt%; Section 159-960C-8H-6) at the Miocene/Pliocene boundary (70 mbsf). A corresponding pronounced decrease in carbonate is preliminarily interpreted as evidence of extensive corrosion of carbonate during time of deposition, due to greatly intensified organic carbon degradation.

Sediments of interval D were recovered in the lower APC cores of Hole 960C (115–140 mbsf; Fig. 45). Intervals D and E were found in rotary cores of Hole 960A (100–180 mbsf; Fig. 46). As a result of the low sampling frequency in Hole 960A, intervals D and E were not differentiated from one another and only reflect large-scale trends in the carbon signal. Distinct and inversely correlated shifts in carbonate and organic carbon represent glauconitic, diatom-radiolarian nannofossil-micrite chalk and claystones of early Eocene through early Miocene age (lithologic Subunit IIA). Carbonate reaches its highest content of almost 50 wt% in chalky lithologies, whereas peaks in organic carbon (up to 6.4 wt%; Section 159-960A-15R-1) are commonly associated to claystones. Continuously low carbonate contents and in-

intermediate organic carbon content between 150 and 180 mbsf in Hole 960A (Fig. 46) likely represent deposits of interval E at Site 959.

A pronounced increase in carbonate, marking the onset of interval H (180–335 mbsf), corresponds to the transition in lithologies from glauconitic claystones and micritic chalks of Santonian and Coniacian age (lithologic Subunit IVA) to underlying limestones of non-specified Cretaceous age (Fig. 46). Carbonate content persists at very high levels (86–97 wt%) throughout the interval, and a minor increase with depth is recognized. Organic carbon is almost absent in interval H. A very similar geochemical pattern in limestones was encountered in the lowermost section of Site 959 (1040–1085 mbsf; see “Organic Geochemistry” and “Lithostratigraphy” sections of “Site 959” chapter, this volume), suggesting a correlation between limestone units at the two sites.

The lowermost section of Hole 960A (interval I; 335–451.2 mbsf, Fig. 46) comprises Cretaceous micritic and silty sandstones, sideritic siltstones, and claystones. Carbonate values in general are very low except for two layers at 368 and 392 mbsf (Sections 159-960A-44R-2 and 50R-3) where intermediate contents were measured (19–30 wt%). Organic carbon contents show large amplitude variations ranging from 0.2 to 2.1 wt%. A clear correlation of high organic carbon content to more clayey deposits was not always encountered. Interval I probably corresponds to the basal sedimentary lithologic Unit V, where similar carbon records occur (see “Organic Geochemistry” and “Lithostratigraphy” sections, “Site 959” chapter, this volume).

Composition of Organic Matter

The type of sedimentary organic matter (OM) in Holes 960A and 960C was characterized using organic carbon:total nitrogen ratios (C/N) and Rock-Eval pyrolysis data (hydrogen index and T_{max}). Application of C/N ratios and hydrogen indices for qualitative evaluation of the relative proportions of marine and terrigenous organic matter, and determination of the thermal maturity level based on T_{max} values of sedimentary organic matter, are discussed in the “Organic Geochemistry” section of the “Site 959” and “Explanatory Notes” chapters (this volume). Results are summarized in Tables 5 and 6, and are presented in Figures 45 and 46.

Late Pliocene to Pleistocene changes in organic matter deposition mainly were controlled by fluctuations in terrestrial supply, as indicated by elevated C/N ratios (10–15, interval A; Fig. 45) and low hydrogen index (HI) values between 50–85 mgHC/gTOC (Fig. 47; Table 6). Slightly higher C/N ratios compared to corresponding Site 959 deposits may suggest higher proportions of terrestrial organic matter. This interpretation is further supported by results from smear slide analysis; up to 5 vol% plant fragments are reported. Amorphous organic matter (AOM) of probable marine sources, in contrast, was not described in Pliocene to Pleistocene sediment from Site 960 (see “Lithostratigraphy” section, this chapter). The organic matter is at a thermally immature level ($T_{max} = 386^{\circ}$ – 401° C).

Intermediate to low organic carbon contents in interval B/C (19–115 mbsf) have no major effect on C/N ratios of these deposits, except for the Miocene/Pliocene depositional event (Fig. 45). C/N ratios scatter around 6–10 down to the Miocene/Pliocene boundary. Below this level, a simultaneous drop in organic carbon and C/N ratios to low values between 4 and 7 is evident. Use of C/N ratios as indicators for the organic matter source therefore does not seem appropriate (see methodologic discussion in the “Organic Geochemistry” section of the “Site 959” chapter, this volume). However, minor proportions of terrestrial organic matter are described in smear slides obtained from this sediment section (traces to 5 vol% plant debris; see “Lithostratigraphy” section, this chapter). Deposition of large quantities of terrestrial organic matter, probably oxidized, at the Miocene/Pliocene boundary, is demonstrated by an anomalously high C/N ratio (165) and a minimum HI of 2 mgHC/gTOC (Figs. 45, 47). The T_{max} value of this TOC-rich deposit indicates a stage of low thermal maturity (417° C). Interestingly, a comparably pronounced or-

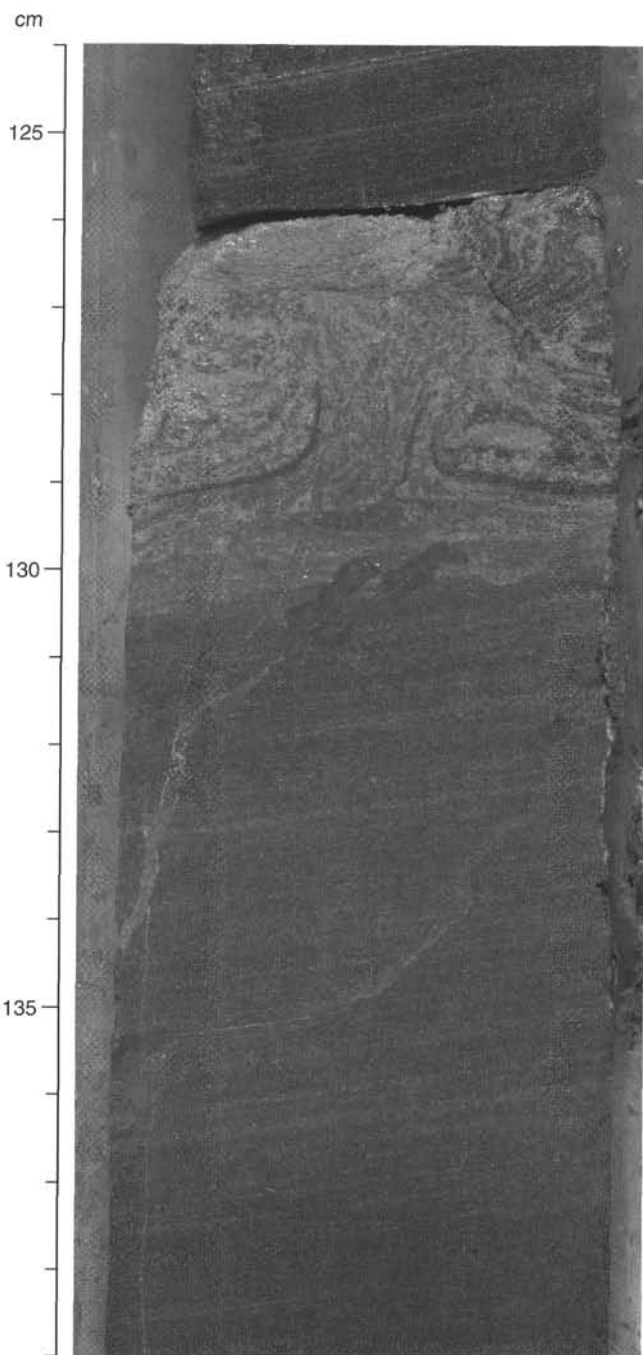


Figure 44. Water escape structure in fine-grained sandstone (Section 159-960A-46R-1, 124–139 cm).

ganic geochemical signal is not recorded in corresponding Site 959 deposits at the Miocene/Pliocene boundary.

Early Eocene to early Miocene chalk and claystones (interval D/E; 115–150 mbsf in Hole 960C and 100–180 mbsf in Hole 960A; Figs. 45, 46) display similar organic carbon, C/N ratio, HI, and T_{max} records as corresponding diatomite/nannofossil chalk units at Site 959 (see “Organic Geochemistry” section of the “Site 959” chapter, this volume). Organic carbon-rich deposits are characterized by elevated C/N ratios (13–17) and intermediate to high HI values (140–380 mgHC/gTOC), suggesting deposition of mixed marine and terrestrial organic matter. Smear slide analyses support the organic

Table 5. Summary of elemental analysis of sediments at Site 960.

Core, section, interval (cm)	Depth (mbsf)	Inorg-C (wt%)	CaCO ₃ (wt%)	Tot-C (wt%)	Org-C (wt%)	TN (wt%)	C/N	Core, section, interval (cm)	Depth (mbsf)	Inorg-C (wt%)	CaCO ₃ (wt%)	Tot-C (wt%)	Org-C (wt%)	TN (wt%)	C/N
159-960A-															
1R-1, 10-11	0.10	5.38	44.8					3H-1, 117-118	16.88	5.22	43.5	6.04	0.82	0.09	9.3
3R-1, 33-34	10.93	5.69	47.4	6.14	0.45	0.05	8.2	3H-2, 110-111	18.31	5.55	46.2	6.72	1.17	0.08	14.0
4R-1, 59-60	20.49	5.21	43.4	5.52	0.31	0.05	6.6	3H-3, 91-92	19.62	6.67	55.6	7.32	0.65	0.07	9.1
5R-1, 122-123	30.82	6.28	52.3	6.66	0.38	0.05	8.1	3H-4, 110-111	21.31	6.37	53.1	6.74	0.37	0.05	7.3
8R-1, 94-95	59.84	5.81	48.4	5.85	0.04	0.02	1.7	3H-5, 51-52	22.22	6.32	52.6	6.69	0.37	0.06	6.4
8R-3, 65-66	62.55	5.92	49.3	6.07	0.15	0.03	4.8	3H-6, 110-111	24.31	5.85	48.7	6.50	0.65	0.07	9.4
9R-1, 97-98	70.57	5.71	47.6	5.72	0.01	0.02	0.4	4H-1, 147-148	26.68	5.76	48.0	6.26	0.50	0.05	9.2
9R-3, 79-80	72.39	5.41	45.1	5.57	0.16	0.03	5.1	4H-2, 110-111	27.81	6.20	51.6	6.93	0.73	0.07	10.6
10R-1, 126-127	79.56	4.24	35.3	4.29	0.05	0.02	2.1	4H-3, 114-115	29.35	5.28	44.0	5.81	0.53	0.06	8.8
10R-3, 48-49	81.78	3.86	32.2	4.22	0.36	0.09	4.2	4H-4, 109-110	30.80	6.46	53.8	6.96	0.50	0.05	9.3
10R-5, 53-54	83.73	4.61	38.4	4.88	0.27	0.03	8.7	4H-5, 112-113	32.33	7.01	58.4	7.48	0.47	0.05	8.8
10R-5, 116-117	84.36	5.55	46.2	6.26	0.71	0.06	11.4	4H-6, 110-111	33.81	5.99	49.9	6.36	0.37	0.05	7.1
11R-1, 57-58	88.57	3.87	32.2	4.02	0.15	0.03	4.8	5H-1, 113-114	35.84	5.40	45.0	5.82	0.42	0.05	8.3
11R-3, 17-18	91.17	1.48	12.3	1.93	0.45	0.05	9.6	5H-2, 110-111	37.31	5.56	46.3	6.07	0.51	0.05	9.5
12R-1, 109-110	98.69	1.94	16.2	2.12	0.18	0.04	4.6	5H-3, 114-115	38.85	6.23	51.9	6.66	0.43	0.05	8.3
12R-3, 135-136	101.95	0.07	0.6	0.99	0.92	0.11	8.4	5H-5, 129-130	42.00	6.18	51.5	6.60	0.42	0.05	8.6
12R-5, 109-110	104.69	0.08	0.7	2.81	2.73	0.17	15.9	5H-6, 110-111	43.31	6.37	53.1	6.66	0.29	0.05	6.4
13R-1, 36-37	107.66	0.07	0.6	3.33	3.26	0.20	16.1	6H-1, 115-116	45.36	6.45	53.7	6.97	0.52	0.05	10.1
14R-1, 11-12	117.01	4.24	35.3	4.69	0.45	0.05	9.6	6H-2, 110-111	46.81	5.65	47.1	6.04	0.39	0.04	8.9
15R-1, 66-67	127.56	0.22	1.8	6.66	6.44	0.38	16.8	6H-3, 115-116	48.36	5.83	48.6	6.21	0.38	0.05	7.6
19R-1, 19-20	164.99	0.06	0.5	0.80	0.74	0.06	11.9	6H-4, 110-111	49.81	5.33	44.4	5.59	0.26	0.05	5.7
22R-1, 104-105	194.84	10.33	86.0					6H-5, 115-116	51.36	6.30	52.5	6.69	0.39	0.05	8.1
25R-1, 32-34	223.02	10.49	87.4					6H-6, 110-111	52.81	5.82	48.5	6.21	0.39	0.04	9.3
28R-1, 100-102	252.70	10.99	91.5					7H-1, 114-115	54.85	6.67	55.6	6.66	0.60	0.04	0.0
29R-1, 7-8	256.47	9.76	81.3					7H-2, 110-111	56.31	5.96	49.6	6.37	0.41	0.04	9.1
29R-3, 128-129	259.85	10.33	86.0					7H-3, 110-111	57.81	6.98	58.1	7.28	0.30	0.03	9.2
30R-1, 50-52	261.90	10.92	91.0					7H-4, 110-111	59.31	5.87	48.9	6.28	0.41	0.04	9.2
31R-1, 16-18	271.26	11.20	93.3					7H-5, 109-110	60.80	5.35	44.6	5.84	0.49	0.05	9.6
32R-1, 13-15	280.83	11.19	93.2					7H-6, 110-111	62.31	5.60	46.6	5.92	0.32	0.04	8.8
33R-1, 30-32	290.60	11.79	98.2					8H-1, 113-114	64.34	5.45	45.4	5.60	0.15	0.03	5.3
34R-1, 28-30	299.88	11.63	96.9					8H-2, 110-111	65.81	4.39	36.6	4.79	0.40	0.04	9.7
35R-1, 58-60	309.78	11.58	96.5					8H-3, 110-111	67.31	4.48	37.3	4.90	0.42	0.04	9.7
36R-1, 93-95	319.83	11.54	96.1					8H-4, 110-111	68.81	5.01	41.7	5.25	0.24	0.03	6.8
37R-1, 31-33	328.81	10.89	90.7					8H-5, 110-111	70.31	4.51	37.6	4.91	0.40	0.04	9.8
37R-2, 139-141	330.36	3.97	33.1	4.07	0.10	0.03	3.2	8H-6, 110-111	71.81	0.03	0.2	5.69	5.66	0.03	165.7
44R-1, 7-8	367.27	0.53	4.4	1.87	1.34	0.16	8.2	9H-1, 109-110	73.80	6.34	52.8	6.70	0.36	0.04	9.3
44R-2, 101-103	368.21	3.62	30.2	3.83	0.21	0.03	6.7	9H-3, 113-114	76.84	6.54	54.5	6.82	0.28	0.03	9.0
45R-1, 127-129	368.47	1.27	10.6	2.63	1.36	0.13	10.3	9H-5, 114-115	79.85	5.28	44.0	5.58	0.30	0.03	8.7
45R-2, 86-87	368.06	1.16	9.7	2.26	1.10	0.12	9.4	10H-1, 110-111	83.31	4.48	37.3	4.69	0.21	0.03	6.4
46R-1, 147-149	373.27	1.42	11.8	2.02	0.60	0.02	25.6	10H-3, 109-110	86.30	5.67	47.2	5.82	0.15	0.03	4.7
46R-2, 127-129	373.07	1.07	8.9	1.88	0.81	0.07	11.5	10H-5, 110-111	89.31	5.13	42.7	5.13	0.00	0.02	0.1
46R-3, 1-2	371.81	0.84	7.0	1.61	0.77	0.12	6.6	11H-1, 130-131	93.01	6.14	51.1	6.39	0.25	0.03	7.4
50R-1, 15-17	391.25	0.57	4.7	2.72				11H-3, 115-116	95.86	6.47	53.9	6.60	0.13	0.03	4.3
50R-1, 16-17	391.26	0.46	3.8	2.56	2.10	0.16	13.5	11H-5, 126-127	98.97	4.23	35.2	4.37	0.14	0.03	3.9
50R-3, 134-135	392.44	2.22	18.5	2.84	0.62	0.15	4.2	12H-1, 45-46	101.66	4.85	40.4	5.08	0.23	0.03	7.5
52R-1, 141-143	398.71	0.62	5.2	2.10	1.48	0.15	10.1	12H-3, 55-56	104.76	3.75	31.2	4.05	0.30	0.04	7.0
52R-2, 142-143	398.72	0.19	1.6	1.83	1.64	0.14	11.9	12H-5, 112-113	108.33	3.43	28.6	3.63	0.20	0.04	5.5
53R-1, 19-21	403.49	0.24	2.0	1.15	0.91	0.13	7.2	13H-1, 122-123	111.93	3.25	27.1	3.45	0.20	0.04	5.7
54R-2, 88-90	415.48	0.39	3.2	1.79	1.40	0.16	8.8	13H-3, 134-135	115.05	2.97	24.7	3.15	0.18	0.04	4.8
55R-1, 13-15	417.93	0.40	3.3	1.50	1.10	0.17	6.4	13H-5, 149-150	118.20	4.81	40.1	5.01	0.20	0.03	6.0
57R-3, 15-17	430.20	0.06	0.5	0.68	0.62	0.18	3.4	14H-1, 93-94	121.14	1.25	10.4	1.46	0.21	0.04	5.0
58R-2, 23-25	434.05	0.18	1.5	1.18	1.00	0.17	6.0	14H-3, 124-125	124.45	0.88	7.3	1.33	0.45	0.10	4.4
59R-1, 36-37	437.36	0.22	1.8	0.88	0.66	0.20	3.4	14H-5, 49-50	126.70	5.88	49.0	6.27	0.39	0.04	10.2
59R-1, 76-78	437.76	0.18	1.5	1.47	1.29	0.23	5.7	15H-1, 126-127	130.97	0.05	0.4	0.54	0.49	0.06	8.3
60R-2, 7-8	443.40	0.47	3.9	1.29	0.82	0.03	30.1	15H-3, 108-109	133.79	0.03	0.2	0.79	0.76	0.12	6.6
61R-1, 78-79	446.98	0.65	5.4	1.46	0.81	0.02	35.8	15H-5, 134-135	137.05	0.05	0.4	1.83	1.78	0.13	13.4
159-960C-															
1H-1, 123-124	1.24	4.56	38.0	5.55	0.99	0.09	10.6	17X-1, 142-143	141.63	4.33	36.1	5.18	0.85	0.08	10.7
1H-2, 123-124	2.74	6.11	50.9	7.06	0.95	0.08	11.9	17X-CC, 34-35	176.93	5.25	43.7	2.72	0.00	0.14	0.0
1H-3, 135-136	4.36	5.78	48.1	6.68	0.90	0.07	13.1	21X-CC, 26-27	206.00	0.02	0.2	0.58	0.56	0.05	12.1
1H-4, 42-43	4.93	5.05	42.1	6.06	1.01	0.08	13.1	22X-1, 20-21	188.81	0.05	0.4	0.40	0.35	0.05	7.7
1H-5, 35-36	6.36	5.54	46.1	6.40	0.86	0.07	11.8	23X-1, 28-29	198.59	0.36	3.0				
2H-1, 109-110	7.30	3.96	33.0	4.86	0.90	0.07	13.4	25X-1, 78-80	333.99	11.30	94.1	11.30	0.00	0.00	
2H-2, 110-111	8.81	6.19	51.6	7.11	0.92	0.06	15.1	25X-2, 35-37	336.56	11.20	93.3	11.29	0.09	0.00	
2H-3, 111-112	10.32	3.93	32.7	4.83	0.90	0.08	11.2	26X-2, 66-67	346.87	3.99	33.2	10.09	6.10	0.12	52.3
2H-4, 112-113	11.83	6.26	52.1	7.14	0.88	0.07	12.5	26X-CC, 6-7	352.97	7.52	62.6	9.14	1.62	0.21	7.6
2H-5, 125-126	13.46	5.80	48.3	6.59	0.79	0.07	11.4								
2H-6, 112-116	14.84	3.44	28.7	4.64	1.20	0.10	12.1								

Note: Inorg-C = inorganic carbon, CaCO₃ = carbonate, Tot-C = total carbon, Org-C = total organic carbon, TN = total nitrogen, and C/N = organic carbon/total nitrogen ratios.

geochemical results; 1-5 vol% amorphous organic matter of probable marine origin are reported (see "Lithostratigraphy" section, this chapter). Organic matter in interval D/E is at an immature to low-maturity level, as demonstrated by T_{max} values between 403° and 429°C (Fig. 47).

Limestones of interval H (180-335 mbsf) are almost devoid of organic carbon.

The sandstone and siltstone interval I (below 335 mbsf) is characterized by highly variable organic carbon and C/N records, which, except for the lowest part of Hole 960A (below 440 mbsf), are linearly correlated (Fig. 46). This suggests enhanced supply of terrestrial organic matter, at least during certain periods of the Cretaceous. In gen-

eral, very low HI values (below 50 mgHC/gTOC; Fig. 47) and the occurrence of plant debris or amorphous organic matter (see smear slide results in "Lithostratigraphy" section, this chapter) lead to the same interpretation. A more differentiated composition of organic matter with regard to thermal maturity, however, is suggested by the T_{max} record (Fig. 47). They scatter either at low values below 365°C (indicating immature organic matter) or above 450°C (evidencing high-to over-mature organic matter). It should be stressed that low T_{max} values do not necessarily correspond to sections with intermediate organic carbon contents. For example, Sections 195-960A-45R-1 and 50R-1 have high organic carbon contents (<1.3%) and low T_{max} values (<370°C) (Table 6). Similar organic geochemical characteristics

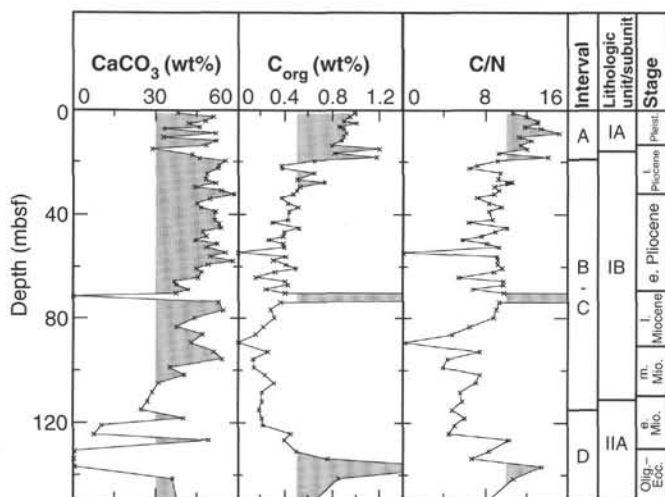


Figure 45. Carbonate content, total organic carbon content, and C/N ratios in sediments between 0 and 150 mbsf at Hole 960C. Intervals distinguished on the basis of carbonate and organic carbon records, lithologic units (see "Lithostratigraphy" section, this chapter), and preliminary stratigraphic stages are indicated.

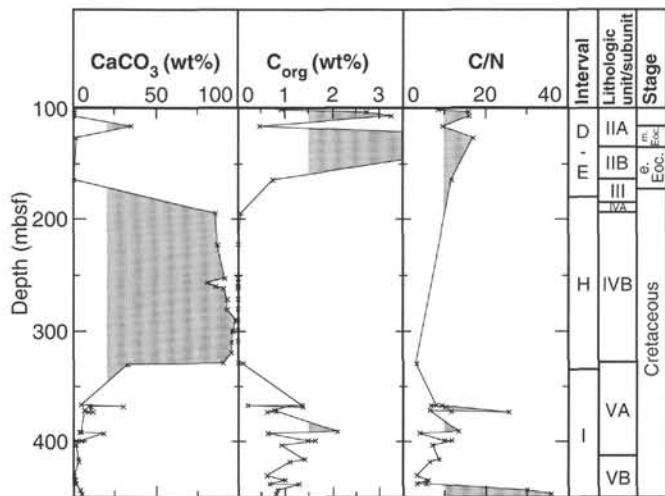


Figure 46. Carbonate content, total organic carbon content, and C/N ratios in sediments between 100 and 450 mbsf at Hole 960A. Intervals distinguished on the basis of carbonate and organic carbon records, lithologic units (see "Lithostratigraphy" section, this chapter), and preliminary stratigraphic stages are indicated.

were observed at the base of interval I of Site 959. Both units possibly may have been affected by previous thermal heating. A final interpretation of these basal sandstones, however, requires more detailed shore-based investigation (see "Organic Geochemistry" section, "Site 959" chapter, this volume).

SOURCE ROCK GEOCHEMISTRY

Concentrations of headspace methane and ethane were measured in Holes 960A and 960C. In the deeper hole, 960A (TD 451.2 mbsf), maximum methane concentrations reached only about 18,000 ppm in

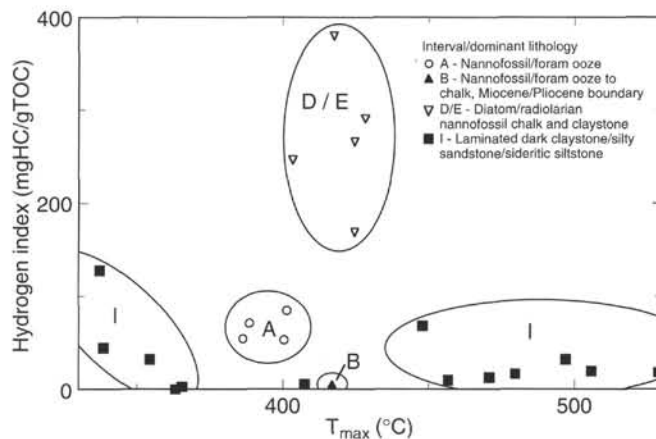


Figure 47. Hydrogen Index values vs. T_{max} values of different sediment types at Site 960. Intervals distinguished on the basis of carbonate and organic carbon records, and corresponding dominant lithologies (see "Lithostratigraphy" section, this chapter) are indicated. Hydrogen Index values of 0–50 mgHC/gTOC suggest elevated proportions of inert organic matter, 50–150 mgHC/gTOC suggests dominant terrestrial with minor contents of marine organic matter, and above 200 mgHC/gTOC suggests dominant marine organic matter. T_{max} values below 410°–420°C are characteristic of thermally immature organic matter, values between 420° and 460°C are characteristic of mature organic matter, and values above 460°C characterize over-mature organic matter.

Core 159-960A-57R. Ethane concentrations were less than 100 ppm throughout the hole.

In Hole 960C (TD 377 mbsf), methane concentrations were insignificant. No ethane was detected. From the aspect of safety and pollution considerations, Site 960 was benign.

INORGANIC GEOCHEMISTRY

Interstitial waters extracted from 13 whole round samples from Site 960 were analyzed. The majority of the interstitial water samples were taken from Hole 960C. One sample per core was taken from Cores 159-960C-1H through 7H (58 mbsf). Thereafter, one whole round sample was taken from every third core to a depth of 115.15 mbsf (159-960C-13H-3, 145–150 cm). Because of low recovery below this depth, typically less than 20%, only one additional whole round was taken from Hole 960C. This sample, 159-960C-23X-1, 7–12 cm, was collected in spite of low recovery so that an interstitial water sample from the palygorskite claystone with barite (see "Lithostratigraphy" section, this chapter) could be analyzed. Hole 960A was rotary drilled from the outset, and only three whole round samples were taken from this hole. In the upper 50 mbsf, whole round samples were not taken because drilling disturbance of unconsolidated sediments was inferred from visual inspection of the sediment through the core liner. At 52 and 86.65 mbsf two interstitial water samples were taken that were sufficiently well lithified to be trimmed and squeezed to extract interstitial water. The final sample from Hole 960A was taken from 392.50 mbsf (159-960A-50R-3, 140–150 cm). Interstitial water sampling between 86.65 and 392.50 mbsf, was precluded by a combination of low recovery and lithologies ill-suited for squeezing. Interstitial water data from Holes 960A and 960C are similar in overlapping depth intervals, and are plotted together in Figures 48 through 50. Detailed examination of depth variations in interstitial water composition reveals small discrepancies between samples from

Table 6. Summary of total organic carbon (Org-C), obtained from elemental analysis, and of T_{max}, S₁, S₂, S₃, hydrogen index (HI) values, and oxygen index (OI) values derived from Rock-Eval pyrolysis in sediments at Site 960.

Core, section, interval (cm)	Org-C (wt%)	T _{max} (°C)	S ₁ (mgHC/gRock)	S ₂ (mgHC/gRock)	S ₃ (mgHC/gRock)	HI (mgHC/gTOC)	OI (mgHC/gTOC)
159-960A-							
10R-5, 116-117	0.71	422	0.04	0.25	2.72	35	383
12R-3, 135-136	0.92	403	0.08	2.26	0.88	246	96
12R-5, 109-110	2.73	425	0.12	7.26	1.50	266	55
13R-1, 36-37	3.26	429	0.20	9.45	1.64	290	50
15R-1, 66-67	6.44	417	0.28	24.41	2.18	379	34
44R-1, 7-8	1.34	457	0.03	0.13	0.61	10	45
45R-1, 127-129	1.36	365	0.04	0.04	1.26	3	92
45R-2, 86-87	1.10	569	0.04	0.29	2.22	26	202
46R-2, 127-129	0.81	480	0.02	0.13	2.19	17	270
50R-1, 16-17	2.10	338	0.10	0.95	1.60	45	76
53R-1, 19-21	0.91	529	0.02	0.17	0.57	18	63
54R-2, 88-90	1.40	497	0.09	0.45	0.45	32	33
55R-1, 13-15	1.10	506	0.02	0.23	0.21	21	19
57R-3, 15-17	0.62	354	0.02	0.20	0.00	32	0
58R-2, 23-25	1.00	471	0.02	0.13	0.08	13	8
59R-1, 36-37	0.66	337	0.09	0.85	1.07	128	161
59R-1, 76-78	1.29	448	0.13	0.88	1.16	68	90
60R-2, 7-8	0.82	407	0.01	0.05	0.49	6	60
61R-1, 78-79	0.81	363	0.03	0.01	0.77	1	95
159-960C-							
1H-1, 123-124	0.99	388	0.13	0.70	3.35	71	340
1H-4, 42-43	1.01	386	0.15	0.56	3.38	55	336
2H-6, 112-116	1.20	401	0.16	1.02	3.20	85	266
3H-2, 110-111	1.17	400	0.08	0.62	3.01	53	257
8H-6, 110-111	5.66	417	0.01	0.12	2.59	2	46
15H-5, 134-135	1.78	425	0.12	2.98	1.01	168	57

Table 7. Interstitial water analyses from Holes 960A and 960C.

Core, section, interval (cm)	Depth (mbsf)	IW vol (mL)	pH	Alkalinity (mM)	Salinity (g/kg)	Ca (mM)	Mg (mM)	Sr (μM)	Cl (IC)	SO ₄ (mM)	NH ₄ (μM)	SiO ₂ (μM)	K (mM)	Mn (μM)	Fe (μM)	Na (mM)
159-960A-																
7R-2, 140-150	52.00	41	7.1	6.266	34.0	12.8	40.5	219.4	579	17.2	1119.64	246	10.2	1.5	85.0	484.8
10R-3, 140-150	82.70	45	6.9	6.682	34.0	15.4	39.1	249.3	555	13.6	1212.41	867	9.6	1.8	7.2	472.3
50R-1, 140-150	392.50					17.0	27.4	392.7	536	0.9	1650.00	246	5.6	7.5		461.5
159-960C-																
1H-2, 145-150	2.95	50	7.4	3.485	35.0	10.5	52.2	98.3	540	26.9	375.43	458	13.2	11.5	1.6	469.0
2H-3, 145-150	10.65	54	7.3	3.996	35.0	10.2	49.2	113.1	557	26.3	402.36	381	12.6	12.0	4.9	476.4
3H-3, 145-150	20.15	54	7.3	4.278	34.5	10.6	48.9	132.6	547	23.8	557.97	270	12.5	10.5	25.9	480.3
4H-3, 145-150	29.65	50	7.4	4.706	34.5	10.5	46.4	149.7	572	22.8	647.75	238	11.7	7.0	42.1	483.8
5H-3, 145-150	39.15	50	7.3	4.841	34.0	10.9	45.3	169.0	556	20.6	761.46	225	11.2	5.0	92.9	482.4
6H-3, 145-150	48.65	50	7.3	5.253	34.0	12.1	45.9	189.0	555	19.8	836.27	243	10.7	3.5	87.2	478.2
7H-3, 145-150	58.15	48	7.3	5.589	34.0	12.2	42.3	204.6	542	17.4	881.10	259	10.5	2.3	92.2	480.8
10H-3, 145-150	86.65	44	7.0	7.181	34.0	15.1	39.4	241.7	555	15.4	1035.71	347	9.3	2.3	92.2	479.7
13H-3, 145-150	115.15	35	7.0	7.710	34.0	16.3	37.4	270.1	553	12.4	1225.66	820	9.3	2.0	80.8	472.8
23X-1, 7-12	198.37	18	7.2	7.503	33.5	17.0	36.1	283.3	540	12.0	1300.76	921	7.3	1.3	106.8	467.1

Holes 960A and 960C. These subtle differences in pore-fluid composition between the two holes may be related to lithostratigraphic differences between the holes (see "Lithostratigraphy" section, this chapter).

Considering the close proximity of Site 960 to Site 959, it is not surprising that the pore-water chemistry of these two sites is similar in many respects, particularly in the upper 100 mbsf. Lithologic differences between these sites are small. The most notable differences, which are reflected in their pore-water profiles, are the presence of large hiatuses in Miocene and Oligocene sediments (see "Biostratigraphy" section, this chapter). Thus, uppermost Miocene to Pleistocene sediments are found at relatively similar depths at both sites, whereas the section below ~85 mbsf at Site 960 is extremely condensed relative to that at Site 959. In addition, lower Miocene-Pleistocene sediments at Site 960 have ~10% more calcium carbonate content and lower organic carbon weight percentages than those at Site 959 (see "Organic Chemistry" section, this chapter). In the following discussion, many of the similarities in pore-water profiles from these two sites, as well as some subtle differences, are noted explicitly. More detailed information about the pore-water chemistry of

Site 959 can be found in the "Inorganic Chemistry" section of the "Site 959" chapter (this volume). The data from the interstitial water analyses are given in Table 7.

Chloride concentrations of interstitial water samples from Site 960 exhibit a total range of 2%, and are similar to ambient seawater. Sodium concentrations, as calculated by charge balance, average 476 mM. The only interstitial water sample that was potentially distinct from the other samples in chloride concentration was the palygorskite claystone. This sample contains chloride concentrations 2% lower than the majority of the other samples and has a slightly lower salinity than the other samples. The cause of this difference is unclear. Given the small magnitude of this difference in chloride concentration, it seems most reasonable to attribute it to diagenetic processes rather than to mixing compositionally distinct fluids.

Microbially Mediated Organic-matter Degradation

The influence of organic-matter degradation on pore-water chemistry in the first 100 mbsf at Site 960 is similar to that at Site 959. We infer the complete consumption of dissolved oxygen in the sediment

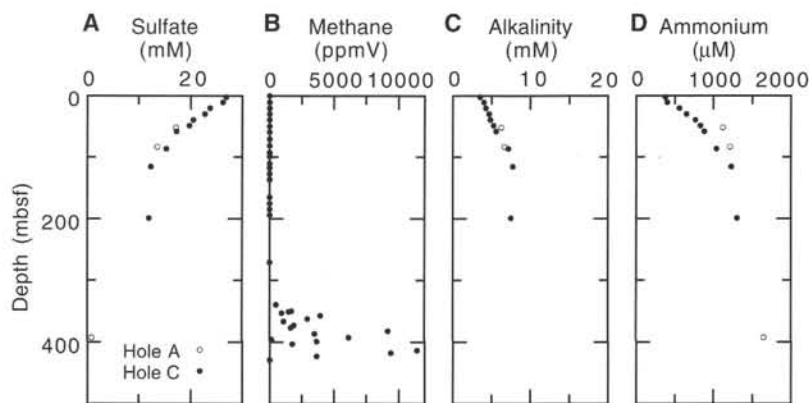


Figure 48. Interstitial water concentrations for (A) sulfate, (B) methane, (C) alkalinity, and (D) ammonium plotted vs. depth in the sediment at Site 960.

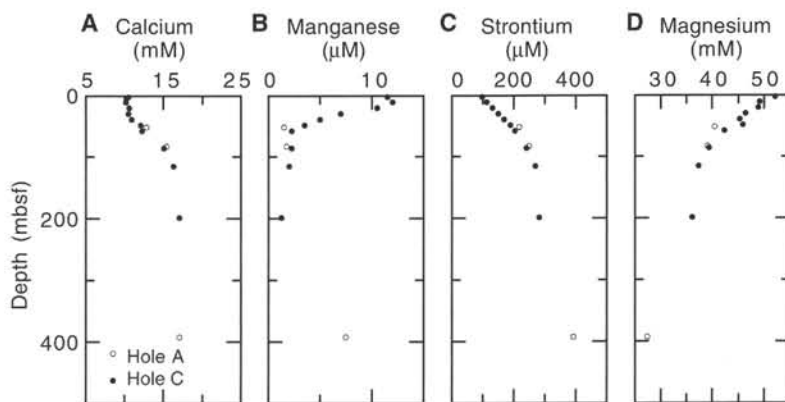


Figure 49. Interstitial water concentrations for (A) calcium, (B) manganese, (C) strontium, and (D) magnesium plotted vs. depth in the sediment at Site 960.

above 10 mbsf from the maximum in dissolved manganese near this depth (Fig. 48). As at Site 959, the depth of the onset of sulfate reduction at Site 960 cannot be identified with certainty. Identification of pyrite in smear slides as shallow as Core 159-960C-3H indicates the onset of sulfate reduction above 30 mbsf. Sulfate concentrations exhibit a nearly linear decrease with increasing depth in the sediment down to near 100 mbsf (Fig. 48A). The linear character of the uppermost portion of the profile suggests that diffusive resupply of sulfate to a broad zone of sulfate reduction within the sediment pile is controlling the vertical distribution of sulfate at Site 960. The onset of methanogenesis at 350 mbsf delineates the lower boundary of this zone of sulfate reduction (Fig. 48B). Increases in alkalinity (Fig. 48C) and dissolved ammonium concentration (Fig. 48D) with depth also reflect the influence of organic matter degradation over the first 100 mbsf at Site 960. In comparison to Site 959, the absolute concentrations of ammonium and alkalinity at Site 960 are slightly lower. The reason for this is unclear. We speculate that the lower average sedimentation rate at Site 960 relative to Site 959 results in a larger portion of the initially deposited organic matter to be metabolized near the sediment/water interface, allowing ammonium and alkalinity to diffuse into the overlying waters.

Below 100 mbsf, it is difficult to characterize the interstitial water chemistry because of the small number of widely spaced samples. The rate of decrease in pore-fluid sulfate concentrations appears to slow markedly below ~100 mbsf. Consequently, the onset of methanogenesis occurs near 350 mbsf, 50 mbsf deeper than at Site 959. The break-in slope of the sulfate profile may reflect a diminished rate of sulfate reduction because of the diminished rates of organic-matter

degradation at depth at Site 960. Alkalinity remains nearly constant below 100 mbsf. Ammonium concentrations increase only modestly, remaining nearly 50% lower than the maximum values measured in Site 959 pore fluids. The low values of alkalinity and ammonium concentrations are consistent with inferred diminished rate of organic-matter decomposition. However, it is noteworthy that three distinct organic-rich zones occur between 100 and 170 mbsf (see "Organic Geochemistry" section, this chapter). As no interstitial water samples were obtained proximal to these zones, their influence on the pore-water chemistry at this site cannot be assessed. Gradual dissolution of barite present in sediments from Cores 159-960C-21X through 23X may provide an additional source of sulfate to the pore water. This process could also account for the observed break in slope of the sulfate profile below 100 mbsf.

Carbonate Diagenesis

Dissolved calcium concentrations are similar to those of seawater (10.5 mM) in the upper 30 mbsf of Site 960. Over the next 80 mbsf, they increase sharply downhole by ~55%. Below this level, there are fewer data points, but they suggest little variation in concentrations (16–17 mM) down to 198.4 mbsf, similar to profiles of other dissolved species discussed above (Fig. 49A). The dissolved calcium concentration of the single data point at 392.5 mbsf within the palygorskite claystone is similar to that of the next sample nearly 200 m above (Table 7). Thus, the greatest change in the calcium profile seems to occur in the interval from 30 to 90 mbsf within the upper Miocene to Pliocene sequence. We infer that the increase in interstitial

calcium may be the result of calcite dissolution within the nanofossil chalk, which is found at shallower depths in this interval (between 47.2 and 55.2 mbsf, see "Lithostratigraphy" section, this chapter) than at Site 959. Calcium may also have been released from the alteration of silicate minerals as evidenced by the presence of zeolites observed in smear slides in or below Core 159-960C-11H. The overall calcium profile differs significantly from that of Site 959, particularly in the upper 100 mbsf, where substantial carbonate precipitation was inferred, based on the marked drop in concentrations at the level of the ooze to chalk transition (see "Inorganic Chemistry" section, Site 959 chapter, this volume). The cause of such differences in the behavior of dissolved calcium at these sites is not apparent at this time.

The profile of dissolved manganese in the upper 200 mbsf of Site 960 is similar to that of Site 959 from the same depth interval (Fig. 49B). At Site 960, concentrations increase to a maximum (12 μM) at ~11 mbsf from the reduction of manganese oxide particulates (see "Inorganic Geochemistry" section, Site 959 chapter, this volume). There is a decrease of ~80% in the next 48 mbsf downhole, and concentrations appear to remain almost constant at background levels down to 198 mbsf. The lowermost data point at 392.5 mbsf has an elevated manganese content of 7 μM . The exponential drop in concentrations reflects a manganese sink in the upper part of the nanofossil chalk sequence, similar to that inferred at Site 959. This is probably associated with the precipitation of a secondary manganese-bearing carbonate in an active diagenetic front.

The gradual increase in interstitial water strontium concentrations with depth at Site 960 is likely the result of dissolution-precipitation processes (i.e., recrystallization) in the calcium carbonate (Gieskes, 1981; Baker et al., 1982) (Fig. 49C). The steepest gradient occurs in the upper 90 mbsf, where strontium concentrations increase by 140 μM , indicating a flux of dissolved strontium to the overlying water. In this interval, absolute concentrations at Site 960 are higher than at Site 959, probably because of the higher relative abundance of calcite in these sediments. Below this level, strontium concentrations increase slightly down to ~198 mbsf. The highest concentration (393 μM) was measured in the deepest sample, the palygorskite claystone.

The dissolved magnesium profile exhibits a trend of decreasing concentrations with depth (Fig. 49D). This trend is similar to that at Site 959, but absolute concentrations are lower at Site 960. From near-seawater values in the uppermost sample, concentrations decrease by ~28% over the next 115 mbsf. Based on one data point, the gradient appears to be significantly less steep from 115 to 198 mbsf. A likely explanation for the measured pattern is the uptake of magnesium during the formation of opal (Kastner et al., 1977; Donnelly and Merrill, 1977). Siliceous microfossils in relatively high abundance were observed in smear slides as high in the section as ~112 mbsf, corresponding to the depth of increased dissolved silica concentrations discussed below (Fig. 50A). This is further supported by the occurrence of porcellanite and chert of late Oligocene and Eocene age, respectively, beginning at ~125 mbsf.

Silica, Potassium, and Iron Profiles

Dissolved silica concentrations at Site 960 appear to be strongly dependent on sediment lithology, just as at Site 959. Initial silica concentrations are roughly 500 μM , and decrease to a minimum concentration at approximately 50 mbsf (Fig. 50A). A similar minimum occurs at Site 959. At both sites, minimum silica concentrations are coincident with a nanofossil ooze essentially devoid of biogenic silica. Close to 100 mbsf dissolved silica concentrations increase abruptly to values slightly less than 1000 μM . This shift is associated with a transition to a lithology containing biogenic opal and abundant zeolite (see "Lithostratigraphy" section, this chapter). Although samples are widely spaced, it appears that silica concentrations remain high to a depth greater than 200 mbsf. The silica concentration of the deepest interstitial water sample (393 mbsf) returns to a silica concentration

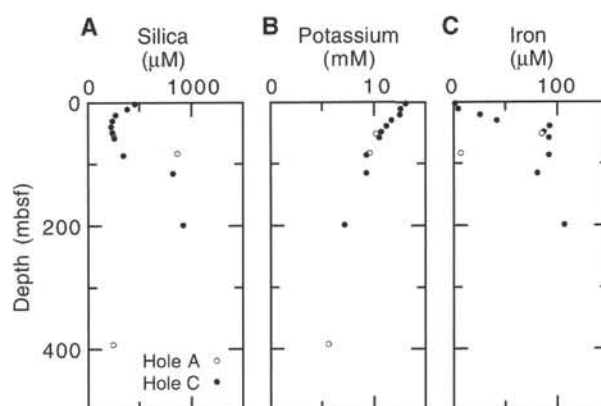


Figure 50. Interstitial water concentrations for (A) silica, (B) potassium, and (C) iron plotted vs. depth in the sediment at Site 960.

below 500 μM , likely reflecting the paucity of highly soluble siliceous material in the claystone occurring at this depth.

The profile of dissolved potassium at Site 960 shows clear evidence of potassium removal from the interstitial water (Fig. 50A). In the first 30 mbsf, potassium concentrations exceed the potassium concentration of seawater. The highest concentration sample, 13 mM potassium, is from the shallowest pore-water sample in Section 159-960C-1H-2. Potassium concentrations decrease systematically with increasing depth, resulting in nearly 50% potassium removal over the uppermost 400 mbsf of Site 960 sediments. Similar evidence of potassium removal was documented at Site 959, but did not begin until approximately 50 m deeper. Given the abundance of zeolite and glauconite in sediments from Site 960, we believe potassium uptake by authigenic clay mineral formation is the most plausible explanation for the potassium data. Alternative explanations for this decrease in dissolved potassium concentrations are given in the "Inorganic Geochemistry" section, "Site 959" chapter, this volume.

The dissolved iron profile from Site 960 is shown in Figure 50C. Below 10 mbsf, the rapid increase in dissolved iron concentrations indicates that reduction of solid phase reactive iron is occurring in the sediment. As expected, the majority of iron reduction occurs below the depth of manganese reduction (Fig. 49B). With one exception (159-960A-10R-3, 140–150 cm), dissolved iron concentrations stabilize in the range between 81 and 106 μM . Assuming the iron data are not subject to oxidation artifacts, the relatively constant iron concentrations may indicate that dissolved iron concentrations at Site 960 are being regulated by equilibrium with an authigenic iron mineral, such as siderite or glauconite. Both of these phases have been identified in smear slides from Site 960 (See "Lithostratigraphy" section, this chapter).

PHYSICAL PROPERTIES

Measurements were made on whole cores at Site 960 using the magnetic susceptibility meter, gamma-ray attenuation porosity evaluator (GRAPE), *P*-wave Logger (PWL), and Natural Gamma Radiation (NGR) tool. Full-space thermal conductivity measurements were made. Index properties were calculated from wet and dry masses and from wet and dry volumes. Compressional (*P*) wave velocity, shear strength, and electrical resistivity were measured on split cores. No PWL velocity measurements were made at Hole 960A, because this hole was RCB cored and the core quality was not appropriate. One core was recovered at Hole 960B, and only the NGR level was measured. Hole 960A has a higher number of observations below 180 mbsf, whereas Hole 960C has the highest sampling frequency above

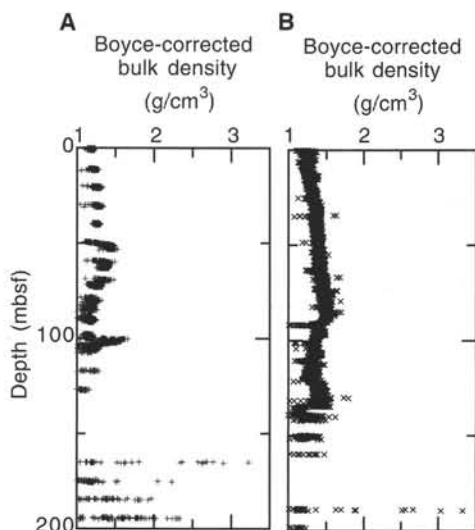


Figure 51. Boyce-corrected density variation with depth at Site 960. A. Hole 960A. B. Hole 960C.

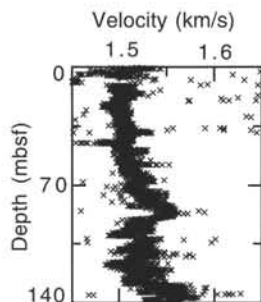


Figure 52. Horizontal *P*-wave velocity variation with depth at Hole 960C; results from the PWL.

180 mbsf. Consequently, we based our analysis primarily on data from Hole 960C for the upper part of the section and on data from Hole 960A for the lower part. Descriptions of the experimental methods are provided in the “Physical Properties” section of the “Explanatory Notes” chapter (this volume). All tables presented and MST data are available on CD (this volume).

Multisensor Track

The results of the magnetic susceptibility observations, taken at 5-cm intervals, are presented in the “Paleomagnetism” section (this chapter).

The GRAPE density values were edited and Boyce-corrected, and only the maximum bulk density values were taken into consideration. At Hole 960C, bulk density gradually increases from about 1.3 to 1.6 g/cm³ between the seafloor and 85 mbsf (Fig. 51). The bulk density ranges from 1.4 to 1.6 g/cm³ between 85 and 135 mbsf, with local minimum at 110 mbsf and local maxima at 85 and 130 mbsf. The sparse number of measurements below 140 mbsf show more scattered bulk density values. The downhole trend of bulk density at Hole 960A mirrors that of Hole 960C if the data are depth shifted by about 25 m (intervals at Hole 960C lie 25 m lower than at Hole 960A).

The horizontal *P*-wave velocity was measured down to 140 mbsf at Hole 960C (Fig. 52) and edited in two steps. No PWL data were

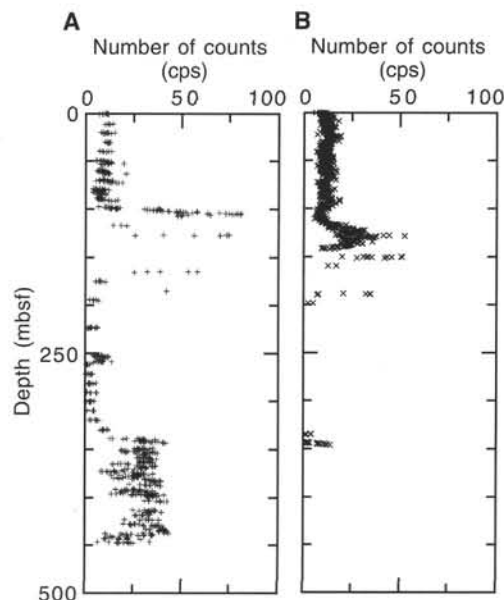


Figure 53. Variation of total number of counts with depth at Site 960; results from the NGR. A. Hole 960A. B. Hole 960C.

collected at Hole 960A because the core diameter was reduced by the drilling method. The PWL velocity increases from 1.49 km/s at the seafloor to 1.56 km/s at 85 mbsf. No significant change in lithology was observed at this depth. Between 100 and 130 mbsf, the velocity ranges from 1.50 to 1.54 km/s. At 130 mbsf, the shift to higher velocity values (about 1.55–1.57 km/s) reflects the change of lithology from micrite nanfossil chalk to glauconitic claystone.

NGR data were collected with 10- or 30-s counting periods, and the background radiation (8.74 cps) was subtracted from all measurements. The total number of counts is fairly constant and varies from 10 to 15 cps in the upper 110 m of Hole 960C. There is a rapid increase in the number of counts below 110 mbsf, with two peaks occurring at 130 and 150 mbsf (Fig. 53). Both peaks are located within lithologic Subunit IIA and probably are induced by local increases in the glauconite content. The downhole trend in the Hole 960A data corresponds well to Hole 960C data if the two data sets are depth shifted by 25 m with respect to each other (Fig. 53). The maximum values are, however, significantly higher at Hole 960A than at Hole 960C. This is probably caused mainly by the drilling disturbances (i.e., clayey sediments were washed out between glauconitic layers at Hole 960A during drilling), and not by an actual variation in lithology between the two holes. The sparse number of measurements between 190 and 340 mbsf at Hole 960A show low values (≤ 10 cps). The shift of more than 10 cps that is observed about 330 mbsf corresponds to the boundary between lithologic Units IV and V (329.0 mbsf at Hole 960A).

Thermal Conductivity Measurements

We measured the thermal conductivity in full-space configuration in cores from Holes 960A and 960C. The data were not corrected for in situ pressure and temperature because the difference between the uncorrected and corrected data is estimated to be significantly less than the error caused by drilling disturbances and technical problems with the equipment.

Only 15 measurements of thermal conductivity were made at Hole 960A, and the values range between 0.82 and 1.28 Wm⁻¹C⁻¹ (Table 8;

Table 8. Thermal conductivity data from Site 960.

Core, section, interval (cm)	Depth (mbsf)	Lithologic unit	Thermal conductivity ($\text{Wm}^{-1}\text{C}^{-1}$)
159-960A-7R-1, 75	49.85	IB	0.85
7R-3, 75	52.85	IB	1.11
8R-1, 75	59.65	IB	0.92
8R-3, 75	62.65	IB	1.22
9R-1, 75	69.35	IB	0.92
9R-3, 75	72.35	IB	1.22
10R-1, 75	79.05	IB	1.00
10R-3, 50	81.80	IB	0.82
11R-1, 75	88.75	IB	1.03
12R-1, 70	98.30	IB	0.83
12R-3, 75	101.40	IIA	1.28
12R-5, 75	104.40	IIA	0.83
13R-1, 20	107.50	IIA	0.89
14R-1, 30	117.20	IIA	1.04
20R-1, 60	175.10	III	1.18

Only a part of this table is reproduced here. The entire table appears on the CD-ROM (back pocket).

Fig. 54). At Hole 960C, there are more measurements of thermal conductivity, and they appear to be less scattered than at Hole 960A. They range between 0.81 and 1.38 $\text{Wm}^{-1}\text{C}^{-1}$, with a maximum occurring at 67 mbsf. This trend approximately follows that of bulk density.

Index Properties

We determined the phase relationship of the marine sediments recovered from Site 960 using gravimetric methods. The depth shift of 25 m between the measurements in Holes 960A and 960C can also be observed in index properties data. There are two different downhole trends of index properties at Hole 960A. The upper 175 m has distinctly higher values of porosity, water content, and void ratio than the lower part (Table 9; Fig. 55A–G). This trend is most evident in the void ratio data, which range from 1.43 to 3.50 in the upper part and drop to less than 0.70 in the lower part. The reverse downhole trend is observed in the bulk- and dry-density data. Bulk density varies from 1.28 to 1.92 g/cm^3 in the upper part of Hole 960A, whereas in the lower part, most values are larger than 2.30 g/cm^3 . The shift occurs at the boundary between lithologic Units III and IV (at 175.7 mbsf). Variations in index properties with depth in the upper part reflect general variations in lithology and age. In the lower part of the hole, the lowest values of porosity were measured in the quartz sand limestones of lithologic Subunit IVB, and were probably caused by cementation.

Velocimetry

Discrete measurements of *P*-wave velocity were made at Holes 960A and 960C close to the location of samples for index properties measurements in soft sediments and on the same samples in lithified ones.

Generally, low (<1.67 km/s) and almost constant velocities were measured in both horizontal and vertical directions in the upper 175 m at Hole 960A (Table 10; Fig. 56). There is a shift to higher and more scattered values (>4.00 km/s) between 185 and 330 mbsf. This shift occurs at the boundary between lithologic Units III and IV (at 175.7 mbsf). In this interval the highest velocity values were noted for quartz sand limestones. Velocity drops to slightly lower and more scattered values (about 2.5 km/s) across the boundary between lithologic Units IV and V (at 329.0 mbsf).

The anisotropy of velocity calculated from discrete velocity measurements in the vertical and horizontal directions (Table 10; Fig. 56) ranges from -0.15 to 0.11 between 88 and 330 mbsf. Anisotropy

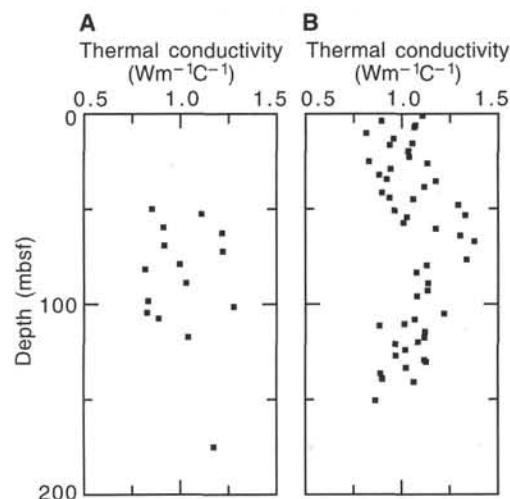


Figure 54. Thermal conductivity variation with depth at Site 960. A. Hole 960A. B. Hole 960C.

changes below 348 mbsf to broader, more scattered and generally positive values. Maximum anisotropy (0.51) was calculated in the finely laminated siltstone at 434 mbsf.

Table 10 further shows *P*-wave velocities corrected to in situ conditions. Corrected velocity is calculated from in situ seawater velocity, porosity, seawater velocity in the laboratory, and sediment velocity (cf. "Physical Properties" section, "Explanatory Notes" chapter, this volume). The downhole variation of in situ seawater velocity and porosity was determined from regression analysis. The linear and the power regression models in KaleidaGraph 3.0.4 were used to generate curve-fit equations for porosity and in situ seawater velocity. The curve fit between the equations and data is good (>0.99) for in situ seawater velocity at Holes 960A and 960C. The curve fit between the equations and data for porosity is not as good: the best curve fit (0.88) was obtained for the upper part of Hole 960C, whereas the poorest fit (0.41) was obtained at the lower part Holes 960A and 960C.

Undrained Shear Strength

Undrained shear strength was measured on Cores 5R to 12R in Hole 960A and on almost all cores from Hole 960C using either the vane shear device or the penetrometer. The two methods give similar magnitudes of the undrained shear strength in intervals where overlapping measurements were obtained at Site 960.

Shear data from both holes show a similar distribution, but the trends are more distinct for Hole 960C data as the sampling frequency was higher in this hole (Table 11; Fig. 57). At Hole 960C in the upper 32 m, values are very low (<5 kPa); below this level, there is an increase to higher values (≥ 20 kPa) and then a progressive increase downhole. The wide scatter of shear strength values observed beneath 90 mbsf at Hole 960C ranges from 17 to 164 kPa and reflects the heterogeneous nature of the sediments.

Electrical Resistivity

There are two different trends of resistivity at Hole 960C, where both horizontal and vertical components follow the same trend (Table 12; Fig. 58). The upper 51 m has fairly constant values (0.06–0.12 Ωm). A shift to higher and more scattered values occurs below 64 mbsf, with values ranging from 0.09 to 0.18 Ωm , and with the maximum value observed at 111 mbsf in Hole 960C.

Table 9. Index properties data from Site 960.

Core, section, interval (cm)	Depth (mbsf)	Lithologic unit	Water content		Density			Porosity (%)	Void ratio (1)
			Total wet mass (%)	Mass of solids (%)	Wet bulk (g/cm ³)	Solids-grain (g/cm ³)	Dry (g/cm ³)		
159-960A-									
5R-1, 123	30.83	IB	42.05	72.56	1.67	2.62	0.97	68.39	1.86
6R-1, 85	40.15	IB	44.10	78.89	1.67	2.64	0.93	71.95	2.03
7R-2, 114	51.74	IB	40.11	66.96	1.70	2.67	1.02	66.61	1.75
7R-3, 102	53.12	IB	37.22	59.30	1.72	2.69	1.08	62.65	1.56
8R-1, 92	59.82	IB	37.95	61.17	1.76	2.65	1.09	65.33	1.58
8R-3, 66	62.56	IB	38.55	62.74	1.74	2.70	1.07	65.58	1.65
9R-1, 95	69.55	IB	37.40	59.75	1.67	2.68	1.04	60.86	1.56
9R-3, 80	72.40	IB	41.83	71.91	1.57	2.65	0.91	64.18	1.86
10R-1, 126	79.56	IB	54.20	118.34	1.28	2.69	0.59	67.71	3.11
10R-3, 45	81.75	IB	54.09	117.80	1.34	2.60	0.62	70.79	2.98
10R-5, 55	84.85	IB	57.80	136.94	1.33	2.62	0.56	74.77	3.50
11R-1, 58	88.58	IB	52.18	109.12	1.37	2.63	0.66	69.91	2.80
11R-3, 15	91.15	IB	55.85	126.52	1.32	2.61	0.58	72.18	3.22
12R-1, 107	98.67	IB	54.32	118.90	1.34	1.43	0.61	71.09	1.66
12R-2, 140	100.50	IIA	34.87	53.54	1.92	2.74	1.25	65.22	1.43

Only a part of this table is reproduced here. The entire table appears on the CD-ROM (back pocket).

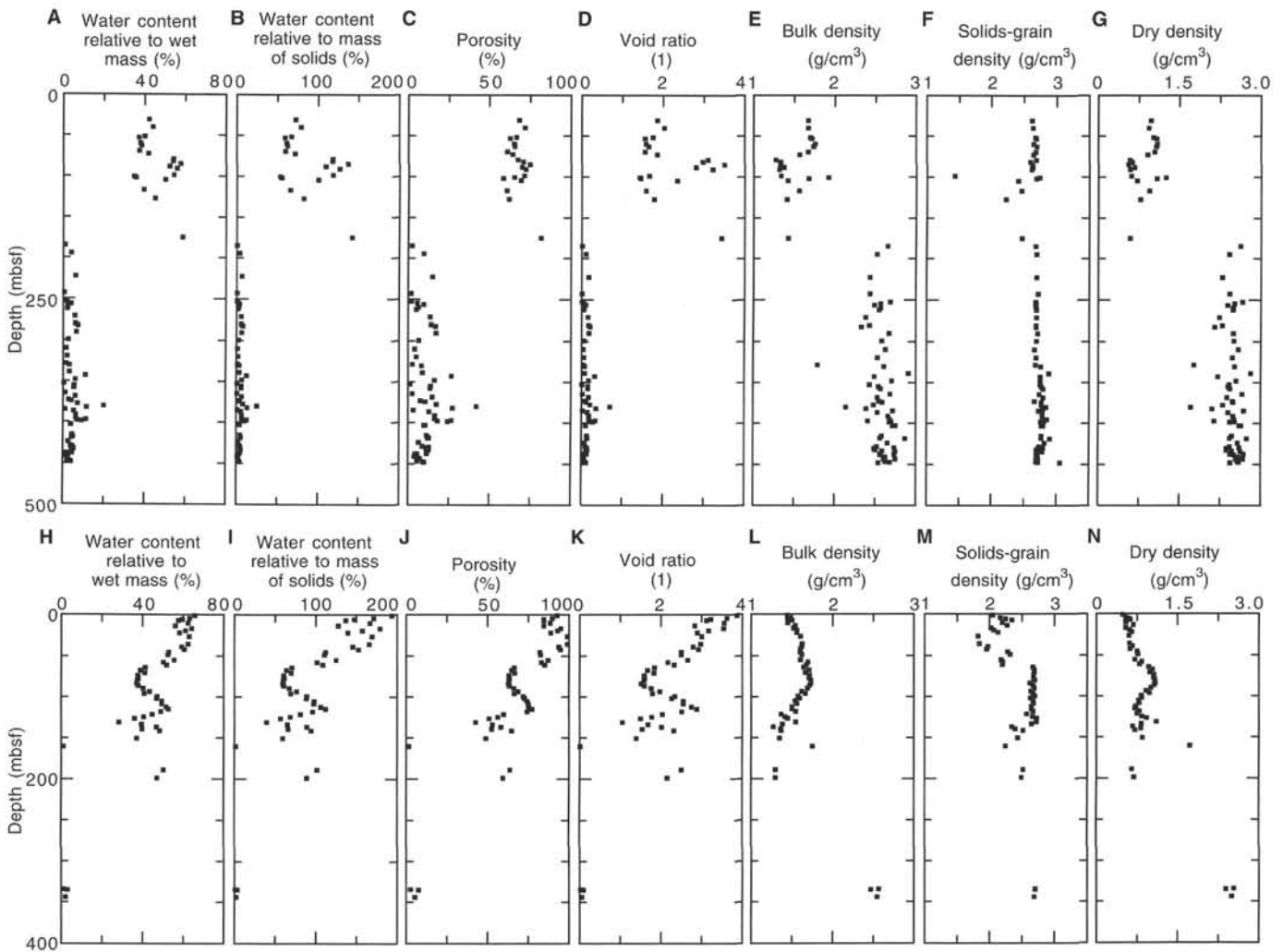


Figure 55. Index properties variation with depth at Site 960. A–G. Hole 960A. H–N. Hole 960C.

Table 10. P-wave velocity and anisotropy data from Site 960.

Core, section, interval (cm)	Depth (mbsf)	Lithologic unit	Uncorrected velocity			Anisotropy		Corrected velocity			DSV
			Vert (km/s)	Hor 1 (km/s)	Hor 2 (km/s)	Hor 1 (1)	Hor 2 (2)	Vert (km/s)	Hor 1 (km/s)	Hor 2 (km/s)	
159-960A-											
5R-1, 128	30.88	IB	1.537	—	—	—	—	1.517	—	—	1
5R-1, 131	30.91	IB	—	1.578	—	—	—	—	1.557	—	3
6R-1, 89	40.19	IB	1.535	—	—	—	—	1.517	—	—	1
6R-1, 91	40.21	IB	—	1.561	—	—	—	—	1.543	—	3
7R-2, 118	51.78	IB	1.546	—	—	—	—	1.530	—	—	1
7R-2, 121	51.81	IB	—	1.551	—	—	—	—	1.535	—	3
7R-3, 106	53.16	IB	1.540	—	—	—	—	1.524	—	—	1
7R-3, 110	53.20	IB	—	1.550	—	—	—	—	1.534	—	3
8R-1, 99	59.89	IB	—	1.592	—	—	—	—	1.576	—	3
8R-1, 100	59.90	IB	1.567	—	—	—	—	1.551	—	—	1
8R-3, 72	62.62	IB	—	1.572	—	—	—	—	1.556	—	3
8R-3, 74	62.64	IB	1.552	—	—	—	—	1.537	—	—	1
9R-1, 80.9	69.41	IB	1.613	—	—	—	—	1.597	—	—	1
9R-1, 81.6	69.42	IB	—	1.670	—	—	—	—	1.653	—	3
9R-3, 73.6	72.34	IB	1.551	—	—	—	—	1.537	—	—	1

Note: Vert = vertical direction (along core); Hor 1 = horizontal direction (perpendicular to cut core face); Hor 2 = horizontal direction perpendicular to Hor 1. DSV 1 = Digital Sound Velocimeter; DSV 3 = Hamilton Frame Velocimeter.

Only a part of this table is reproduced here. The entire table appears on the CD-ROM (back pocket).

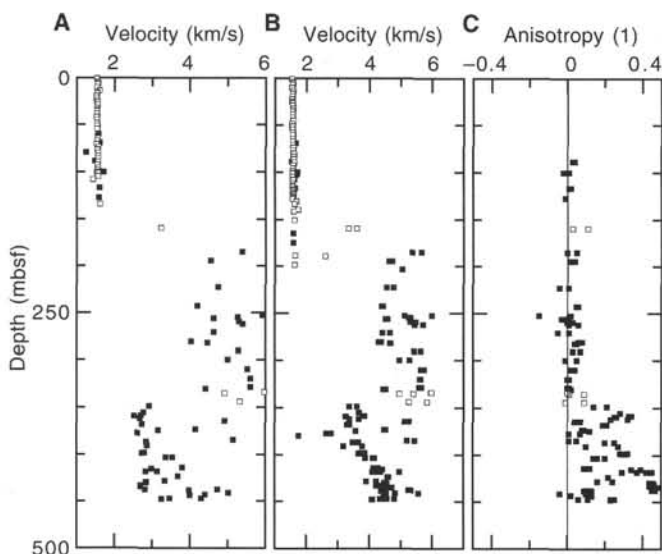


Figure 56. Results of discrete velocity measurements at Site 960. A. P-wave velocity in vertical direction vs. depth. B. P-wave velocity in horizontal directions vs. depth. C. Anisotropy vs. depth. Solid squares = Hole 960A, open squares = Hole 960C.

The formation factor was calculated using a pore-water resistance of 161 Ωm. It ranges from 0.34 to 1.01 at Hole 960C and between 0.78 and 1.08 at Hole 960A. There was insufficient time available to correlate porosity of different lithologies to the corresponding formation factor.

Comparison Between Continuous and Discrete Measurements

Continuous Boyce-corrected bulk-density data recorded with the MST and gravimetric bulk-density data from discrete measurements at Hole 960C follow the same trend and show peak values at 85 mbsf, just above the biostratigraphic boundary between upper and middle Miocene, for which no change in lithology was recorded (Fig. 59A). However, continuous Boyce-corrected bulk-density values are consistently about 0.2 g/cm³ lower than those from discrete measure-

Table 11. Undrained shear strength measurements made at Site 960.

Core, section, interval (cm)	Depth (mbsf)	Lithologic unit	Shear strength	
			Vane shear (kPa)	Penetrometer (kPa)
159-960A-				
5R-1, 139	30.99	IB	2.60	—
6R-1, 101	40.31	IB	3.70	—
7R-2, 129	51.89	IB	2.90	—
8R-1, 108	59.98	IB	39.10	—
9R-1, 91.4	69.51	IB	64.00	—
9R-1, 91	69.51	IB	—	44.15
9R-3, 83.2	72.43	IB	92.00	—
9R-3, 83	72.43	IB	—	83.39
10R-1, 133.7	79.64	IB	33.50	—
10R-1, 134	79.64	IB	—	58.86
10R-3, 66.2	81.96	IB	26.20	—
10R-3, 66	81.96	IB	—	36.79
10R-5, 96	85.26	IB	—	39.24
11R-3, 22.3	91.22	IB	33.30	—

Only a part of this table is reproduced here. The entire table appears on the CD-ROM (back pocket).

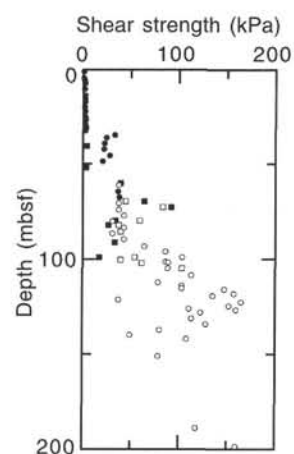


Figure 57. Undrained shear strength variation with depth at Site 960. Squares = Hole 960A, circles = Hole 960C, solid symbols = vane shear data, open symbols = penetrometer data.

Table 12. Electrical resistivity and formation factor data from Site 960.

Core. section, interval (cm)	Depth (mbsf)	Lithologic unit	Resistivity		Formation factor	
			Vert (Ω m)	Hor (Ω m)	Vert (1)	Hor (1)
159-960A-						
8R-1, 70	59.60	IB	0.16	0.14	0.86	0.78
9R-1, 118	69.78	IB	0.20	0.16	1.08	0.89
12R-1, 55	98.15	IB	0.17	0.17	0.95	0.93
12R-2, 37	99.47	IB	0.19	0.18	1.04	0.99
19R-1, 15	164.95	III	0.16	0.16	0.87	0.86
159-960C-						
1H-1, 122	1.22	IA	0.07	0.10	0.39	0.54
1H-3, 133	4.33	IA	0.09	0.10	0.47	0.54
1H-5, 33	5.83	IA	0.07	0.06	0.39	0.32
2H-1, 105	7.25	IA	0.07	0.07	0.40	0.40
2H-3, 107	10.27	IA	0.06	0.06	0.34	0.35
2H-5, 123	13.43	IA	0.08	0.09	0.46	0.47
2H-7, 33	15.53	IA	0.10	0.09	0.53	0.52
3H-1, 113	16.83	IB	0.09	0.09	0.48	0.48

Note: Vert = vertical direction (parallel to core axis), Hor = horizontal direction (perpendicular to cut core axis).

Only a part of this table is reproduced here. The entire table appears on the CD-ROM (back pocket).

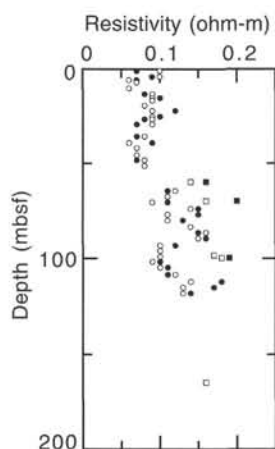


Figure 58. Electrical resistivity variation with depth at Site 960. Squares = Hole 960A, circles = Hole 960C, solid symbols = vertical resistivity data, open symbols = horizontal resistivity data.

ments. This is expected because the densities were determined using two significantly different methods.

Comparisons between continuous PWL velocity data and discrete horizontal velocity reveal a similar relationship (Fig. 59B). PWL velocities are generally about 0.5 km/s lower than those from discrete measurements. The difference in magnitude is probably related to the fact that sediments become more compacted in DSV 3 than on the MST.

Summary

Most of the physical properties data (discrete and continuous) correlate well with each other and with major lithologic boundaries. In addition, changes are common in the downhole trends of data at biostratigraphic boundaries. Thus, an environmental event that results in a change in calcareous nannoplankton and planktonic foraminifers could also influence the physical properties of sediments without a significant change in their lithology. The MST, index properties, and velocimetry data show that the sedimentary sequence of Hole 960A is shifted about 25 m above that of Hole 960C.

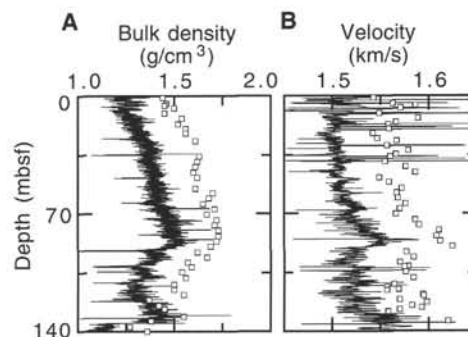


Figure 59. Comparison between continuous and discrete measurements at Hole 960C. **A.** Boyce-corrected bulk density and gravimetric bulk-density variation vs. depth. **B.** Horizontal *P*-wave velocity variation with depth, measured from the PWL and DSV 3. Lines correspond to continuous measurements, and open squares correspond to discrete measurements.

The local maximum in PWL velocity, discrete velocity, GRAPE density, and bulk density (Fig. 58) in Hole 960C data at 85 mbsf does not correlate with a change in lithology (cf. Core 159-960C-10H). However, this may be related to the biostratigraphic unconformity at 85 mbsf. There is another discontinuity in GRAPE density, PWL velocity, magnetic susceptibility (see "Paleomagnetism" section, this chapter), and index properties data at 92 mbsf. This depth corresponds to the biostratigraphic boundary between the upper and middle Miocene, as well as to a slight increase in clay and pyrite content. The boundary between lithologic Units I and II at 111.2 mbsf in Hole 960C is most apparent in the GRAPE density and index properties data (Figs. 51, 55). The discontinuity at 130 mbsf in Hole 960C in the PWL, NGR, and index properties data occurs at the change of lithology from micrite nannofossil chalk to glauconitic claystone (also the biostratigraphic boundary between the lower Miocene and middle Eocene; Figs. 52, 53, 55). The boundary between lithologic Units IV and V (at 329 mbsf) in Hole 960A is well reflected by the NGR and discrete velocity data, and in some of the index properties data (Figs. 53, 55, 56). There is a distinct change in GRAPE density, NGR, index properties, and velocimetry data at about 175 mbsf (Figs. 51, 53, 55, 56); this depth corresponds to the boundary between lithologic Units III and IV. This offset reflects the totally different lithologies (chert and claystone vs. limestone) and ages (early Eocene vs. Early Cretaceous).

DOWNHOLE MEASUREMENTS

Logging Operations and Log Quality

Logging at Site 960 was severely hampered by adverse borehole conditions. Only a modified Quad tool string was run in Hole 960A because of the large borehole diameter, which exceeded the caliper range (17 in.) for most of the logged interval. The Formation Micro-Scanner (FMS) and Geochemical Logging Tool String (GLT) both require a maximum borehole width of less than 14.5 in. to collect data of reasonable quality, so they were not run in this hole. In Hole 960C, the modified seismic stratigraphic tool string deployed included the High Temperature Lithodensity Tool (HLDT) to provide caliper measurements. To lower the risk of losing the nuclear source, it was removed from the HLDT. Although the GLT was not run in this hole, the FMS tool string was deployed despite the large hole diameter, in view of the importance of obtaining structural data at this site. Seastate conditions were mild and the wireline heave compensator was employed during most of the logging.

In Hole 960A, an impassable bridge prevented the modified Quad combination from reaching the total depth (TD) of the hole (451.3

Table 13. Summary of logging operations at Site 960.

Hole	Tool string	Tool string components	Depth (mbsf)
960A	Quad	DITE/HLDT/CNT-G/SDT/NGTC/TLT	Main: 361.3–73.3 Repeat: 265.3–73.3
960C	Seismic stratigraphic	DITE/HLDT*/SDT/NGTC/TLT**	Main: 374.6–159.7
	FMS	FMS/GPIT/NGTC	Main: 354.5–173.7

Note: * = used with source removed for caliper only; ** = TLT with bullnose on end. DITE = Dual Induction Resistivity Tool; HLDT = High Temperature Lithodensity Tool; CNT-G = Compensated Neutron Porosity Tool; SDT = Sonic Digital Tool (Array); NGTC = Natural Gamma-Ray Tool; TLT = Lamont-Doherty Temperature Tool; FMS = Formation MicroScanner; GPIT = General Purpose Incliner Tool.

mbsf) and logging thus commenced at 361.3 mbsf. A main log (361.3–73.3 mbsf) and a repeat log (265.3–73.3 mbsf) were collected before logging was terminated because of poor borehole conditions. Although the seismic stratigraphic tool string was able to reach within 4 m of the total depth (374.6 mbsf; TD = 377.7 mbsf) at Hole 960C, borehole blockage prevented the FMS tool string from getting deeper than 354.5 mbsf. A main (374.6–159.7 mbsf) log was obtained with the seismic stratigraphic tool string, which was run at about 900 ft/hr, with only standard mode (15-cm sampling) data recorded. The FMS tool string was run at about 1800 ft/hr over the interval 354.5 to 173.7 mbsf. A summary of logging operations for both holes is presented in Table 13.

Data Processing

Data from both holes suffered from the effects of borehole washout. The density, porosity, and photoelectric logs (in Hole 960A) and sonic data (in both Hole 960A and 960C) deteriorate where washout prevented the tool string from maintaining close contact with the borehole wall (see processed logs at the end of chapter). The density tool measures a combination of seawater and formation density, resulting in low densities that should be interpreted with caution. The same type of behavior can be observed with the photoelectric effect log (PEF), which uses the same measurement principle. Borehole size variations also induce “cycle skipping” in the sonic velocity log, the result of the receivers picking incorrect first arrival times used in velocity calculation. This log, however, may be improved with post-cruise processing of the full-waveform sonic data. Comparison of the density, photoelectric effect, and velocity logs with the caliper log from Hole 960A (Fig. 60) illustrates the effects of borehole diameter variability on these log measurements. The resistivity and gamma-ray data are affected to a much lesser degree by borehole washout; the gamma-ray data will improve with post-cruise processing that smoothes the data and compensates for the borehole environment.

Selected Quad logs for Holes 960A and 960C are shown in Figures 60 and 61, respectively. The figures in this chapter are based on logs that have been depth-shifted to match the core by subtracting the water depth (2059.7 m) provided by direct pipe measurement. After coring, a discrepancy was discovered in the calculation of the water depth (see “Operations” section, this chapter). The corrected precision depth recorder reading established the true water depth as 2048.4, indicating a difference of 11.3 m. The processed logs at the end of this chapter have been depth-shifted to this depth. This means that features on the figures within this chapter will appear slightly deeper on the processed logs at the end of this chapter.

Although the Quad combination data from Hole 960A were linearly depth-shifted on board by an additional +1.5 m to match the core natural gamma-ray data for comparison purposes, there was little overlap between core and log data in Hole 960C, and no depth-shift for this hole was performed on board. Logs from both holes will undergo more precise depth-shifting during post-cruise processing. Preliminary shipboard processing of the FMS data at Hole 960C was

performed using Schlumberger’s Geoframe software. The images were enhanced by histogram equalization after undergoing depth-shifting (to seafloor) and voltage corrections, and were then used to determine dip and azimuth of sedimentary bedding. Because of a bug in the computation of true dips and azimuths, those data were computed independently using apparent dips and azimuths, diameter (average between calipers 1 and 2), deviation, and azimuth of the hole (Fig. 62). Complete reprocessing and reinterpretation of the FMS data will be performed post-cruise.

Comparison of Core and Log Physical Property Measurements

Low core recovery at Hole 960A, the lack of overlap between the cored and logged intervals in Hole 960C, and the poor quality of the density and sonic logs obtained prohibit valid correlation of log density and velocity data with core measurements. The natural gamma-ray data for the core and log at Hole 960A (Fig. 63) demonstrate good correspondence where recovery is sufficient to offer comparison, but for most of the interval logged such a comparison was not possible. The large spike in gamma radiation at approximately 180 mbsf is seen in both the core and in the log and measures 860 API units in the log.

Log Interpretation and Lithology

The natural gamma-ray, resistivity, and caliper logs (Hole 960A only) and the density and porosity logs (for Holes 960A and 960C) show trends that correlate well with most of the major lithologic unit boundaries derived from core descriptions (Figs. 60, 61). The boundary that separates lithologic Subunit IB (clayey nanofossil/foraminifer/micrite ooze to chalk; “Lithostratigraphy” section, this chapter), from lithologic Subunit IIA (interbedded and intermixed nanofossil chalk, micrite chalk with radiolarians, porcellanite, chert, glauconite and clay) is clearly visible on the natural gamma-ray log. High uranium peaks that occur throughout lithologic Unit II coincide with elevated organic carbon values measured in core samples in this unit (see Fig. 46, “Organic Geochemistry” section, this chapter), which suggest uranium fixation by organic matter under reducing conditions. The log from Hole 960A (Fig. 60) shows a significant increase in uranium and a smaller increase in potassium near this boundary (100 mbsf). Within lithologic Subunit IIA, continued high uranium values peak at depths of about 115 and 125 mbsf, where claystone was recovered in the cores (see “Principal Results” section, this chapter). Although the density log also shows an increase, this log must be interpreted with caution because of the detrimental effects of borehole washout at this depth as indicated by the caliper log.

The boundary that separates lithologic Subunit IIA from Subunit IIB (comprising black chert, porcellanite, and claystone; see “Lithostratigraphy” section, this chapter) coincides with the depth (about 136 mbsf) where the resistivity and density logs begin to decrease and the neutron porosity starts to climb. This trend continues throughout

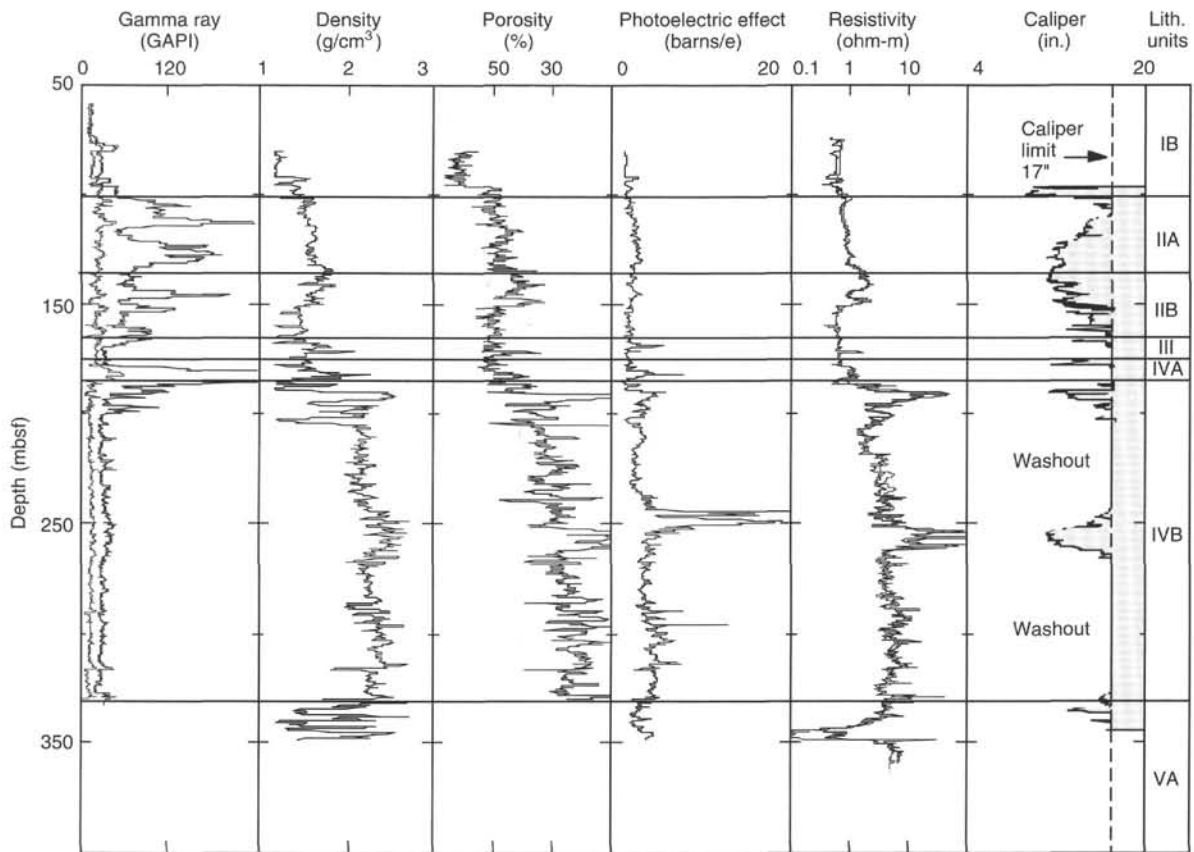


Figure 60. Summary of selected log data from Hole 960A. Lithologic units are shown at right (see "Lithostratigraphy" section, this chapter).

Subunit IIB with the exception of a short (2–3 m) interval at approximately 147 mbsf, suggesting the presence of a more resistant bed at this depth not recovered in the core (see processed logs at the end of chapter). A similar bed is indicated within this unit in Hole 959D at about 445 mbsf (see Fig. 65, "Site 959" chapter, this volume).

The most notable change associated with the transition to lithologic Unit III, a lower Eocene palygorskite claystone with barite nodules, is the abrupt deterioration in hole conditions as shown by the caliper log. In Hole 960A, the caliper arms lost contact with the borehole wall at this boundary, and density and porosity measurements made under these conditions are suspect. In Hole 960C, the FMS tool logged the transition between the base of lithologic Unit III, Subunit IVA (micrite claystone and chalk), and the top of Subunit IVB (quartz sand limestones; see "Lithostratigraphy" section, this chapter). This interval appears highly disturbed, as only a few beds can be seen on all four pads. This may be due to the combination of poor borehole conditions, discontinuities in the sedimentary layers, and fracturing.

Subunit IVA contains the dominant feature of the logs at this site: anomalously high natural gamma-ray values, which peak at about 182 mbsf in Hole 960A (206 mbsf in Hole 960C) and indicate uranium values reaching 107 ppm in Hole 960A (Fig. 64). XRD analysis on a sample from Section 159-960A-21R-1 shows several apatite peaks that may be responsible for the high uranium content (see Fig. 21, "Lithostratigraphy" section, this chapter).

The boundary between lithologic Subunit IVA and the limestone of Subunit IVB is characterized by a sharp elevation in density and resistivity, along with a decrease in porosity and natural gamma radiation. The resistivity log peaks at about 190 mbsf in Hole 960A (220 mbsf in Hole 960C) before dropping again but still remaining higher

than in Subunit IVA. Below this depth resistivity climbs steadily until about 250 mbsf in Hole 960A (280 mbsf in Hole 960C). At this depth, there is another sharp increase in the resistivity and density logs (with a corresponding decrease in porosity), lasting for approximately 15 m (280–295 mbsf, Hole 960C). This reflects the change to the more resistant, pure bioclastic limestone in the middle of lithologic Subunit IVB (see "Lithostratigraphy" section, this chapter). The change is also apparent in the caliper log: the center of this subunit was noticeably harder than the upper and lower parts and is one of the few sections within the logged interval where the borehole was not washed out and valid FMS data were obtained. In the interval from 275 to 292 mbsf (Hole 960C), FMS images show alternating beds 5 to 40 cm thick, with laminations in the resistive beds. The interval at 323–351 mbsf (Hole 960C) can be correlated with Cores 159-960C-25X and 26X, which exhibit alternating layers of pelagic and hemipelagic sedimentation with grain-flow deposition of limestones. Downhole (323–351 mbsf), the thickness of the beds decreases to 5–10 cm and there is some evidence of cross-bedding (Fig. 65).

Structural Measurements with FMS images

The FMS images indicate that hole deviation is limited in Hole 960C. The deviation is less than 1.5° above 285 mbsf, but increases up to 3° from 275 to 330 mbsf (Fig. 62). Such small values prevent a reliable measurement of hole azimuth, at least in the upper part of the logged interval. Downhole, the hole maintains an azimuth of 50°. Unfortunately, most of Hole 960C is too washed out for logging (Fig. 61). Only three intervals (198–215, 275–292, and 323–351 mbsf) are narrow enough to allow contact between at least two FMS pads and the borehole.

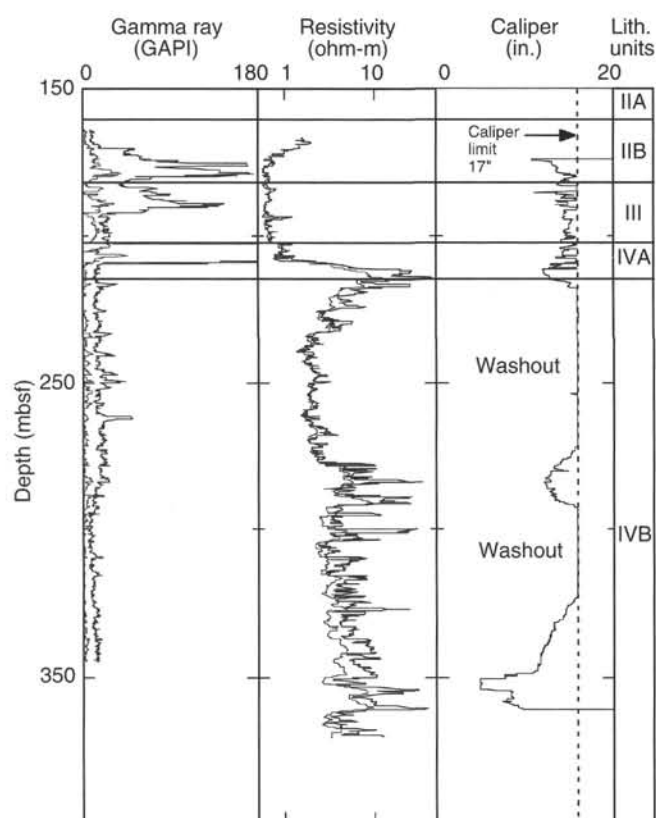


Figure 61. Summary of selected log data from Hole 960C. Lithologic units are shown at right (see "Lithostratigraphy" section, this chapter).

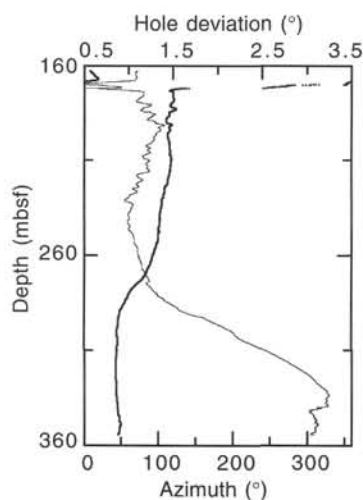


Figure 62. Deviation (thin line) and azimuth (thick line and dots) of Hole 960C in the interval logged by the FMS tool. Deviation and azimuth are by reference to the vertical and north, respectively.

As Hole 960C is only slightly deviated, the hole azimuth does not represent the elongation axis, which consequently is unknown. The ratio from the two calipers' measurements provides only an apparent elongation (Fig. 66). From 206 to 215 mbsf, this ratio is low, between 1 and 1.1, with an increase where one caliper is oriented N170°. From 275 to 292 mbsf, the caliper ratio varies between 1 and 1.15, with several sudden increases that can be related to breakout (N50° to N70°

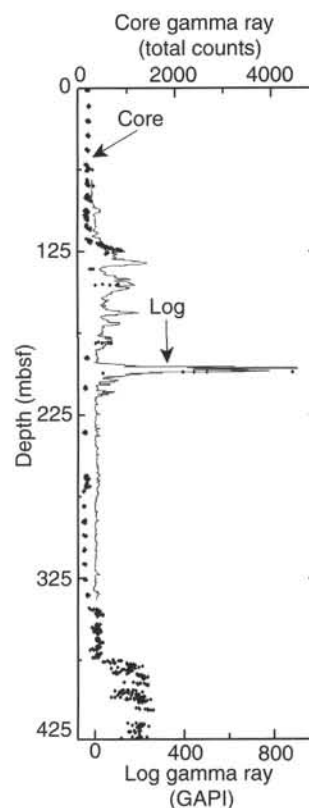


Figure 63. Comparison of core and log natural gamma radiation.

trending) recorded by caliper 2 and one decrease that is possibly related to a breakout recorded by caliper 1. In this section, the maximum caliper ratio is reached when one caliper is oriented N160°–N170°, with the minimum at N20°. Between 334 and 340 mbsf, the caliper ratio remains at almost 1, even though caliper 1 changes in azimuth from N140° to N05°, indicating an almost round hole. Finally, from 340 to 347 mbsf, the hole becomes narrower and exhibits a strong elongation (up to 1.65), probably related to collapse rather than breakout. All these observations are consistent with a northwest-southeast elongation of Hole 960C, similar to that seen at Site 959.

Dip and azimuth of sedimentary bedding were measured on the FMS images in the intervals where the hole is sufficiently narrow, with most of the measurements made between 325 and 352 mbsf (Fig. 67). The average dip is about 17°, and there is no evident increase of dip with depth. The average azimuth is between N15° and N25°. But, as in Hole 959D, both azimuths and dips exhibit important variations about their average values that cannot be ascribed to measurement resolution: from 2° to 42° for the dips, from N330° to N60° for the azimuths. The changes in dip and azimuth are correlated and rotation axes can be retrieved from sets of measurements made on successive bedding planes.

Each rotation axis is derived from a set of three to six consecutive measurements of bedding, with constant changes (increasing or decreasing) in azimuths and dips, as expected for a progressive rotation. The thickness of the sets ranges from 10 cm to 3 m. Both increasing and decreasing downhole dips were observed. Some increasing and decreasing dips are consecutive and are related to the same rotation axis, but more commonly, they show a change in rotation axis of as much as 90°. Moreover, the change in orientation of the rotation axis can be followed between several successive sets. The vertical scale for these types of changes in orientation seems to be 2 to 5 m.

Together, the bedding measurements from Hole 960C do not provide a clear image of a preferential trend for the rotation axis, as they

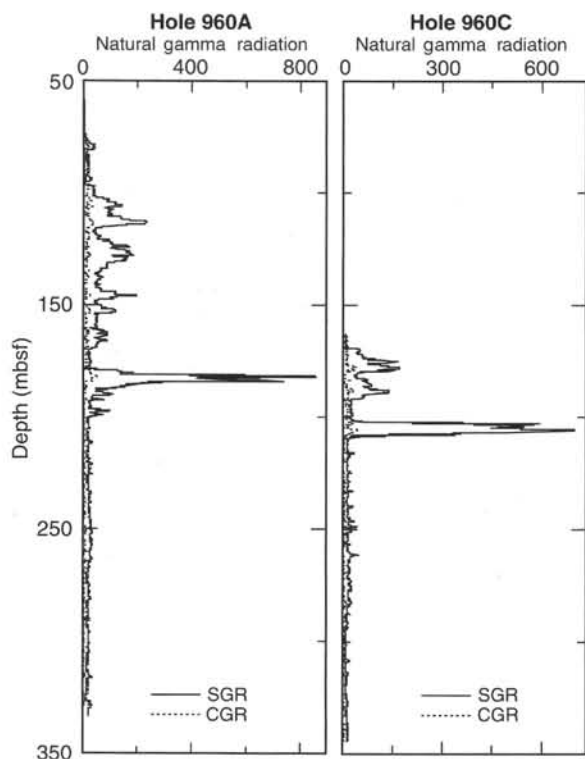


Figure 64. Natural gamma radiation from Holes 960A and 960C. SGR is the total signal, including potassium, thorium, and uranium. CGR includes only potassium and thorium, so the difference between the two is an indication of uranium content.

trend from N280° to N115°, with a slight dip northward (Fig. 68). Two preferential orientations appear from N300° to N330° and at N40°.

Two main mechanisms can be involved in the tilting of sedimentary beds at a centimeter to decimeter scale: tectonically induced rotation and wedge-shaped sedimentation. An example of tilting induced by a normal fault can be seen in Section 159-960C-26X-2, 117–124 cm (Fig. 69). The apparent rotation (measured on core section) in these siltstones is 4°, with an increase of dip downhole. On the FMS images, many faults can be inferred but cannot be correlated easily from pad to pad, and so were not studied on board.

Sedimentary structures can also explain sharp changes in dip down section. A few angular relationships related to erosional surfaces at the base of grain flows can be seen in cores, such as in Section 159-960C-26X-2, 70–82 cm, where the apparent angle reaches 2°. But the most significant angles are found in cross-laminated coarse sediments. In Section 159-960C-26X-1, 126–130 cm, the apparent dip of the bedding increases downhole by 16°, then decreases by 14°. Many cross-bedding structures can be observed on the FMS images, and they are involved in most of the rotation axes trending N270° (or N90°) to N330°, which indicates that the sediment transport direction was toward the north to northeast.

The succession of wedge-shaped bedding probably results from a combination of several processes. Sedimentary processes related to grain-flow deposition of grainstones and packstones can explain the abrupt changes of the dips. Divergence of grain flows in a submarine fan can also explain the dispersion of the trends of the rotation axis. However, these sedimentary processes can hardly be involved in tilting of in situ deposited pelagic or hemipelagic sediments. For this type of sediment, rotations are most likely related to faulting, either induced by regional tectonic stresses, or to gravitational sliding.

Borehole Temperature

The Lamont-Doherty Temperature Logging Tool (TLT) was run at the bottom of the seismic stratigraphic tool string in Holes 960A and 960C. The formation cools during drilling operations and hole conditioning because of fluid circulation, and temperatures begin to return to normal only after circulation has ceased. Both holes were conditioned immediately prior to logging. (Hole 960A: about 4 hrs before; Hole 960C: about 2.5 hrs before), so the temperatures measured predominantly reflect the seawater temperature in the borehole, rather than the true formation temperature.

In Hole 960A, the maximum temperature measured was 7°C at 370 mbsf. A consistent difference in temperatures measured between the first and second pass is probably because of clogging of the thermistors with mud collected on the first pass.

The temperatures in Hole 960C show a larger range than in the previous hole. The maximum temperature measured is 29°C at 374 mbsf. Thermal lags caused by mud clogging also can be observed between the downhole and uphole logs, with the latter more affected by this phenomenon. The temperature shows a sharp increase from 280 to 300 mbsf toward the bottom of the hole.

Synthetic Seismogram

A log-derived synthetic seismogram is not presented for this site because of poor density and velocity data quality associated with borehole washouts throughout the logged interval. Post-cruise processing of the velocity (full waveform) data is required to produce a reliable velocity log.

REFERENCES

- Bailey, S.W., 1988. Structures and compositions of other trioctahedral 1:1 phyllosilicates. In Bailey, S.W. (Ed.), *Hydrous Phyllosilicates (Exclusive of Micas)*. Rev. Mineral., 19:169–188.
- Baker, P.A., Gieskes, J.M., and Elderfield, H., 1982. Diagenesis of carbonates in deep-sea sediments: evidence from Sr²⁺/Ca²⁺ ratios and interstitial dissolved Sr²⁺ data. *J. Sediment. Petrol.*, 52:71–82.
- Berggren, W.A., 1977. Late Neogene planktonic foraminiferal biostratigraphy of the Rio Grande Rise (South Atlantic). *Mar. Micropaleontol.*, 2:265–313.
- Berggren, W.A., Kent, D.V., Swisher, C.C., III, and Aubry, M.-P., in press. A revised Cenozoic geochronology and chronostratigraphy. In Berggren, W.A., Kent, D.V., and Hardenbol, J. (Eds.), *Geochronology, Time Scales, and Global Stratigraphic Correlations: A Unified Temporal Framework for an Historical Geology*. Spec. Publ.—Soc. Econ. Paleontol. Mineral., 54.
- Bolli, H.M., Saunders, J.B., and Perch-Nielsen, K. (Eds.), 1985. *Plankton Stratigraphy*: Cambridge (Cambridge Univ. Press).
- Bonatti, E., and Joensuu, O., 1968. Palygorskite from the deep sea: a reply. *Am. Mineral.*, 54:568.
- Bouillin, J.P., Poupeau, G., Riou, L., Sabil, N., Basile, C., Mascle, J., Mascle, G., and the Equanaute Scientific Party, 1994. La marge transformante de Côte d'Ivoire-Ghana: premières données thermo-chronologiques (campagne Equanaute, 1992). *C. R. Acad. Sci. Ser. 2*, 318:1365–1370.
- Chamley, H., 1989. *Clay Sedimentology*: Berlin (Springer-Verlag).
- Coudé-Gaussen, G., and Blanc, P., 1985. Présence de grains éolisés de palygorskite dans les poussières actuelles et les sédiments d'origine désertique. *Bull. Soc. Geol. Fr.*, 14:571–579.
- Couture, R.A., 1977. Composition and origin of palygorskite-rich and montmorillonite-rich zeolite-containing sediments from the Pacific Ocean. *Chem. Geol.*, 19:113–130.
- Curry, W.B., Shackleton, N.J., Richter, C., et al., 1995. *Proc. ODP, Init. Repts.*, 154: College Station, TX (Ocean Drilling Program).
- Debrabant, P., Fagel, N., Chamley, H., Bout, V., and Caulet, J.P., 1993. Neogene to Quaternary clay mineral fluxes in the Central Indian Basin. *Palaeogeogr., Palaeoclimat., Paleoecol.*, 103:117–131.
- Deconinck, J.F., Beaudoin, B., Chamley, H., Joseph, P., and Raoult, J.F., 1985. Contrôles tectonique, eustatique et climatique de la sédimentation

- argileuse du domaine subalpin français au Malm-Crétacé. *Rev. Geogr. Phys. Geol. Dyn.*, 26:311–320.
- Donnelly, T.W., and Merrill, L., 1977. The scavenging of magnesium and other chemical species by biogenic opal in deep-sea sediments. *Chem. Geol.*, 19:167–186.
- Enos, P., and Moore, C., 1983. Fore-reef slope environment. In Scholle, P., Bebout, D., and Moore, C. (Eds.), *Carbonate Depositional Environments*. AAPG Mem., 33:507–618.
- Ewing, M., Worzel, J.L., et al., *Init. Repts. DSDP*, 1: Washington (U.S. Govt. Printing Office).
- Gartner, S., Jr., 1977. Calcareous nannofossil biostratigraphy and revised zonation of the Pleistocene. *Mar. Micropaleontol.*, 2:1–25.
- Gibbs, R.J., 1977. Clay mineral segregation in the marine environment. *J. Sediment. Petrol.*, 47:237–243.
- Gieskes, J.M., 1981. Deep-sea drilling interstitial water studies: implications for chemical alteration of the oceanic crust, layers I and II. In Warne, J.E., Douglas, R.G., and Winterer, E.L. (Eds.), *The Deep Sea Drilling Project: A Decade of Progress*. Spec. Publ.—Soc. Econ. Paleontol. Mineral., 32:149–167.
- Guiraud, M., Benkhelil, J., Mascle, J., Basile, C., Mascle, G., and the Equanaute teams, in press a. Syn-rift to syn-transform deformation: evidences from deep-sea dives along the Côte d'Ivoire-Ghana Transform Margin. *Geo-Mar. Lett.*
- Guiraud, M., Mascle, J., Benkhelil, J., Basile, C., Mascle, G., and Durand, M., in press b. Early Cretaceous sedimentary environment of the Côte d'Ivoire-Ghana Transform Margin as deduced from deep dives data. *Geo-Mar. Lett.*
- Jansa, L.F., Enos, P., Tucholke, B.E., Gradstein, F.M., and Sheridan, R.E., 1979. Mesozoic-Cenozoic sedimentary formations of the North American Basin, western North Atlantic. In Talwani, M., Hay, W., and Ryan, W.B.F. (Eds.), *Deep Drilling Results in the Atlantic Ocean: Continental Margins and Paleoenvironment*. Am. Geophys. Union, Maurice Ewing Ser., 3:1–57.
- Kastner, M., 1981. Authigenic silicates in deep sea sediments: formation and diagenesis. In Emiliani, C. (Ed.), *The Sea* (Vol. 7): *The Oceanic Lithosphere*: New York (Wiley), 915–980.
- Kastner, M., Keene, J.B., and Gieskes, J.M., 1977. Diagenesis of siliceous oozes. I. Chemical controls on the rate of opal-A to opal-CT transformation—an experimental study. *Geochim. Cosmochim. Acta*, 41:1041–1059.
- Lucas, J., and Prévôt, L., 1975. Les marges continentales, pièges géochimiques: l'exemple de la marge atlantique de l'Afrique à la limite Crétacé-Tertiaire. *Bull. Soc. Geol. Fr.*, 17:496–501.
- Mascle, J., Auroux, C., and the Shipboard Scientific Team, 1989. Les marges continentales transformantes ouest-africaines (Guinée, Côte d'Ivoire-Ghana) et la zone de fracture de la Romanche: Campagne Equamarge II (Février-Mars 1988). *Campagnes Océanographiques Françaises*, 8: Brest (IFREMER).
- Mascle, J., Basile, C., Pontoise, B., and Sage, F., 1995. The Côte d'Ivoire-Ghana transform margin: an example of an ocean-continent transform boundary. In Banda, E., Talwani, M., and Thorne, M. (Eds.), *Rifted Ocean-Continent Boundaries*, NATO ASI Ser.: Dordrecht (Kluwer), 327–339.
- Mascle, J., Blarez, E., and Marinho, M., 1988. The shallow structure of the Guinea and Côte d'Ivoire-Ghana transform margins: their bearing on the equatorial Atlantic Mesozoic evolution. *Tectonophysics*, 155:193–209.
- Mascle, J., Guiraud, M., Basile, C., Benkhelil, J., Bouillin, J.P., Cousin, M., and Mascle, G., 1993. La marge transformante de Côte d'Ivoire-Ghana: premiers résultats de la campagne Equanaute (Juin 1992). *C. R. Acad. Sci. Ser. 2*, 316:1255–1261.
- McRae, S.G., 1972. Glauconite. *Earth-Sci. Rev.*, 8:397–440.
- Meischner, K.D., 1964. Allodapische Kalke, turbidite in riff-nahen sedimentations-becken. In Bouma, A.H., and Brouwer, A. (Eds.), *Turbidities*: Amsterdam (Elsevier).
- Millot, G., 1964. *Géologie des Argiles*: Paris (Masson).
- , 1970. *Geology of Clays*: Berlin (Springer-Verlag).
- Odin, G.S., and Mather, A., 1981. Die glauconarum origine. *Sedimentology*, 28:611–641.
- Odum, I.E., 1984. Glauconite and celadonite minerals. In Bailey, S.W. (Ed.), *Micas*. Rev. Mineral., 13:545–572.
- Pickering, K.T., Hiscott, R., and Hein, F.J., 1989. *Deep-marine Environments: Clastic Sedimentation and Tectonics*: London (Unwin Hyman).
- Pisciotta, K.A., 1981. Distribution, thermal histories, isotopic compositions, and reflection characteristics of siliceous rocks recovered by the Deep Sea Drilling Project. In Warne, J.E., Douglas, R.G., and Winterer, E.L. (Eds.), *The Deep Sea Drilling Project: A Decade of Progress*. Spec. Publ.—Soc. Econ. Paleontol. Mineral., 32:129–148.
- Reineck, H.E., and Singh, I.B., 1980. *Depositional Sedimentary Environments* (2nd ed.): Berlin (Springer-Verlag).
- Sage, F., 1994. Structure crustale d'une marge transformante et du domaine océanique adjacent: exemple de la marge de Côte d'Ivoire-Ghana [Ph.D. thesis]. Univ. Pierre et Marie Curie, Paris.
- Shipboard Scientific Party, 1978. Site 380. In Ross, D.A., Neprochnov, Y.P., et al., *Init. Repts. DSDP*, 42 (Pt. 2): Washington (U.S. Govt. Printing Office), 119–291.
- Sibuet, J.-C., Hay, W.W., Prunier, A., Montadert, L., Hinz, K., and Fritsch, J., 1984. Early evolution of the South Atlantic Ocean: role of the rifting episode. In Hay, W.W., Sibuet, J.-C., et al., *Init. Repts. DSDP*, 75 (Pt. 1): Washington (U.S. Govt. Printing Office), 469–481.
- Singer, A., and Galan, E. (Eds.), 1984. *Palygorskite-Sepiolite: Occurrences, Genesis, and Uses*: Amsterdam (Elsevier), Dev. Sedimentol., 37.
- Thompson, G.R., and Hower, J., 1975. The mineralogy of glauconite. *Clays Clay Miner.*, 23:289–300.
- Tomadin, L., Lenaz, R., Landuzzi, V., Mazzucottelli, A., and Vannucci, R., 1984. On wind-blown dusts over the central Mediterranean. *Oceanol. Acta*, 7:13–24.
- Weaver, C.E., and Beck, K.C., 1977. Miocene of the S.E. United States: a model for chemical sedimentation in a perimarine environment. *Sediment. Geol.*, 17:1–234.

Ms 159IR-106

NOTE: For all sites drilled, core-description forms (“barrel sheets”) and core photographs can be found in Section 4, beginning on page 317. Smear-slide data can be found in Section 5, beginning on page 587. Scanned structural VCDs, structural data spreadsheets, and selected scanned microstructures are included on the CD-ROM in the back of this volume. Also presented on the CD-ROM are all processed logs (including FMS, dipmeter, BRG temperature, high-resolution density, and neutron data), sonic waveforms, and explanatory text.

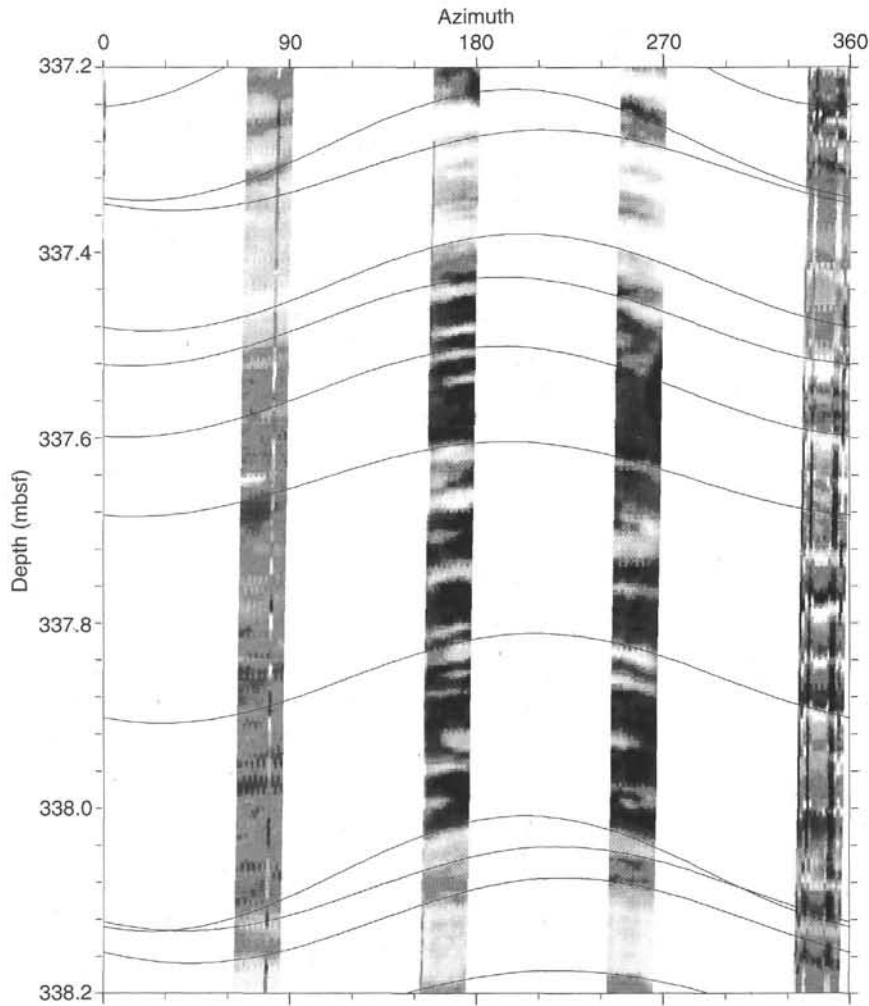


Figure 65. FMS image of Subunit IVB. The image is displayed without vertical exaggeration. Horizontal scale is azimuth by reference to north, vertical scale is in meters below seafloor. The sinusoids follow the trace of the intersection between bedding and borehole. The beds used in sets 3 to 5 are shown in Figure 69. Note cross-bedding at 337.3 and 338.1 mbsf.

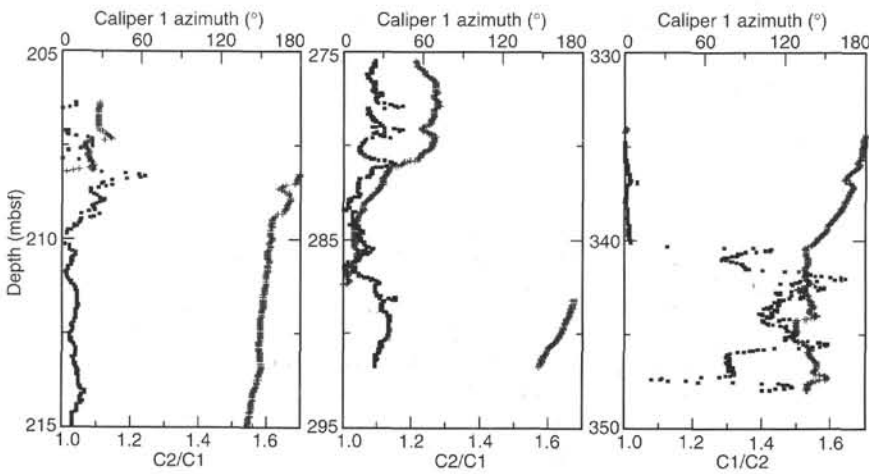


Figure 66. Caliper azimuth (plus signs), providing the wider measurement of Hole 960C, and wider caliper/narrower caliper ratio (solid squares). Caliper 1 is wider between 334 and 348 mbsf, and caliper 2 is wider between 206 and 215 mbsf and from 275 to 292 mbsf. The three sections shown are the only ones where the two calipers provide reliable measurements. The caliper ratio provides the elongation of the hole only when one caliper has the same azimuth as the elongation axis, which is unknown. A caliper ratio that equals 1 can be due to no elongation or to obliquity between caliper azimuth and elongation axis.

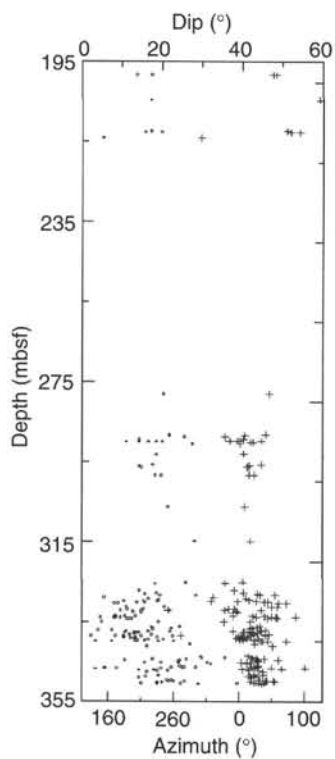


Figure 67. True dips (circles) and azimuths (plus signs) of bedding logged by the FMS in Hole 960C.

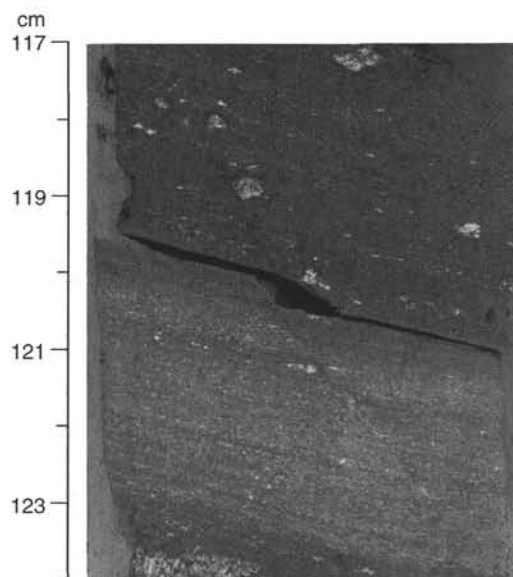


Figure 69. Normal fault and associated tilting in siltstones in Subunit IVB. (Section 159-960C-26X-2, 117–124 cm).

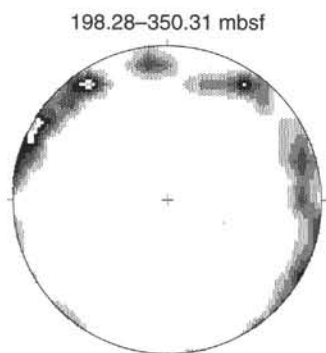


Figure 68. Stereographic plot (Schmidt net) of rotation axes. The net displays isodensity lines (2%, 4%, 6%, 8%, and 10%) for a total of 38 rotation axes between 198.28 and 350.31 mbsf. The white areas trending N300°–N310°, N330°, and N40° are the maxima (more than 8%).

SHORE-BASED LOG PROCESSING

HOLE 960A

Bottom felt: 2048.4 mbrf (used for depth shift to seafloor). Note: the mud line was originally established by the drillers at 2059.7 mbrf by direct pipe measurement. The corrected PDR reading was 2048.4 mbrf (see "Operations" section, this chapter).

Total penetration: 451.2 mbsf (calculated using a "bottom felt" depth of 2059.7 m)

Total core recovered: 145.01 m (32.1%)

Logging Runs

Logging string 1: DIT/SDT/HLDT/CNTG/NGT

The wireline heave compensator was used to counter ship heave resulting from the mild sea conditions.

Bottom-hole Assembly

The following bottom-hole assembly depths are as they appear on the logs after depth shift to the seafloor. As such, there might be a discrepancy with the original depths given by the drillers on board. Possible reasons for depth discrepancies are ship heave, use of wireline heave compensator, and drill-string and/or wireline stretch.

DIT/SDT/HLDT/CNTG/NGT: Bottom-hole assembly at ~85 mbsf.

Processing

Depth shift: All original logs have been depth-shifted to the seafloor (-2048.4 m). Any correlation with core must take into account the difference of 11.3 m between core and log sub-bottom depth.

Gamma-ray processing: NGT data have been processed to correct for borehole size and the type of drilling fluid.

Acoustic data processing: The quality of the data is impaired by the bad hole conditions. The borehole size variations induced frequent cycle skipping in the log, the result of the receivers picking incorrect first arrival times. Because of the extremely noisy character of the sonic logs, no processing has been performed at this stage.

Quality Control

Data recorded through bottom-hole assembly (NGT and CNTG above 85 mbsf) should be used qualitatively only because of the attenuation on the incoming signal.

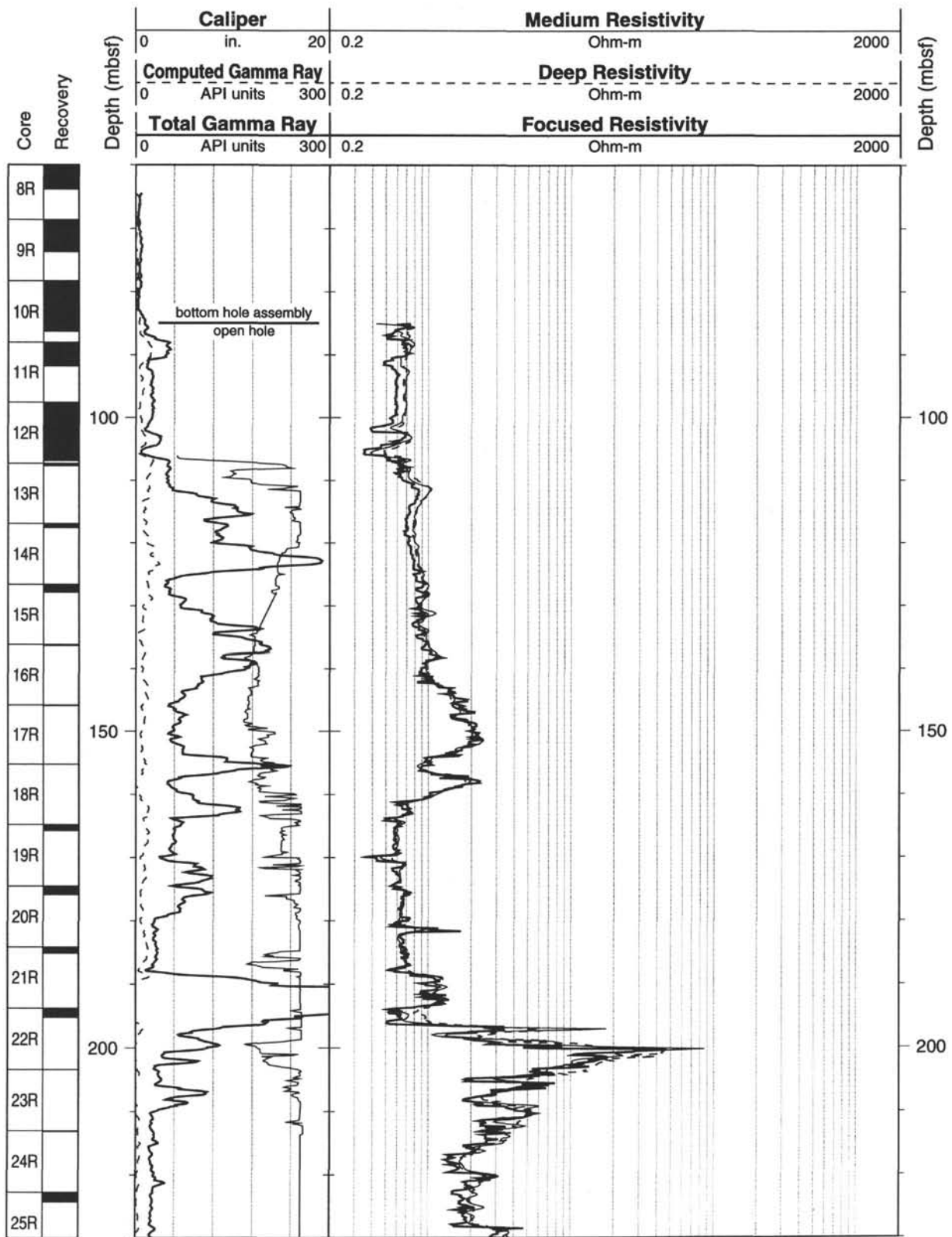
Hole diameter was recorded by the hydraulic caliper on the HLDT tool (CALI).

Details of standard shore-based processing procedures are found in the "Explanatory Notes" chapter, this volume. For further information about the logs, please contact:

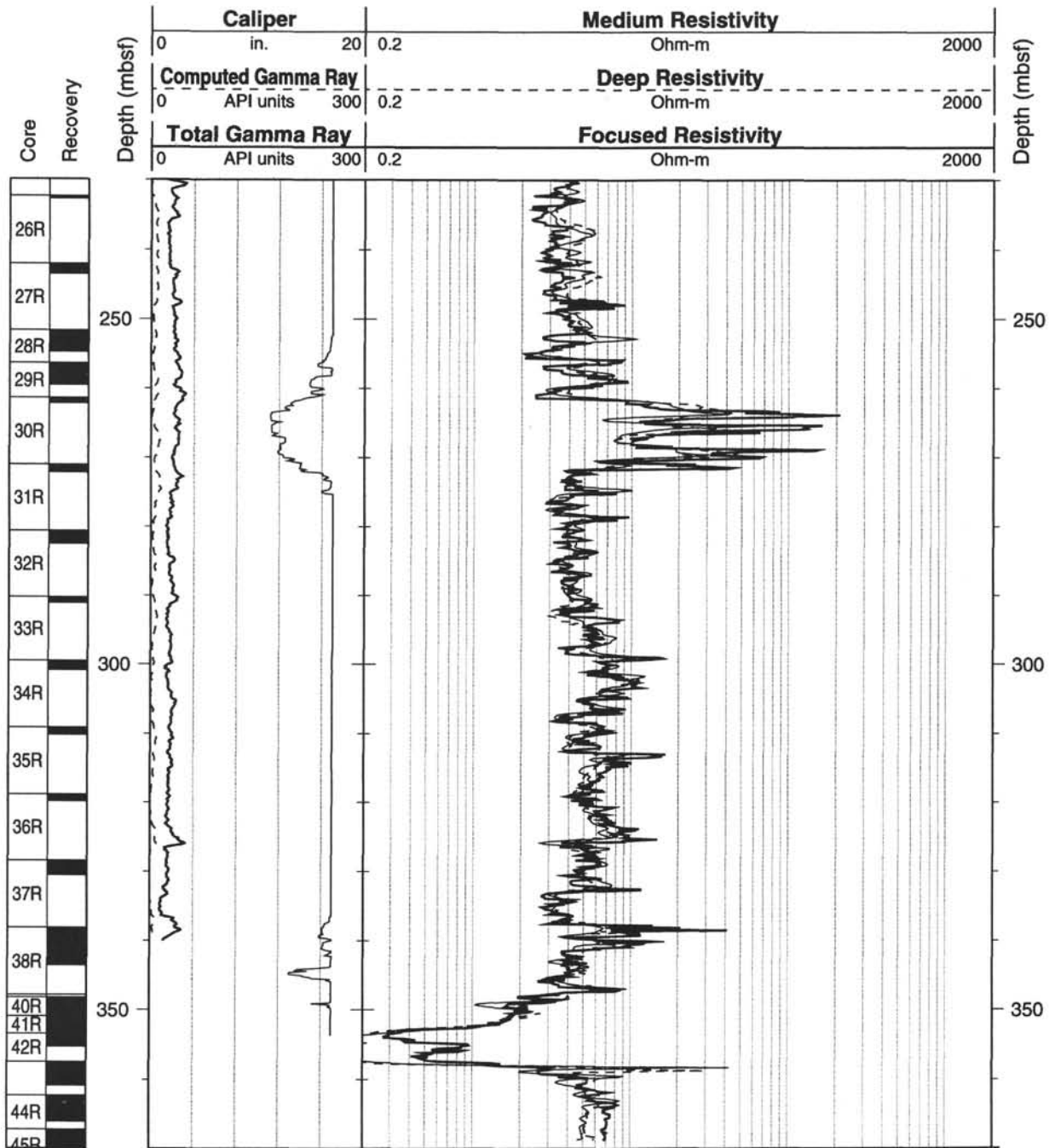
Cristina Broglia
Phone: 914-365-8343
Fax: 914-365-3182
E-mail: chris@ldeo.columbia.edu

Elizabeth Pratson
Phone: 914-365-8313
Fax: 914-365-3182
E-mail: beth@ldeo.columbia.edu

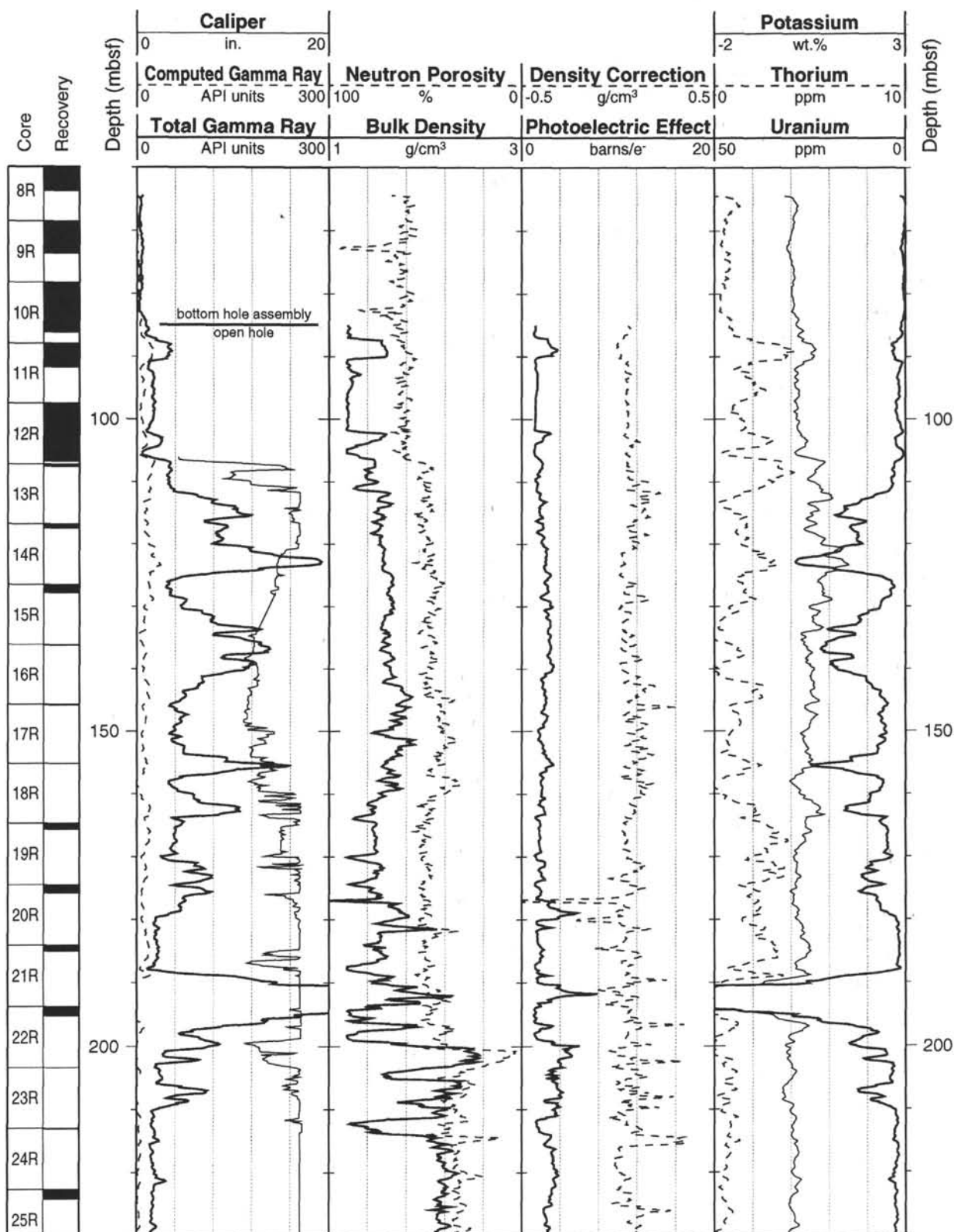
Hole 960A: Natural Gamma Ray-Resistivity-Sonic Logging Data



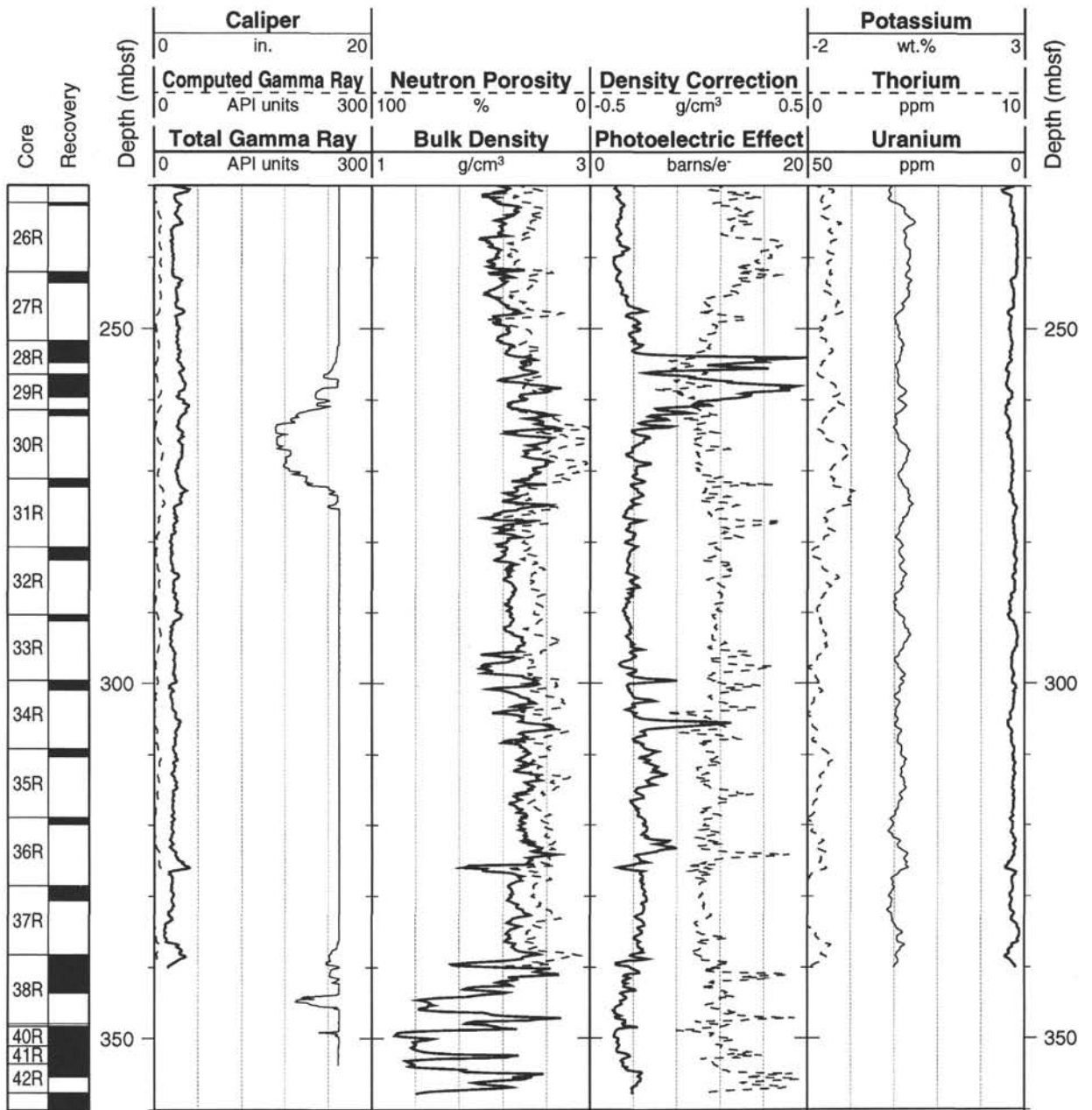
Hole 960A: Natural Gamma Ray-Resistivity-Sonic Logging Data (cont.)



Hole 960A: Natural Gamma Ray-Density-Porosity Logging Data



Hole 960A: Natural Gamma Ray-Density-Porosity Logging Data (cont.)



SHORE-BASED LOG PROCESSING

HOLE 960C

Bottom felt: 2046.3 mbrf (used for depth shift to seafloor)

Total penetration: 352.8 mbsf

Total core recovered: 160.67 m (69.8%)

Logging Runs

Logging string 1: DIT/SDT/NGT with hydraulic caliper and no HLDT source.

Logging string 2: FMS/GPIT/NGT

Wireline heave compensator was used during the FMS/GPIT/NGT run to counter ship heave resulting from the mild sea conditions. Due to electronics failure, no WHC could be used during the DIT/SDT/NGT run.

Bottom-hole Assembly

The following drill pipe depths are as they appear on the logs after differential depth shift (see "Depth shift" section) and depth shift to the seafloor. As such, there might be a discrepancy with the original depths given by the drillers on board. Possible reasons for depth discrepancies are ship heave, use of wireline heave compensator, and drill-string and/or wireline stretch.

DIT/SDT/NGT: Bottom-hole assembly at ~170 mbsf.

FMS/GPIT/NGT: Bottom-hole assembly at ~169 mbsf.

Processing

Depth shift: Reference run for depth shift: DIT/SDT/NGT. All original logs have been interactively depth shifted with reference to NGT from DIT/SDT/NGT run, and to the seafloor (-2046.3 m).

Gamma-ray processing: NGT data have been processed to correct for borehole size and type of drilling fluid.

Acoustic data processing: The quality of the data is impaired by the bad hole conditions. The borehole size variations induced frequent cycle skipping in the log, the result of the receivers picking incorrect first arrival times. Because of the extremely noisy character of the sonic logs, no processing has been performed at this stage.

Quality Control

Data recorded through bottom-hole assembly, such as the NGT data above 170 mbsf, should be used qualitatively only because of the attenuation on the incoming signal.

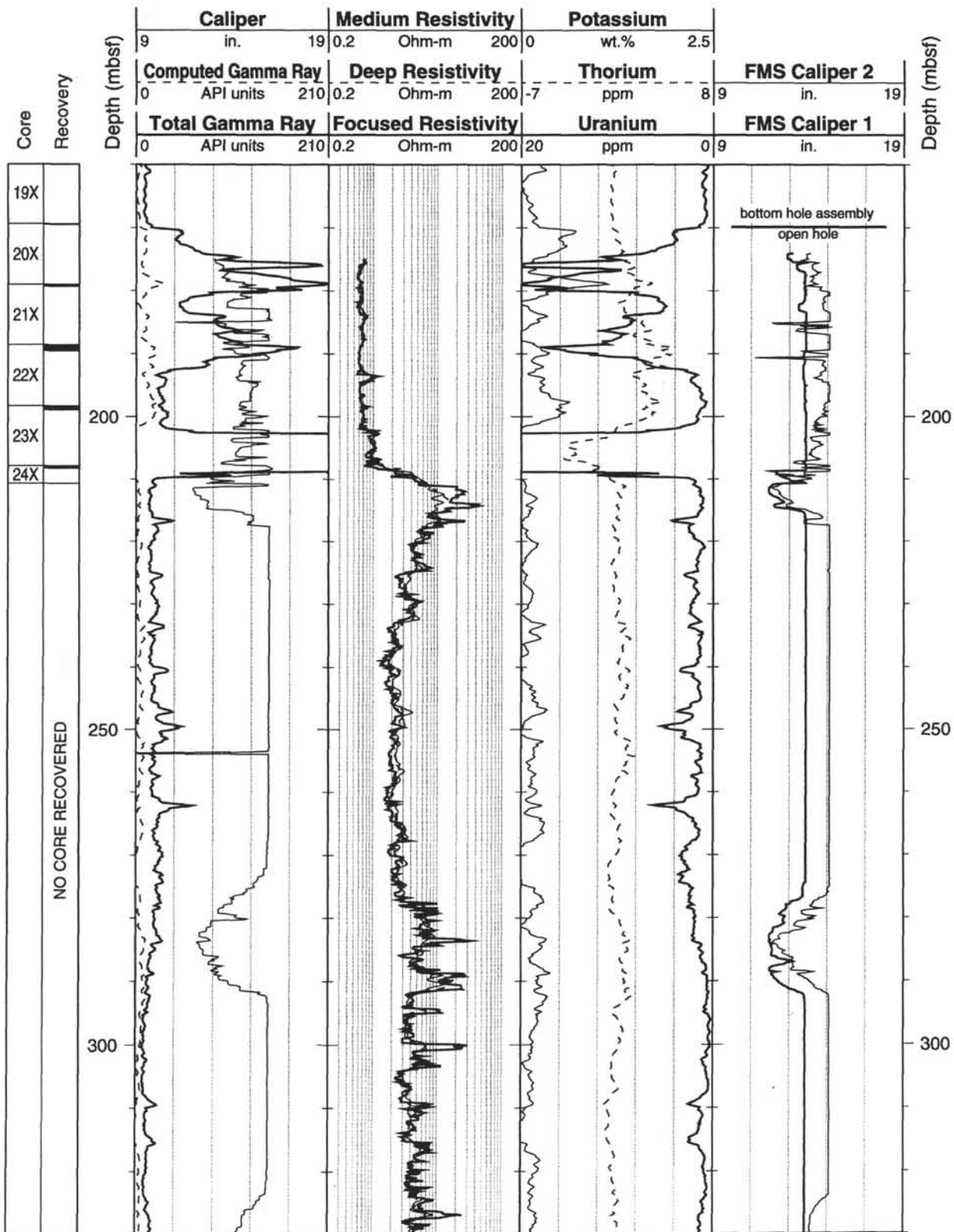
Hole diameter was recorded by the hydraulic caliper on the HLDT tool (CALI) and the caliper on the FMS string (C1 and C2).

Details of standard shore-based processing procedures are found in the "Explanatory Notes" chapter, this volume. For further information about the logs, please contact:

Cristina Broglia
Phone: 914-365-8343
Fax: 914-365-3182
E-mail: chris@ldeo.columbia.edu

Elizabeth Pratson
Phone: 914-365-8313
Fax: 914-365-3182
E-mail: beth@ldeo.columbia.edu

Hole 960C: Natural Gamma Ray-Resistivity Logging Data



Hole 960C: Natural Gamma Ray-Resistivity Logging Data (cont.)

